



Title	Distribution of Mountain Permafrost in the Daisetsu Mountains, Hokkaido, northern Japan
Author(s)	Ishikawa, Mamoru
Citation	北海道大学. 博士(地球環境科学) 甲第5716号
Issue Date	2001-12-25
DOI	10.14943/doctoral.k5716
Doc URL	<a href="http://hdl.handle.net/2115/32522">http://hdl.handle.net/2115/32522</a>
Type	theses (doctoral)
File Information	5716.pdf



[Instructions for use](#)

# **Distribution of Mountain Permafrost in the Daisetsu Mountains, Hokkaido, northern Japan**

by

**Mamoru ISHIKAWA**

## **ABSTRACT**

This study deals with the mapping and modelling the distribution of mountain permafrost in the Daisetsu Mountains, central Hokkaido, northern Japan. To these ends, the distribution and structure of permafrost were surveyed at a number of sites, covering a wide area. Simplified ground thermal prospecting methods including measurements of bottom temperature of snow cover (BTS), ground surface temperature monitoring through a year and shallow ground temperature (SGT) measurements were used together with DC resistivity sounding and imaging. With respect to the temporal BTS variations, three kinds of BTS evolution were recognized. Sites with a low BTS value were seen to correspond to areas where winter frost affects the ground thermal regimes, including direct cold heat penetration and subsurface lateral thermal flow during winter. The presence of permafrost was confirmed by DC resistivity soundings in the areas where low BTS values ( $< -2.0\text{ }^{\circ}\text{C}$ ) were recorded.

Extrapolating the thickness of permafrost layers estimated by previous studies and DC resistivity sounding at different altitudes, the lower limit of permafrost is considered to be at 1650 m ASL, where MAAT is estimated to be  $-2.0\text{ }^{\circ}\text{C}$ . This altitude is slightly higher than that estimated by Sone (1990), made on the basis of the analogy with circumpolar permafrost such as the lapse rate of air temperature and palsa. Around the lower altitudinal limit, patches of permafrost were identified where thick peat prevents thermal penetration during the summer where the potential radiation is significantly reduced due to topographic shading and where the cold air concentrates due to ventilation within open-work blocky materials.

SGT, year-round ground temperature monitoring and DC resistivity imaging were

used to assess the distribution and structures of permafrost in the summit areas were investigated in detail. Permafrost was identified beneath the wind-blown bare ground in the summit areas and under the wind-blown blocky slopes, where some snow is trapped during winter due to surface undulation. Permafrost beneath the ground surface lacking snow is thicker than those beneath wind-blown blocky slopes. On the southern slope, thicker active layers were found. This survey suggests that the occurrence of permafrost is strongly controlled by snow cover distribution and that permafrost structure is controlled by spatial differences in the amount of potential solar radiation.

Based on the field observations described above, the distribution of permafrost in the summit area is modelled. Geographical information systems (GIS) and a precise digital elevation model (DEM,  $2 \times 2$  m unit grid cell) were applied and represents the first attempt at modelling the distribution of mountain permafrost in Japan. The conventional model for calculating the distribution of potential solar radiation was improved by considering the effects of topographic shading effect. The improved model predicts the presence of permafrost beneath steep north facing blocky slopes with a coarse resolution. In addition, the model was developed to simulate the spatial distribution of snow cover taking into account the predominant strong wind direction and the effect of micro-topography with regards snow trapping. The simulated snow distribution was validated by comparison with oblique air photographs and the distribution of vegetation which gives a good indication of the distribution of snow cover. Based on the simulated snow cover distribution, cumulative freezing and thawing indexes (CFTI) on the ground surface were calculated spatially, using the results of year-round air temperature monitoring at an adjacent site. Negative CFTIs indicate the occurrence of permafrost and agree with the distribution of permafrost delineated by a number of field observations.

Discussion is made on the climatic significance of the spatial distribution of permafrost in summit areas of the Daisetsu Mountains. The development of permafrost in the Daisetsu Mountains is favored due to the absence of glaciers, the flat topography resulting from volcanic lava flow and the lack of snow cover blown off by wind. These situations are significantly different from those in the European Alps and Himalaya, where permafrost develops beneath the snow-covered slopes. Since the occurrence of permafrost in the summit areas of the Daisetsu Mountains is directly controlled by air temperature and thermal insulation by snow cover, the distribution of permafrost would be expected to change more rapidly than that of the European Alps and Himalaya. Changes in the spatial distribution of permafrost have been simulated in accordance

with a temperature rise predicted by GCM. The areas with permafrost in summit areas of the Daisetsu Mountains will be significantly reduced after the 2050s when the mean annual air temperature increases by 1.69 °C. In particular, permafrost will disappear in the fringes of the wind-blown flat ground and in the steep slopes.

## ACKNOWLEDGEMENTS

First of all, I would like to express my great thanks to Professor Kazuomi Hirakawa, Graduate School of Environmental Earth Science, Hokkaido University, who has been my supervisor since the beginning of my study. He provided me many helpful suggestions, advices and encouragements during the course of this work.

I also wish to express my grateful thanks to Professor Yugo Ono of Graduate School of Environmental Earth Science, Hokkaido University, who made many valuable suggestions and constructive advices for this thesis.

Thanks are due to Professor Masami Fukuda, Low Temperature Institute of Hokkaido University, and Dr. Teiji Watanabe, Graduate School of Environmental Earth Science, who made many valuable suggestions.

I would like to thank Dr. Norikazu Matsuoka, Institute of Geoscience, University of Tsukuba, who provided me chances to discuss with permafrost scientists in European countries and made many valuable suggestions for this thesis.

Gratitude also goes to Dr. Takanobu Sawagaki, Graduate School of Environmental Earth Science, Hokkaido University for providing numerous ideas and useful discussions.

I wish to acknowledge valuable instruction with Dr. Yoshimasa Kurashige, the University of Shiga Prefecture during my initial stages of this study.

Sincere thanks are extended to the member of Mountain Permafrost Research Group, Atsushi Ikeda, Yuki Sawada, Kotaro Fukui and Masafumi Aoyama, for their kind collaboration and discussion both in the field and laboratory.

I am also indebted to Shogo Iwasaki, Hotaka Matsumoto, Mikio Sukeno, Yoshinori Katayama, Akemi Yoda, Naohiro Nakamura, Yoko Otaki, and Shunsuke Tanaka for valuable assistance in the fieldwork. Help in drawing of detailed map by Dr. Liu Dali is also appreciated. We thank Mrs. M. Osada and Y. Hashimoto, OYO Corporation for providing helpful comments on analysis of DC resistivity soundings.

My special thanks are due to Dr. D. Vonder Mühll, University of Basel for practical instruction on applying geophysical method.

I express my gratitude to Dr. Richard Jones, Department of Geography, University of Liverpool and to Ms. Melissa Haltach, Ohio State University for their sincere advices for improving this paper, especially in English.

This research was supported by a grant-in-aid for scientific research from the Japan Society for the Promotion of Science.

Finally, I wish to express my gratitude thanks to my family, Noriko and Takehiro. They allowed me to concentrate on completing this dissertation and supported mentally during the course of this work. Without their help and encouragement, this study would not have been completed.

## CONTENTS

<b>ABSTRACT</b>	i
<b>ACKNOWLEDGEMENTS</b>	iv
<b>CONTENTS</b>	vi
<b>Chapter 1      Introduction</b>	<b>1</b>
1-1.      Characteristics of mountain permafrost distribution	1
1-2.      Significance of mountain permafrost	3
1-3.      Review of mountain permafrost studies	3
1-4.      Aims of this study and structure of this thesis	6
<b>Chapter 2      Physical Settings of the Daisetsu Mountains</b>	<b>7</b>
2-1.      Topography and Geology	7
2-2.      Climatic setting of the Daisetsu Mountains	10
2-3.      Vegetation	13
<b>Chapter 3      Field Survey Methods</b>	<b>15</b>
3-1.      Combined use of indirect prospecting	15
3-2.      Ground thermal prospecting	17
3-3.      BTS methods	17
3-4.      DC resistivity prospecting	19
3-4-1.      Physical background	
3-4-2.      DC resistivity sounding	
3-4-3.      DC resistivity imaging	
<b>Chapter 4      Permafrost Distribution beneath Snow Cover</b>	<b>25</b>
4-1.      Introduction	25
4-2.      Study areas	25
4-3.      Results and interpretations	28
4-3-1.      Spatial BTS variations	

4-3-2.	Temporal BTS variations	
4-3-3.	DC resistivity sounding and Permafrost Occurrence	
4-3-3-1.	Mt. Chubetsudake and its surroundings	
4-3-3-2.	Mt. Hakuundake and its surroundings	
4-4.	Three temporal BTS variations and thermal processes beneath snow cover	37
4-5.	BTS criteria and permafrost occurrences in the Daisetsu Mountains	39
4-6.	Altitudinal variations of permafrost in the Daisetsu Mountains	42
<b>Chapter 5</b>	<b>Spatial Variations of Permafrost Distribution</b>	<b>45</b>
5-1.	Introduction	45
5-2.	Local factors controlling the presence and structure of permafrost	45
5-2-1.	Snow cover and plant distribution	
5-2-2.	Potential solar radiations	
5-2-3.	Surface and subsurface materials	
5-3.	Results and Interpretations	51
5-4.	Micro-scale permafrost distribution and the factors controlling permafrost presence	76
<b>Chapter 6</b>	<b>Spatial Mountain Permafrost Modelling</b>	<b>78</b>
6-1.	Introduction	78
6-2.	Analytical procedure and data collection	79
6-3.	Modelling the distribution of potential radiation (PR)	79
6-3-1.	Computational procedures	
6-3-2.	The algorithm	
6-4.	Modelling the distribution of CFTI	82
6-4-1.	Modelling the distribution of snow cover	
6-4-1-1.	Model	
6-4-1-2.	Model validation	
6-4-2.	Modelling CFTI	
6-4-2-1.	Background	
6-4-2-2.	Assumption of thermal effect by snow cover and snow cover evolution	

	6-4-2-3. Model	
	6-4-2-4. Result and validation	
6-5.	Correlation between the proxies estimated and field evidences of permafrost occurrences	102
	6-5-1. Correlation between PR and Permafrost occurrence	
	6-5-2. Correlation between CFTI and Permafrost occurrence	
6-6.	Spatial changes of mountain permafrost in the Daisetsu Mountains	108
	6-6-1. Significance of permafrost in the summit areas of the Daisetsu Mountains	
	6-6-2. Global Circulation Model	
	6-6-3. Predicted changes of permafrost distribution	
<b>Chapter 7</b>	<b>Conclusions</b>	112
<b>References</b>		114

## Chapter 1 Introduction

### 1-1. Characteristics of mountain permafrost distribution

Permafrost is a thermal condition of the ground where ground temperatures remain at or below 0 °C for at least two years (Washburn, 1979). More than 20 per cent of the world's land area is underlain by permafrost (fig. 1.1), occurring in two contrasting geographical regions, namely high latitudes and high altitudes (Harris, 1988). The majority occurs in high latitudes of the northern hemisphere, while minority in high altitudes of mid- and low latitudes.

High altitude permafrost is commonly referred to as circumpolar permafrost and its distribution is classified into one of the three following zones: (a) continuous (>80% of areas underlain by permafrost), (b) discontinuous (30 to 80% of area underlain by permafrost) and (c) sporadic (<30% of area underlain by permafrost). These distributions are broadly governed by climate (AGGR, 1988). For example in Canada, the southern limits of the discontinuous zone are seen to roughly coincide with  $-1^{\circ}\text{C}$  mean annual air temperature (MAAT) (Brown, 1967).

Mountain permafrost is defined as permafrost that is found at high altitudes in middle and low latitudes where permafrost does not occur surrounding lowlands (Fujii, 1980), and differs considerably from lowland circumpolar permafrost. Clearly, the most important control on mountain permafrost is climate, which depends on the geographical location of the mountain (latitude, altitude, and distance from ocean). The zonation of mountain permafrost is not like that of circumpolar permafrost. Typically the lapse rate of decreasing temperature is used for zonation of mountain permafrost. However, some difficulties arise in determining the lower altitudinal limit of mountain permafrost.

The distribution of mountain permafrost is controlled by a number of factors such as slope inclination and aspect, micro-topography, and active layers consisting of coarse blocks with wide-open pore spaces (*e.g.* Harris, 1979; 1983). These factors influence the flux of energy across the surface of mountain permafrost areas in a way not commonly encountered in circumpolar lowlands. Therefore, the distribution of mountain permafrost is more complicated than that of circumpolar permafrost and restricted only where energy flux at the ground surface is thermally favorable.

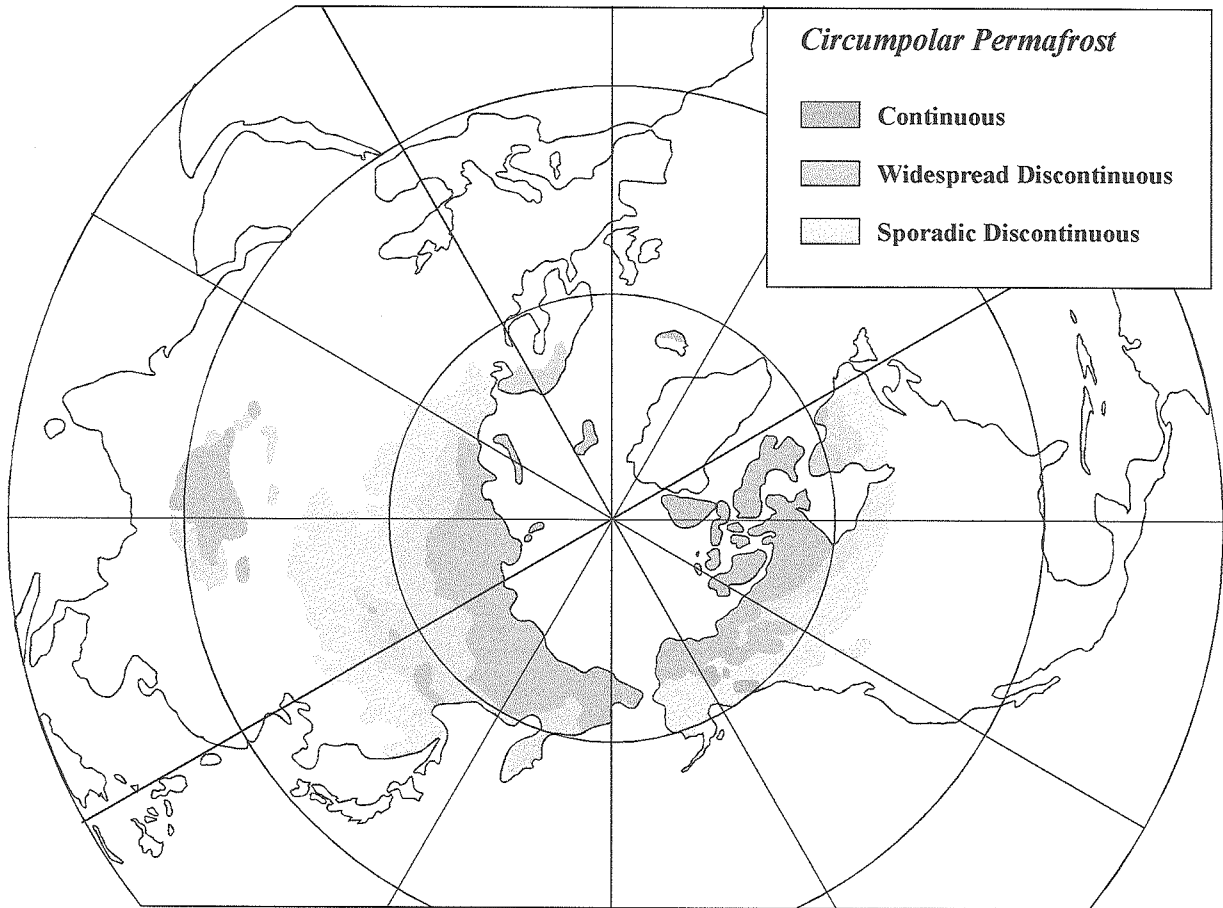


**Fig. 1.1** Distribution of circumpolar permafrost in the northern hemisphere (After Pewe, 1991)

## **1-2. Significance of mountain permafrost**

Owing to the changes in global climate and local ground surface energy flux, the warming and degradation of permafrost has been reported in the circumpolar region (*e.g.* Lachenbruch and Marshall, 1986; Osterkamp and Romanovsky, 1996; 1999). It is stressed that the degradation of permafrost in such region is discontinuous and sporadic regions (*e.g.* Osterkamp and Romanovsky, 1999).

This trend may also occur in mountain permafrost. Since the distribution of mountain permafrost is restricted to the areas where the temperature is slightly below 0°C, a slight shift in energy flux at the ground surface could lead to degradation and thawing of mountain permafrost over wide areas. Indeed the warming and thawing of permafrost has been reported in the mid-latitude mountains (fig. 1.2). Ground temperature monitoring in deep borehole demonstrates that the temperature of mountain permafrost has increased in the European mountains in recent years (Vonder Mühll, *et al.*, 1998; Harris *et al.*, 2001; Isaksen *et al.*, 2001). Accordingly, the areas underlain permafrost will change sensitively in mountain areas.

It is clear that more attention should be paid to the dynamics of mountain permafrost in order to assess the impact of high mountains in mid- and low latitudes owing to global warming. However, little attention has been given to these points, because the distribution of mountain permafrost is complicated and has not been clarified.

## **1-3. Review of mountain permafrost studies**

In the Japanese high mountains, permafrost can be found in Mt Fuji (Higuchi and Fujii, 1971; Fujii and Higuchi, 1972) and the Daisetsu Mountains (Fukuda and Kinoshita, 1974). In the Daisetsu Mountains the distribution of mountain permafrost has been discussed in relation to the lapse rate of air temperature (which is seen to decrease with elevation) and through the use of geomorphic features such as palsa (Takahashi and Sone, 1988; Sone 1990). Using air temperature, the distribution is predicted to be continuous in the areas with an elevation above 2050 m and discontinuous in the area between 1350 and 2050 m, if snow cover is less than 50 cm. However, such predictions have not been confirmed by detail field surveys.

Over the last two decades, rapid progress has been made in the study of mountain

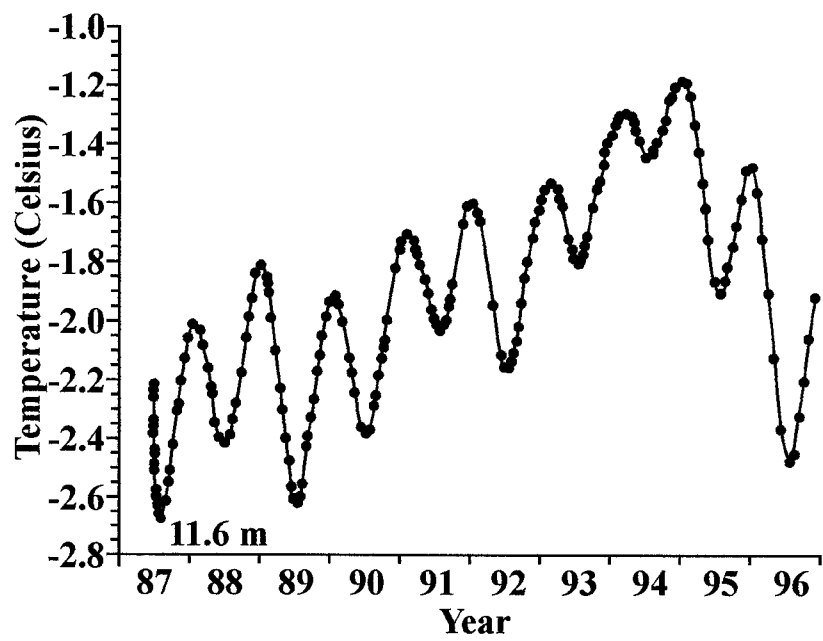


**Fig. 1.2** Temperature variations of mountain permafrost in the Murtel Rock Glacier, Engadin, Swiss Alps, 1987-1996(After Vonder Muehll et al., 1998).

permafrost in Europe. Significant progress for example has been made into gaining an understanding of the down-slope movements of ice-rich permafrost, leading to the development of rock glaciers (*e.g.* Haeberli, 1985). The active and fossil rock glaciers can indicate current and past mountain permafrost, respectively (Barsch, 1996). Important methodological developments have also been made in order to clarify more effectively the existences of permafrost efficiently in mountainous areas. Haeberli (1973) for example introduced a quick and reliable survey method utilizing BTS (bottom temperature of snow cover). In Europe the quantity of BTS data that has subsequently been produced, has led to attempts to model the spatial distribution of permafrost (Hoelzle, 1992; Hoelzle *et al.*, 1993; Keller, 1994; Hoelzle, 1994). In addition, some indirect geophysical methods such as DC resistivity sounding, shallow seismic sounding have been applied to identify and characterize the mountain permafrost (*e.g.* King, *et al.*, 1992; Vonder Mühll, *et al.*, 2001). Indeed geophysical and BTS analysis now represent the standard techniques used for mapping the distribution of permafrost (Haeberli, 1973; King, *et al.*, 1992, Vonder Mühll, *et al.*, 2001).

Another important area of progress concerns the modelling of the complicated distribution of mountain permafrost by means of geographical information systems (Keller 1992; Hoelzle, 1996; Hoelzle and Haeberli, 1995; Hoelzle, *et al.*, 2001; Etzelmüller, *et al.*, 2001). Empirical- and process-based models have been developed seeking to predict the distribution of mountain permafrost and can be used to examine the spatial and temporal changes in mountain permafrost that might occur in relation to future global climatic changes (Etzelmüller *et al.*, 2001; Hoelzle, *et al.*, 2001). Model validations are mainly based on BTS values, geophysical data and the surface geomorphic feature such as rock glaciers (Barsch 1988; 1992; Imhof, 1996).

The same approaches to that used for the European mountains have been applied to other areas in order to clarify distribution of permafrost in other mountains. In the Himalayan regions, the zonation of mountain permafrost has been attempted based on the distribution of rock glaciers (Jacob, 1992; Barsch and Jacob, 1998; Ishikawa *et al.*, 2001). Whilst in the Japanese Alps, efforts have to date concentrated on the distribution of rock glaciers within deglaciated cirques (Matsuoka, 1998; Matsuoka and Ikeda, 1998; Fukui and Iwata, 2000).

#### **1-4. Aims of this study and structure of this thesis**

Utilizing the technique developed for the study in the European Mountains, this study aims to map and model the distribution of mountain permafrost in the Daisetsu Mountains. A number of indirect methods have been used and a secondary purpose of the study is to examine the adaptability of these survey methods.

Following this introduction (chapter 1), the physical setting of the Daisetsu Mountains will be outlined (chapter 2). Chapter 3 will focus on the methodologies used during fieldwork to identify the permafrost. The first use of the BTS method for mapping mountain permafrost in the Japanese high mountains is also discussed. The use of DC resistivity methods including vertical sounding and two dimensional imaging is also described. Chapters 4 and 5 are devoted to the field investigations related to the distribution of permafrost on the basis of survey methods presented in chapter 3. In chapter 4, the distribution of permafrost including beneath snow cover is described regionally. BTS criteria for permafrost mapping are also discussed in this chapter. Chapter 5 describes the spatial distribution of mountain permafrost on a micro-scale through detailed and intensive field surveys. These field surveys include the DC resistivity imaging techniques, which has been recently used to map the distribution of mountain permafrost in the European mountains (Hauck *et al.*, 1999; Vonder Mühll *et al.*, 2001) and Himalaya (Ishikawa *et al.*, 2001). In chapter 6, an attempt to spatially model the mountain permafrost in the summit areas of the Daisetsu Mountains is presented incorporating the use of Geographical Information System (GIS) and a precise Digital Elevation Model (DEM). A map showing the distribution of mountain permafrost on a micro-scale is also presented. This map was verified by field evidence as described in chapter 5. The map is used to discuss the future distribution of mountain permafrost across the study area with respect to the latest available GCM data. Conclusions of the study are summarized in chapter 7.

## Chapter 2 Physical Settings of the Daisetsu Mountains

### 2-1. Topography and Geology

The Daisetsu Mountains are located in the central Hokkaido, northern Japan (fig. 2.1). They form part of the Daisetsuzan National Park, which occupies an area of about 230,000 ha and is the largest one of the Japanese national parks. The study areas extend cover the main part of the Daisetsu Mountains, stretching about 26 km from north to south and about 20 km from east to west.

The Daisetsu Mountains are composed of andesitic lava plateau and a number of volcanic cones constructed on the former, of which Mt. Asahidake at 2290 m ASL, represents the highest summit in Hokkaido (fig. 2.2). Five principle volcanic landforms can be identified: (1) wide and flat lava plateau ranging from 1400 to 1800 m ASL, (2) dome-shaped volcanic cones whose summits are around 2000 m ASL, (3) Ohachidaira crater about 2 km in diameter, (4) Asahidake strato-volcano and (5) large-scale landslides.

Four major lava plateaus can be identified, Takanegahara, Goshikigahara, Numanohara and Koganegahara (fig. 2.2), located in the central part of the Daisetsu Mountains, the southeastern part, southeastern part and the southwestern part, respectively. The major dome-shaped volcanoes are Hokuchindake (2244 m ASL), Kurodake (1984 m ASL), and Hakuundake (2230 m ASL) in the northern part and Tomuraushiyama (2141 m ASL) in the southern part. A number of landslides are distributed around the flat surface and gentle slopes. For example, on the east of Takanegahara and on the north and south of Goshikigahara, large-scale landslides of more than 100 ha can be found consisting of long and steep scarp, landslide blocks and depressions (Takahashi, 1983; 1985).

Some periglacial geomorphic features are observed on the flat summit area. Patterned ground, hummocky topography, frost crack and block slopes are observed in the area of wind-blown debris (Koaze, 1965; Sone and Takahashi, 1986; Fukuda and Sone, 1992; Ishikawa and Hirakawa, 2000). Palsas are found in mires at 1710 m ASL south of Mt. Hiragatake (Takahashi and Sone, 1988). Block slope features are present on the northern slopes of Mt. Chubetsudake, Mt. Hakuundake and Mt. Tomuraushiyama (Takahashi, 1985; Ishikawa and Hirakawa, 2000). The occurrence and development of these features

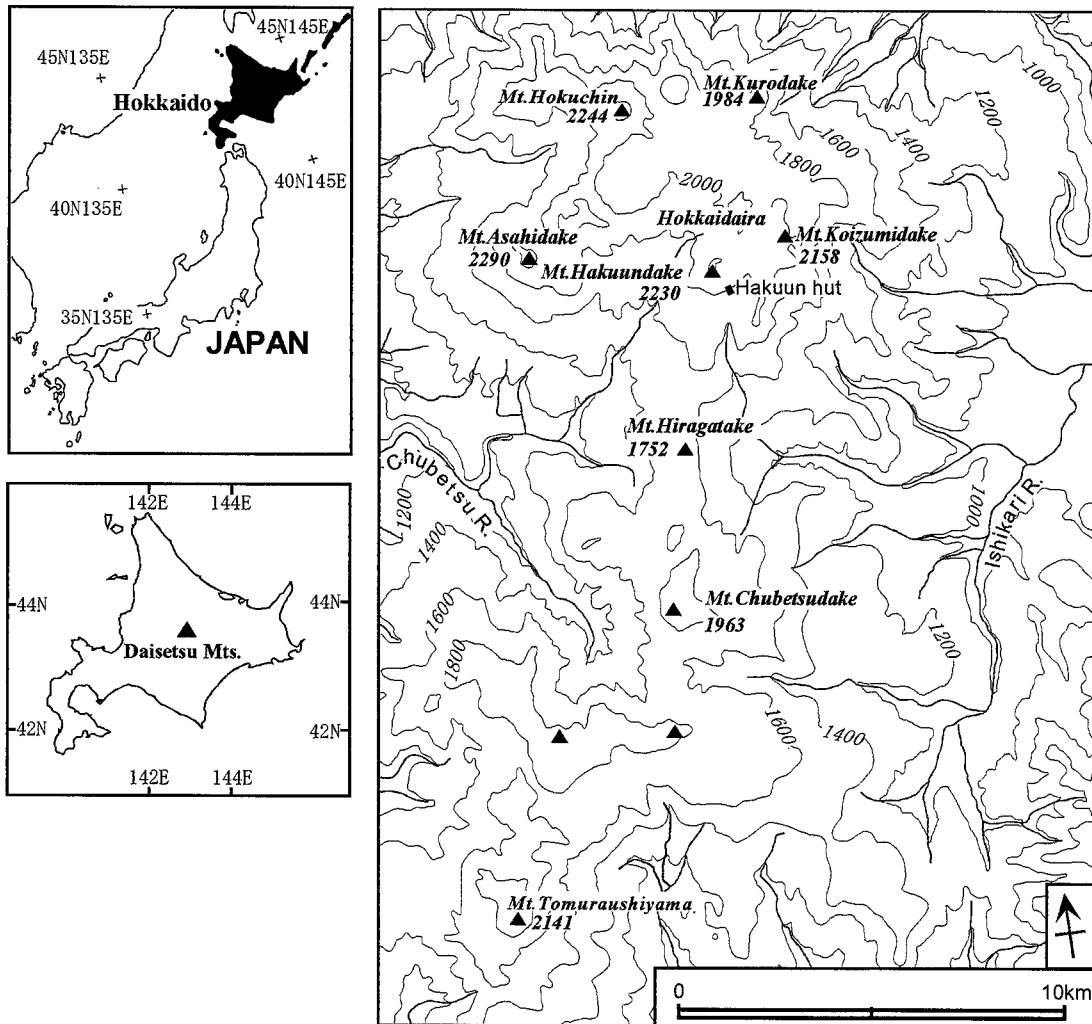


**Fig. 2.1** Location and map of the Daisetsu Mountains **A:** Mt. Hakuundake and its surroundings. **B:** Mt. Chubetsudake and its surroundings.

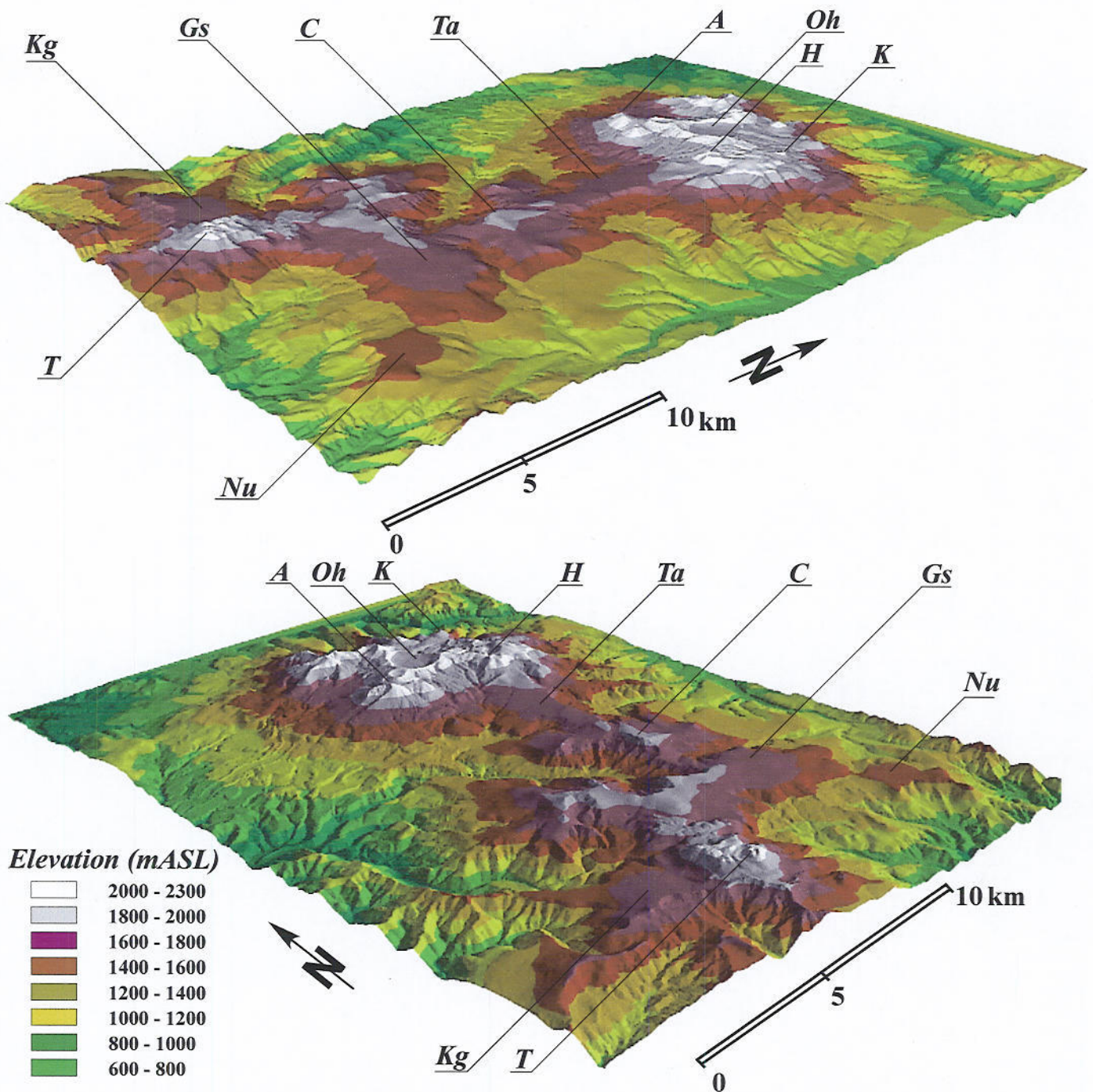


**Fig. 2.2** Landform of the Daisetsu Mountains (Digital Elevation Model). (a) Bird-eye's view from southeast; (b) Bird-eye's view from southwest. A: Mt. Asahidake (2290 m ASL), H: Mt. Hakuundake (2230 m ASL), K: Mt. Kurodake (1984 m ASL), C: Mt. Chubetsudake (1963 m ASL), T: Mt. Tomuraushiyama (2141 m ASL), Oh: Ohachidaira caldera, Ta: Takanegahara lava plateau, Gs: Goshikigahara lava plateau, Nu: Numanohara lava plateau, Kg: Koganegahara lava plateau

have been interpreted as a reflection of the presence of permafrost.

## 2-2. Climatic setting of the Daisetsu Mountains

The Daisetsu Mountains are characterized climatically by a high amount of snowfall and strong winds blowing predominantly from the west during winter. The mean annual precipitation measured at a meteorological observatory of Asahikawa, approximately 45 km WNW of the study area, was 1158 mm between 1951 and 1980. Most of the precipitation between November and March is snow. According to Yamada (1982), the maximum snow depth at Asahidake was 200 cm at 1070 m ASL. The snow depths become less at the higher altitudes. Above the timberline, the maximum snow depth was 120 cm on the windward slope of Asahidake. Westerly prevailing wind in winter brings about a large amount of snowfall on the eastern slope. On the eastern slope of Takanegahara lava plateau, snow depth is known to reach a maximum of 30-35 m (Wakahama, *et al.*, 1968; Wakahama, *et al.*, 1969).

The velocity of westerly winds in Japan at the 500 mb, is very high, probably twice as high as that in western Europe (Yoshino, 1968). The mean monthly wind speed at Hakuun hut (2000 m ASL) is 8.6 m/s (Sone and Takahashi, 1988), and 7.1 m/s at the western mid-slope of Mt. Asahidake (1595 m ASL, Yamada *et al.*, 1978). Such speeds are above the critical wind speed of 4-7 m/s needed to blow snow from the slopes (Ohmura *et al.*, 1967; Yamada, *et al.*, 1978). As a result of the strong predominant westerly wind above the timberline leave the flat terrain extensively snow free even in winter (fig.2.3). Snow tends to accumulate mainly on the east-facing leeward slopes, forming snow patches, some of which are perennial.

Air temperature monitoring was carried out at Hakuun hut (2000 m ASL) in 1985, 1987 and 1988 with the mean annual air temperatures for each year records as  $-3.8^{\circ}\text{C}$ ,  $-4.9^{\circ}\text{C}$  and  $-5.2^{\circ}\text{C}$ , respectively (Sone and Takahashi, 1988; Sone and Nakayama, 1992). The negative mean monthly air temperature values were recorded between October and April. In 1985, the lowest monthly mean value of  $-21.3^{\circ}\text{C}$  was recorded in January, whereas the highest value of  $13.9^{\circ}\text{C}$  occurred in August. The freezing index calculated from annual air temperature variation was  $2,600^{\circ}\text{C}\cdot\text{days}$ , which corresponds to a value obtained in Fairbanks, Alaska, in the discontinuous permafrost zone (Sone, 1990). As part of this study additional measurements were taken through 1998 at three

**Table 2.1** Summary of air temperature monitoring through a year in 1999 at Mt. Koizumidake (2135 m ASL), Hakuun hut (2000 m ASL) and Chubetsu hut (1635 m ASL).

Site	Altitude (m ASL)	Mean (°C)	Daily mean of the warmest month (°C)	Daily mean of the coldest month (°C)	Freezing Index (°C.days)	Thawing Index (°C.days)
Mt.Koizumidake	2135	- 4.67	12.81 (Aug.)	- 20.18 (Feb.)	2919	1172
Hakuun hut	2000	- 3.84	13.06 (Aug.)	- 19.39 (Feb.)	2701	1305
Chubetsu hut	1635	- 2.04	14.63 (Aug.)	- 17.48 (Feb.)	2314	1535



**Fig. 2.3** Winter view of the flat summit areas of the Daisetsu Mountains from Hakuun hut (2000 m ASL) to the south (See fig. 2.1 for location).

different altitudes; Mt. Koizumidake (2135 m ASL), Hakuun hut (2000 m ASL) and Chubetsu hut (1635 m ASL) as summarized in table 2.1.

### **2-3. Vegetation**

According to Ito and Sato (1981), the natural vegetation of the Daisetsu Mountains is divided into alpine, subalpine, montane vegetations and others (table 2.2). The alpine vegetation is typically composed of seven communities and four community-complexes. The subalpine vegetation stretches around and below the timberline, and consists of *Sasa kurilensis* and *Alnus maximowiczii* communities, *Betula ermanii* forest, upper mixed forest and coniferous forest from the higher to the lower. The montane forest occupies a comparatively narrow area below 600-800 m ASL. Pioneer *herbaceous* communities occupy the western slope of Mt. Asahidake.

The altitude of the timberline is around 1700 to 1800 m on the eastern side of the mountain, whereas it is only 1300 to 1400 m on the western side (Takahashi, 1990). The terrain above the timberline is only partially covered with the *alpine snow-hostile scrub* community. On the surface of the summit areas, the *alpine wind-blown rocky gravel herbaceous* community is distributed mainly.

**Table 2.2** Actual vegetation of the Daisetsu Mountains  
(after Ito and Sato, 1981).

Natural vegetation	Alpine vegetation	1. Alpine snow-hostil scrub ( <i>Vaccinio-Pinetum pumilae</i> ) 2. Alpine snow meadows (Alpine tall perennial herbaceous communities) 3. Alpine snow-bed communities 4. Alpine wind-blown dwarf scrub ( <i>Arctérico-Leuseleurietum procumbentis</i> ) 5. Alpine wind-blown dwarf scrub ( <i>Arctous alpinus</i> var. <i>japonicus-Vaccinium uliginosum</i> community) 6. Alpine wind-blown rocky gravel dwarf scrub·herbaceous community ( <i>Salici-Oxytropidetum yesonensis</i> ) 7. Alpine wind-blown rocky gravel herbaceous community ( <i>Dicentro-Violetum crassae</i> ) 8. Community complex (4 and 7) 9. Community complex (3 and 4) 10. Community complex (1 and 12) 11. Community complex (1 and 14)
	Subalpine vegetation	12. <i>Sasa kurilensis</i> 13. <i>Alnus maximowiczii</i> community 14. <i>Betula ermai</i> forest 15. Upper mixed forest 16. <i>Picea jazoensis</i> forest 17. <i>Picea jezoensis</i> · <i>Abies sachalinensis</i> forest 18. <i>Picea glehnii</i> forest 19. <i>Picea glehnii</i> · <i>Pjezoensis</i> · <i>Abies sachalinensis</i> forest
	Montane vegetation	20. <i>Populus maxmowiczii</i> · <i>Toisusu urbaniana</i> forest 21. Lower mixed forest of conifers an broadleaf trees 22. Montane broadleaved forest 23. <i>Ulmus davidiana</i> var. <i>japonica</i> · <i>Cercidiphyllum japonicum</i> forest 24. <i>Salix spp.</i> forest 25. <i>Quercus mongolia</i> var. <i>grosseserrata</i> forest 26. <i>Betula spp.</i> forest 27. Upland meadows
	Others	28. Pioneer herbaceous communities on active volcanos 29. High moor
Anthropogenic vegetation and others	30. <i>Cutovar</i> land 31. Man-made forest 32. Abandoned field 33. Artificial grassland 34. Urban sites 35. Open water 36. Non-vegetation-cover 37. Perennial snowdrift glacier	

## Chapter 3 Field Survey Methods

### 3-1. Combined use of indirect prospecting

In order to map and characterize mountain permafrost, a number of geophysical techniques and ground temperature measurements have been applied (e.g. King *et al.*, 1992; Vonder Mühll *et al.*, 2001). King *et al.* (1992) categorized survey methods into direct and indirect observations. Direct observations include borehole drilling together with ground temperature monitoring through a year, while indirect observations include BTS measurements and geophysical surveys such as DC resistivity and shallow seismic soundings. Continuous temperature monitoring through the deep borehole provides the most accurate information about ground thermal conditions at a particular site, although drilling in mountain permafrost areas is usually difficult and extremely expensive. Accordingly, indirect methods are widely used and become practical in mountain areas. Although geophysical methods do not provide direct proof of permafrost presences, they allow one to measure certain physical properties of subsurface materials, such as DC resistivities and P-wave velocities. These indicators should be verified and supported by the results of other geophysical and/or thermal prospecting.

The occurrence of permafrost in the Daisetsu Mountains has been investigated primarily through direct methods such as drilling and ground temperature monitoring (Fukuda and Kinoshita, 1974; Sone, 1990). Geophysical investigations have also been applied complementing the direct investigations (Fukuda and Sone, 1992).

Within this study a combination of indirect methods were used to survey the permafrost over a wide area. DC resistivity and thermal prospecting methods were carried out at the same site consisting of 1) DC resistivity sounding and BTS measurements; 2) DC resistivity imaging, shallow ground temperature measurements or ground surface temperature monitoring through a year. The survey methods are summarized in table 3.1. Each method offers both advantages and disadvantages, and as such care was taken as to when and where each methodology was used. The combination of shallow ground temperature measurements and DC resistivity imaging was also applied to the delineation of spatial permafrost distribution at a micro-scale.

**Table 3.1** Advantages and disadvantages of survey methods applied in this study. **SGT**: Shallow ground temperature measurements, **AGST**: Annual ground surface temperature monitoring, **BTS**: Bottom temperature of snow cover.

Physical Properties	Method	Limitation of ground condition	Limitation of snow cover
Thermal	SGT	Fine materials	No
	AGST	No	No
	BTS	No	More than 1 m
Resistivity	Sounding	No	No
	Imaging	No	No

### **3-2. Ground thermal prospecting**

Shallow ground temperature (SGT) at a depth of 1.0 or 1.5 m and its profiling can indicate the occurrence of permafrost, since daily air temperature fluctuation is negligible at these depths (e.g. Takahashi, 1995). Ground temperatures were measured through pre-drilled hole by thermistor sensor, which is capable of reading temperatures between  $-30$  and  $200$  °C at a resolution of  $0.1$  °C and with an error less than  $\pm 0.5$  °C.

On the blocky surface, which composed of open-work coarse debris, the ground temperature is difficult to measure by the ways mentioned above. Year-round monitoring of ground surface temperature may be indicative of thermal exchanges through the ground surface. Assuming the thermal equilibrium, the presence of permafrost requires a subzero value of the mean annual ground surface temperature (MAST), because the geothermal flow tends to increase the mean annual ground temperature with depth. Thermal recorders (T&D TR51) were placed at the sites under investigation. The sensors were covered by a thin layer of sand or cobbles in order to negate the effect by direct solar radiation and to ensure good thermal conductivity with the ground surface.

### **3-3. BTS methods**

The BTS method has been used as a standard method to map mountain permafrost in the Alps and Scandinavia (Haeberli, 1973; 1978; Haeberli and Patzelt, 1982; Hoelzle, 1992; Hoelzle *et al.*, 1993; Keller, 1994; Hoelzle, 1994). The principle is based on the insulating properties of sufficiently thick snow cover, which can keep short periodical variations in temperature and radiation away from the ground surface. Consequently, temperature at the bottom of the snow cover is seen to reach an equilibrium in late winter (fig. 3.1). Where permafrost is present, BTS is colder (usually below  $-3$  °C) than in permafrost-free areas (usually warmer than  $-2$  °C). These criteria have been provided empirically (Haeberli, 1973). For BTS measurements to be taken a snow depth of at least 0.8 or 1.0 m is needed (King, 1983; King *et al.*, 1992).

Two kinds of BTS methods were utilized in this study: BTS measurements taken by BTS probes pushed through the snow cover to the ground surface and BTS monitoring using mounted single-channel temperature data loggers (BTS monitoring). The BTS

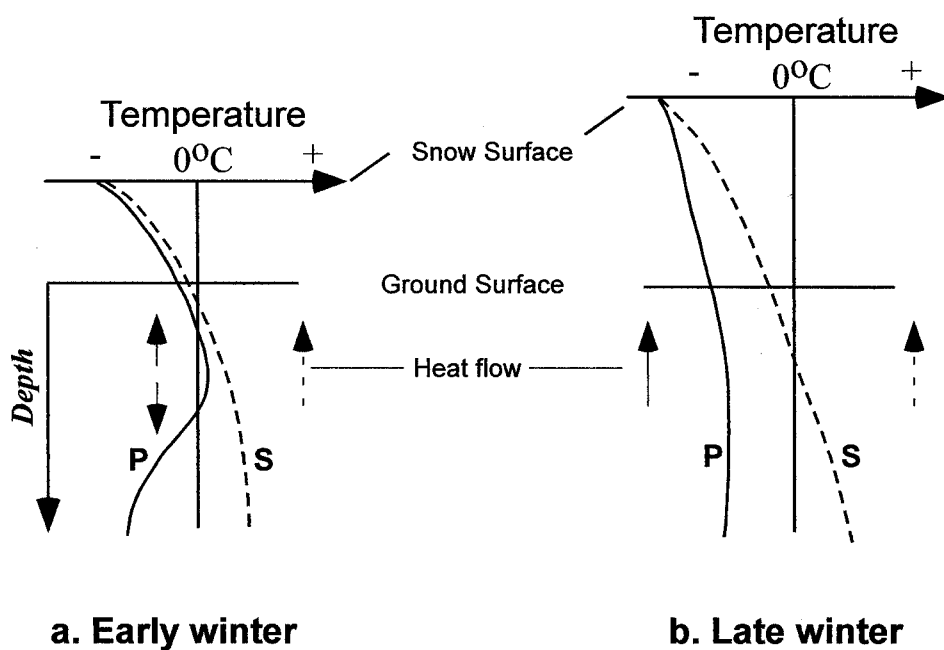


**Fig. 3.1** Schematic temperature profiles of ground and snow cover at a permafrost site (P) and seasonal frost site (S) (After Haerberli and Patzelt, 1982).

monitoring shows the evolution of BTS values, which depend on the thermal characteristics of subsurface materials and annual snow cover history at a site.

BTS measurements were carried out at 41 sites where the snow thickness was more than 1.0 m. In practice, the areas with a suitable thickness of snow cover tend to be restricted above timberline, owing to re-distribution of snow cover by strong wind. BTS can be measured in the following three sites:

- 1) The wind-lee snow covered ground and convex hollows on the flat summit area.
- 2) Shrubbery vegetation patches.
- 3) The coarse blocky surface, where snow accumulates due to the surface roughness.

BTS monitorings were carried out at 11 sites in total. To avoid disturbing the snow cover all of data loggers were installed prior to the first snow fall. Readings were carried out from October 1997 to July 1998 in Mt. Chubetsudake and its surroundings and from October 1998 to July 1999 in Mt. Hakuundake and its surroundings.

### **3-4. DC resistivity prospecting**

#### **3-4-1. Physical background**

The DC resistivity values of unconsolidated sediments are a function of the volumes of debris, pores, water and ice. In particular, the DC resistivity value of ice is considerably higher than those of unfrozen water. Therefore, the DC resistivity value of a frozen material is two or three orders of magnitude higher than that of an unfrozen material (Hoekstra and McNeill, 1973; Harada *et al.*, 1991).

#### **3-4-2. DC resistivity sounding**

DC resistivity sounding involved simple four-electrode arrays (fig. 3.2) and is the most commonly used geophysical technique to identify mountain permafrost (Fisch *et al.*, 1977; King *et al.*, 1987; Barsch and King, 1989; Evin and Fabre, 1990; Vonder Mühl, 1993; Hoelzle, 1993; Evin *et al.*, 1997; Berthling, *et al.*, 1998; Kneisel, 1998; Ishikawa and Hirakawa, 2000). In this study, a total of 12 soundings were carried out from

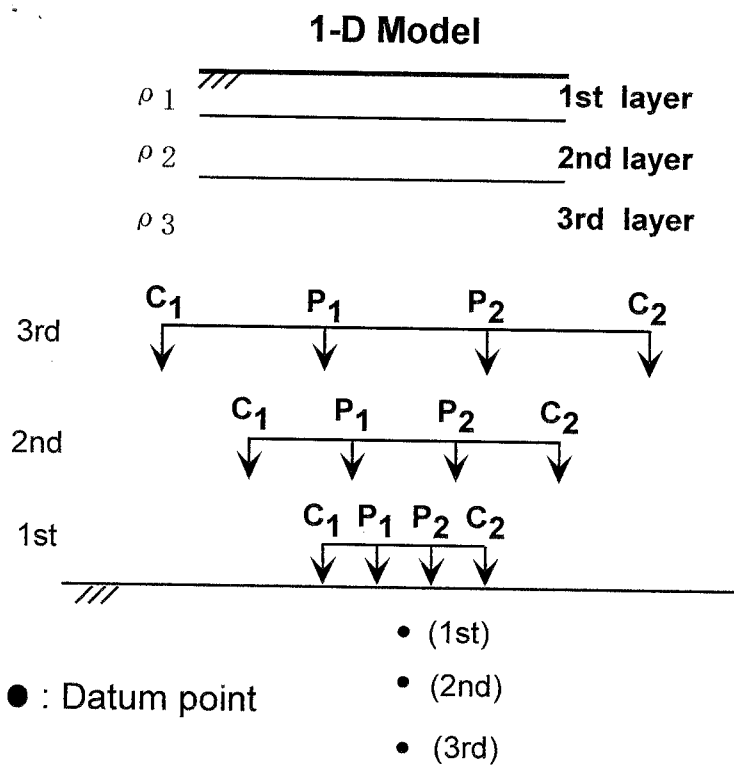


**Fig. 3.2** Schematic diagram showing array configuration of DC resistivity sounding. *P1*, *P2*: Potential electrodes, *C1*, *C2*: Current electrodes.

mid-August to late September 1998. A Wenner electrode array method was applied at all sounding sites using the SYSCAL R1 instruments for current injection and voltage measurement. The maximum spacing of the electrodes depends on the terrain limitations of each sounding site. A DC resistivity model of the sounding site was determined using a fitting model for the apparent resistivity values obtained through vertical variation in the DC resistivity values. The linear filter method (Koefoed, 1979) was used for this calculation. On the basis of the hybrid least square optimization method (Powell, 1970), several iterations were conducted until the RMS (root-mean-squared) error converges. The subsurface stratigraphy was determined primarily through this DC resistivity model. The situation is complicated by the fact that mountain slopes are composed of concave and convex surfaces, so that subsurface structures can display complicated variations even over short distance. Therefore, some problems exist in the interpretation of the data sets obtained by DC resistivity sounding in such areas. King *et al.* (1992) indicated that the 'lateral effect' influences the DC resistivity sounding on rock glaciers and many other mountain permafrost features, resulting on oversteepened graph. With this difficulty in mind, each calculated resistivity layer was then correlated with the subsurface materials on the basis of both the calculated DC resistivity values and the properties of surface and subsurface materials.

General resistivity values summarized by Haeberli and Vonder Mühll (1996) were mainly used to identify frozen materials. The resistivity of frozen materials composed of sand and gravel ranges from  $10^0$ - $10^2$  k $\Omega$  m or more if unfrozen water content is low, while the resistivity of unfrozen materials from 100  $\Omega$  m to 10 k $\Omega$  m. The resistivity of frozen material with high clay content is slightly lower than that of sand-gravel if a considerable amount of unfrozen water is included (Harada *et al.*, 1991; King *et al.*, 1992). The resistivity of unfrozen coarse blocky boulders ranges from several k $\Omega$  m to several 10 k $\Omega$  m (Fisch *et al.*, 1977; King *et al.*, 1987; Barsch and King, 1989). This relatively high resistivity is due to the lack of matrix between blocky boulders that is occupied by air, which has a considerably high resistivity. The overlapping range of resistivity between frozen materials and unfrozen coarse blocky boulders may make some ambiguities.

### 3-4-3. DC resistivity imaging

DC resistivity imaging is a survey technique recently developed for the investigation of areas with complex geology where the use of DC resistivity sounding is unsuitable (Griffiths and Barker, 1993; Loke and Barker, 1995; 1996). This technique gives detail instructions on subsurface structures both horizontally and vertically (fig.3.3), and could be suitable for investigation of mountain permafrost under complicated topography and/or subsurface structure (Hauck and Vonder Mühll, 1999; Ishikawa *et al.*, 2001; Kneisel, *et al.*, 2001; Vonder Mühll, *et al.*, 2001).

Total of 10 lines were surveyed by DC resistivity imaging. A multi-core cable (Griffiths, *et al.*, 1990) has a number of nodes, which determines the potential or current electrodes connected through the extension cable under the control of the remote control multiplexer. The remote control multiplexer is programmed to determine the active electrodes used for each measurement through the multi-core cable. The stacking type digital resistivity-meter, SYSCAL Junior, was used for current injection and voltage measurements. The electrodes connected to the node were placed on the ground surface before the sequence of data acquisition. The steel nets mounted on an outer sponge were used on the coarse blocky surface where installation of the steel sticks is difficult. Due to the poor conductivity, however, a high electrical resistance between this electrode and the ground surface was usually encountered. Sometimes, this causes problems such as an insignificant electrical current and unstable potential values. To minimize such an electrical resistance, each electrode was saturated by salt water. Furthermore, two or three extra electrodes were connected to one end of the extension cable in parallel. The noise level was normalized by more than 10 times stacking at one measuring point.

For electrode configuration, two electrode arrays were considered; Dipole-dipole and Wenner-Schlumberger arrays. A Dipole-dipole array is useful for detecting vertical subsurface structures, whilst a Wenner-Schlumberger array is more useful for horizontal subsurface structures (Vonder Mühll *et al.*, 2001). For this study preliminary measurements were taken using both electrode arrays at some site and it was found that the Dipole-dipole array produce higher noise level than that of the Wenner-Schlumberger array. It was decided therefore to use the Wenner-Schlumberger array, which is a hybrid of the Wenner and Schlumberger arrays (Padzerik and Braha, 1996). The apparent electrical resistivity  $\rho_a$  ( $\Omega$  m) is calculated by the following

formula:

$$\rho_a = KV/I \quad (3-1)$$

where  $V$  is the measured potential in mill volts, and  $I$  is the injected current in milliamp.  $K$  is the geometrical coefficient calculated by the following formula:

$$K = \pi n(n+1)na \quad (3-2)$$

where  $n$  and  $a$  are the parameters related to the electrode array configurations ( $n = 1, 2, 3, \dots$ , and  $a$  is the unit electrode spacing in meters). The obtained resistivity values calculated with high standard deviation (more than 50 %) and abnormally high or low values were excluded prior to data analysis.

The apparent resistivity data were contoured in the form of a pseudo-section, which gives an approximate picture of the subsurface resistivity. The inverted resistivity models, which approximately indicate the distribution of resistivity in the subsurface, were processed by the software program, RES2DINV ver 3.4 (Loke and Barker, 1996). Several iterations based on the non-linear least square calculation were conducted until the RMS error converged and reached a minimum. The inverted resistivity tomograms show the model resistivity section. High gradients of resistivity values usually characterize a contact zone between different resistivity bodies.

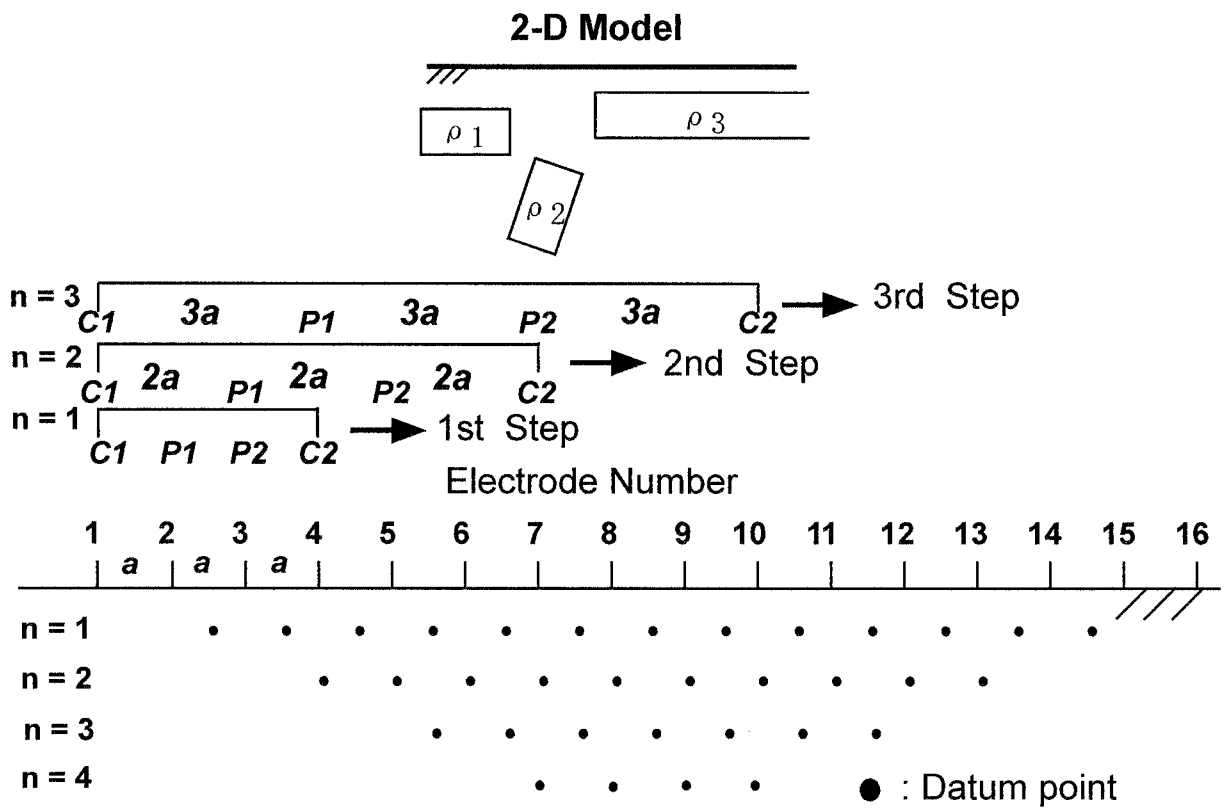


**Fig. 3.3** The arrangement of electrodes for DC resistivity imaging and the sequence of measurements used to build up a pseudosections. *a*: Spacing of electrodes, *P1*, *P2*: Potential electrodes, *C1*, *C2*: Current electrodes.

## **Chapter 4 Permafrost Distribution beneath Snow Cover**

### **4-1. Introduction**

This chapter focuses on the occurrence of permafrost beneath snow cover in the Daisetsu Mountains. BTS and DC resistivity soundings were applied for this purpose. In the Daisetsu Mountains, distribution of permafrost and the associated thermal regimes have only been studied on wind-blown ground. In such areas the near total absence of snow cover means that winter frost can penetrate deeply into the ground surface and thus air temperature can be seen have a directly affect on the ground thermal regimes. Areas with such conditions are suitable for permafrost growth if MAAT is below 0 °C. These situations are not like those in the European mountains, where permafrost beneath snow cover have been mapped at a number of sites (*e.g.* Imhof, *et al.*, 2000).

Recently, the combined BTS surveys using both mapping and monitoring have shown significant differences in the evolution of BTS value throughout winter, depending on the thermal characteristics of surface materials and annual snow cover history at a site (Keller and Gubler, 1993; Hoelzle, 1999; Imhof, *et al.*, 2000). This suggests that application of BTS to other mountains areas with different climatic conditions requires caution. Since no attempt has been undertaken to map the permafrost distribution in the Daisetsu Mountains by means of BTS method, the spatial and temporal characteristics of BTS values and thus its applicability to map the permafrost distribution, is unclear.

The primary aims of this chapter are to clarify the occurrence of permafrost beneath snow cover in the Daisetsu Mountains. The secondary aim is to examine the BTS criteria (Haeberli, 1973) in the Daisetsu Mountains. For these purposes, field investigations by DC resistivity sounding, BTS mapping and BTS monitoring were carried out at a number of sites.

### **4-2. Study areas**

Four main study areas were investigated in this study located on the southwest and northwest-facing block slope of Mt. Chubetsudake (1963 m ASL), the north-facing slope of Mt. Hakuundake (2230 m ASL) and the Mt. Hakuundake volcanic crater (fig.4.1). The southwest-facing block slope of Mt. Chubetsudake (fig. 4.1) is located at

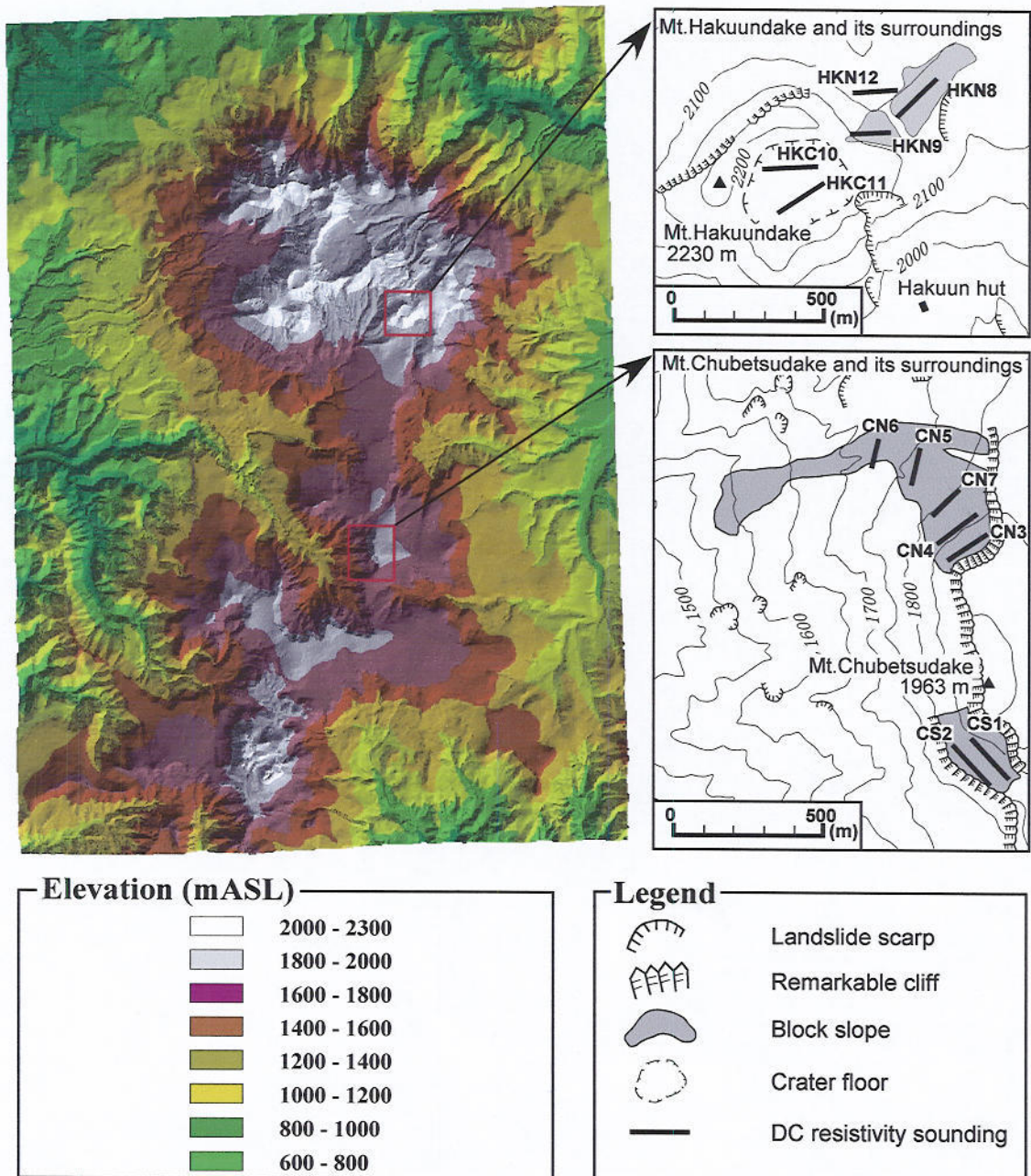


**Fig. 4.1** The locations of DC resistivity soundings and BTS measurements around Mt. Chubetsudake and Mt. Hakuundake.

the foot of a steep bedrock cliff with a height of approximately 100 m. The area covered with boulders extends from 1870 m down to 1790 m ASL with a length of 150 m and a width of 270 m (fig. 4.1). Large blocks at the surface show an openwork texture. In early April 1998, snow thickness was between 1.0 and 2.5 m.

The northwest-facing block slope of Mt. Chubetsudake (fig. 4.1) extends from 1870 m down to 1560 m ASL with a maximum length of 1300 m and a width of about 450 m. Transverse furrows and ridges are formed on the surface above 1700 m ASL. The deposits display an openwork texture with blocky coarse boulders, in places reaching more than 10 m in diameter. Alpine snow-hostile scrub (mainly *Pinus pumila*) and lichen mat partly cover the surface of this block slope. Takahashi (1985) studied the origin of this block slope and concluded that the origin was a rockslide-avalanche formed several hundred years ago. However, the presence of permafrost on this block slope has not yet been discussed. Snow thickness in early April 1998 ranged from 1.0 to 2.0 m on the ridge of this slope, while more than 3.0 m within the furrow. The snow remains on the debris slope below the cliff and within the transverse furrows until early summer.

On the north-facing slope of Mt. Hakuundake (fig. 4.1), two blockstreams have developed indicating down slope movement. One blockstream consisting of andesitic boulders occupies the eastern part of the slope extending from 2140 m ASL down to 2090 m with a length of approximately 180 m and a width of 250 m. The relative height of this front slope ranges from approximately 4 m to 20 m with an inclination ranging between 30° and 40°, which is the angle of repose for boulders. This block slope is composed of matrix-free andesitic boulders with alpine snow-hostile scrub (mainly *Pinus pumila*) scattered on the surface. The second block stream occupies the western part of the slope extending from 2160 m ASL down to 2110 m (fig. 4.1). It is approximately 120 m in length and 80 m wide. The relative height of the front slope is several meters. The surface is covered with *Pinus pumila* and soil, whereas the front slope is less vegetated and has an openwork texture. Snow thickness was between 1.0 and 2.5 m in early April 1998 on the north-facing slope. The snow cover remains until early summer in the eastern part, but is gone from the western part by mid-spring.

Frost crack and earth hummocks are very prevalent the Mt. Hakuundake crater floor (fig. 4.1). Turf-banked terraces and solifluction lobes are present on the northern fringe. Except for the northern fringe, there is negligible snow cover on the Mt. Hakuundake

crater during winter. On the northern fringe a snow thickness of between 1.0 and 2.5 m was recorded in early April 1998, with less than 0.5 m recorded on the crater floor.

### **4-3. Results and Interpretations**

#### **4-3-1. Spatial BTS variations**

The spatial variations of BTS, including the minimum values obtained by BTS monitoring at three sites, are shown in fig. 4.2. At the sites on Mt. Chubetsudake and its surroundings, spatial variations of BTS values were obtained on April 14 and 15, 1998.

On the northwest-facing slope of Mt. Chubetsudake, BTS values ranged from 0.0 to  $-4.4$  °C. Two BTS values monitored at 1860 m and 1750 m elevations indicate values of  $-3.0$  and  $-8.4$  °C, respectively. As results, two zones with low values were detected: one between 1750 m and 1800 m ASL, and the other at 1860 m ASL. On the southwest-facing slope of Mt. Chubetsudake, BTS values were  $-2.5$ ,  $-4.4$  and  $-4.8$  °C. A value of  $-15.5$  °C was recorded during late-February and March by BTS monitoring.

On Mt. Hakuundake and its surroundings, BTS values ranged from  $-2.6$  to  $-9.8$  °C on the north-facing slope, and from  $-1.2$  to  $-3.1$  °C on the south-facing slope (fig. 4.2). The extremely low BTS values are found at some sites on the northern slope. On the Mt. Hakuundake volcanic crater, BTS measurements were unavailable due to the lack of snow cover.

#### **4-3-2. Temporal BTS variations**

In Mt. Chubetsudake and its surroundings, BTS monitoring has been conducted at three sites: two sites were set at elevations 1860 m and 1755 m ASL on the northwest slope of Mt. Chubetsudake, with the third 1830 m ASL on the southwest slope (figs. 4.1). All monitorings were conducted on the openwork blocky surface (table 4.1). One logger was installed in a transverse furrow (fig. 4.1, site CN5); one on the top of a ridge (fig. 4.1 site CN3); one is in the depression below a talus slope (fig. 4.1, site CS1). In Mt. Hakuundake and its surroundings, BTS monitoring had been conducted at 8 sites in total; one is on the openwork block slope; four are in the patch of *Pinus pumila*; three are on the snow bed where snow remains until summer (table 4.1).

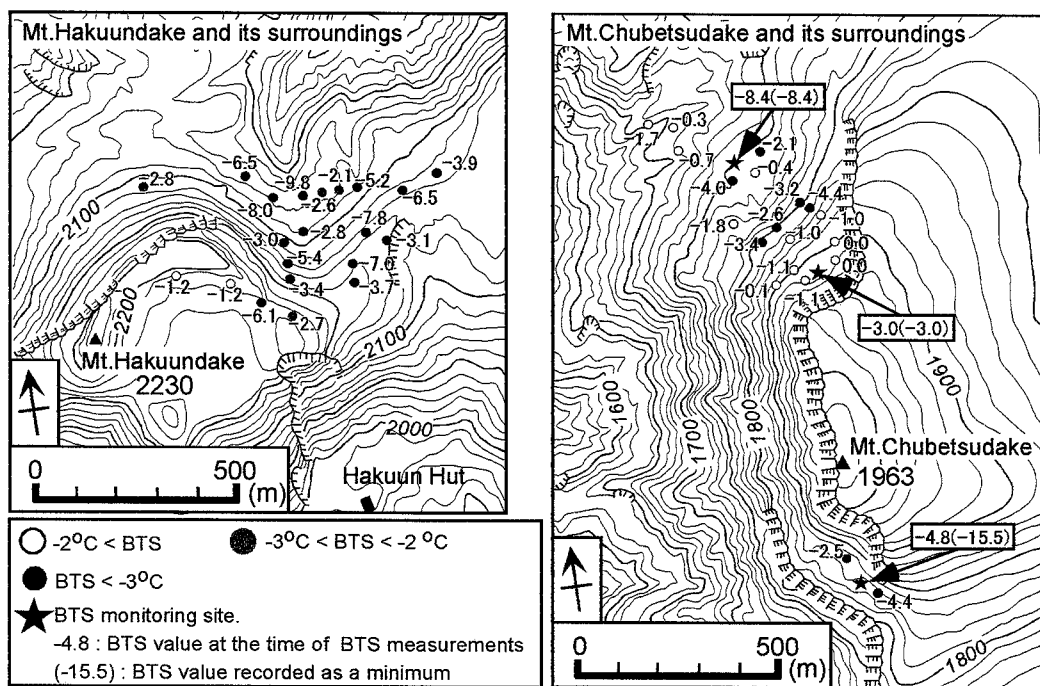


**Fig. 4.2** Spatial variation of BTS values in early April, 1998  
(See figs. 4.1 for the locations)

**Table 4.1** Characteristics of the site for BTS monitoring

Area	Site	Surface materials and topography
Mt. Chubetsudake NW Slope	CN3	Openwork boulders, ridge
	CN5	Openwork boulders, furrow
Mt. Chubetsudake SW Slope	CS1	Openwork boulders, Depression hollow
Mt. Hakuundake and its surroundings	HK1	Openwork boulders
	HK3	<i>Pinus pumila</i> patch
	HK6	Snow patch, sand-gravel
	HK18	Snow patch, sand-gravel
	HK19	<i>Pinus pumila</i> patch
	HK20	<i>Pinus pumila</i> patch
	HK27	Snow patch, sand-gravel
HK29	<i>Pinus pumila</i> patch	

Fig. 4.3 shows the temporal variations derived from BTS monitoring. At the sites around Mt Chubetsudake, BTS values indicated that daily fluctuations occurred during autumn 1997 and from late spring or summer 1998. By contrast, BTS values did not fluctuate from early to late winter, and remained constant at 0 °C from early spring to early summer. As mentioned previously, the mean annual monthly air temperatures increased during April in this mountain. An increase in snow temperature and the constant value at 0 °C from early spring to early summer was due to seasonal snow melting. In early spring 1998 the thickness of snow cover was observed to be more than 1.0 m at the three BTS monitoring site and their surroundings. Furthermore, BTS values between mid-October and late-March did not show daily fluctuations. These results suggest that BTS values were not affected by daily air temperature fluctuations. BTS evolutions of CS1 and CN5 showed similar general behavior. Until early-December 1997 to mid-March, temperatures were seen to decrease. Thereafter, BTS remained constant at minimum values through to the onset of snowmelt. BTS evolution of CN3 also shows slightly similar behavior with CS1 and CN5 sites, although some fluctuations are observed.

The observed temporal ground surface temperature in the Mt. Hakuundake and its surroundings is shown in fig. 4. 3. BTS evolutions obtained at the sites HK6, HK18 and HK27 did not show daily fluctuation and remain constant nearly at 0 °C in all winter 1998, 1999 and 2000. BTS evolution at the site HK29 also did not show the daily fluctuation. However a small decrease in temperature was observed. The minimum BTS values at site HK29 was -4.5 °C. BTS evolution obtained at the sites HK1, HK3, HK19 and HK20 showed daily fluctuations. These evolutions also showed the annual trigonometric temporal variation, suggesting that BTS are affected by annual air temperature fluctuation.

#### **4-3-3. DC resistivity sounding and Permafrost Occurrence**

##### **4-3-3-1. Mt. Chubetsudake and its surroundings**

The sounding curves and estimated subsurface electrical stratigraphy obtained from Mt. Chubetsudake and its surroundings are shown in fig. 4.4. These soundings were carried out over blocky boulders with an open-work texture.

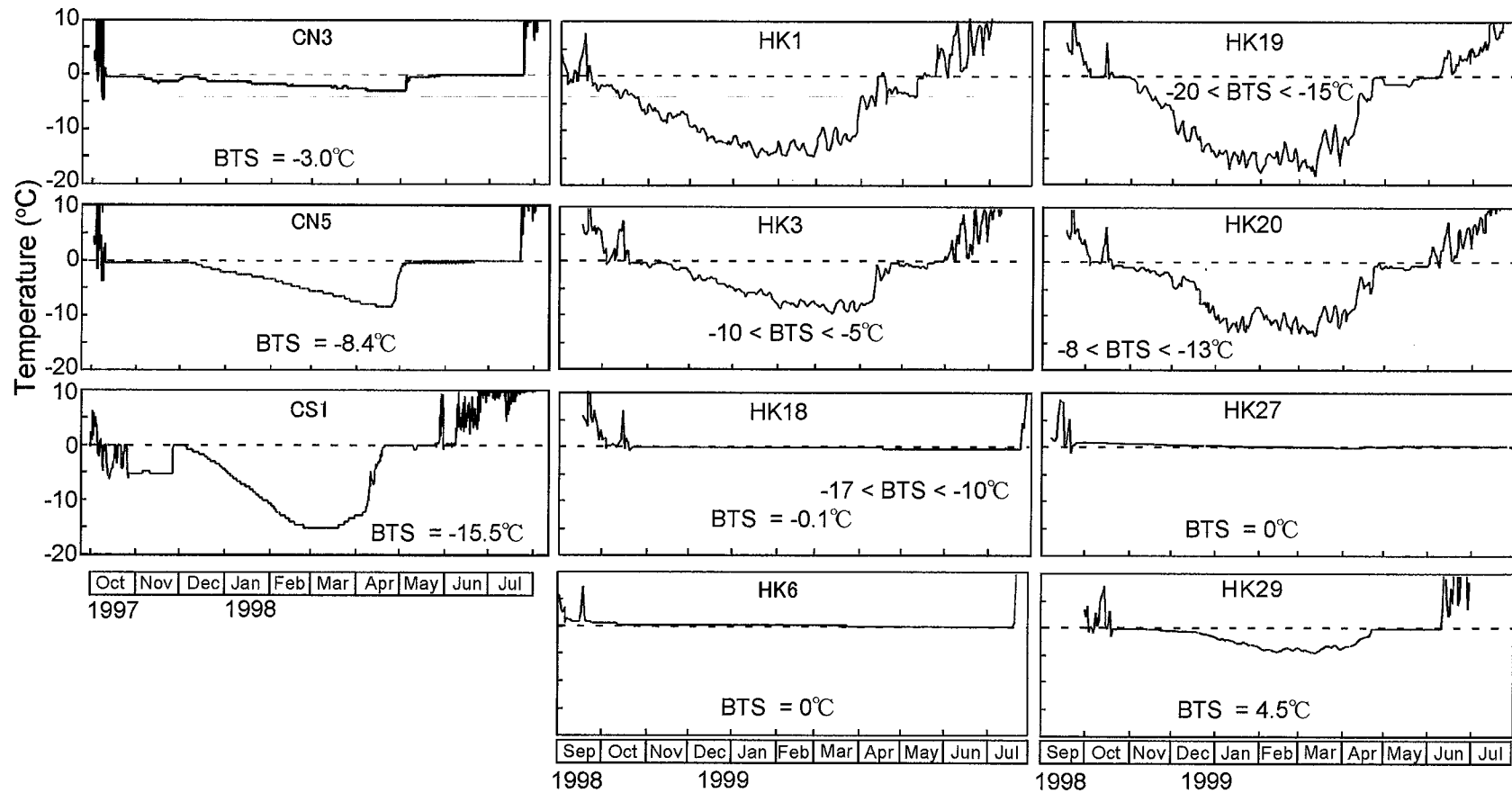


**Fig. 4.3** Results of BTS monitoring. The BTS values are also shown in diagram.

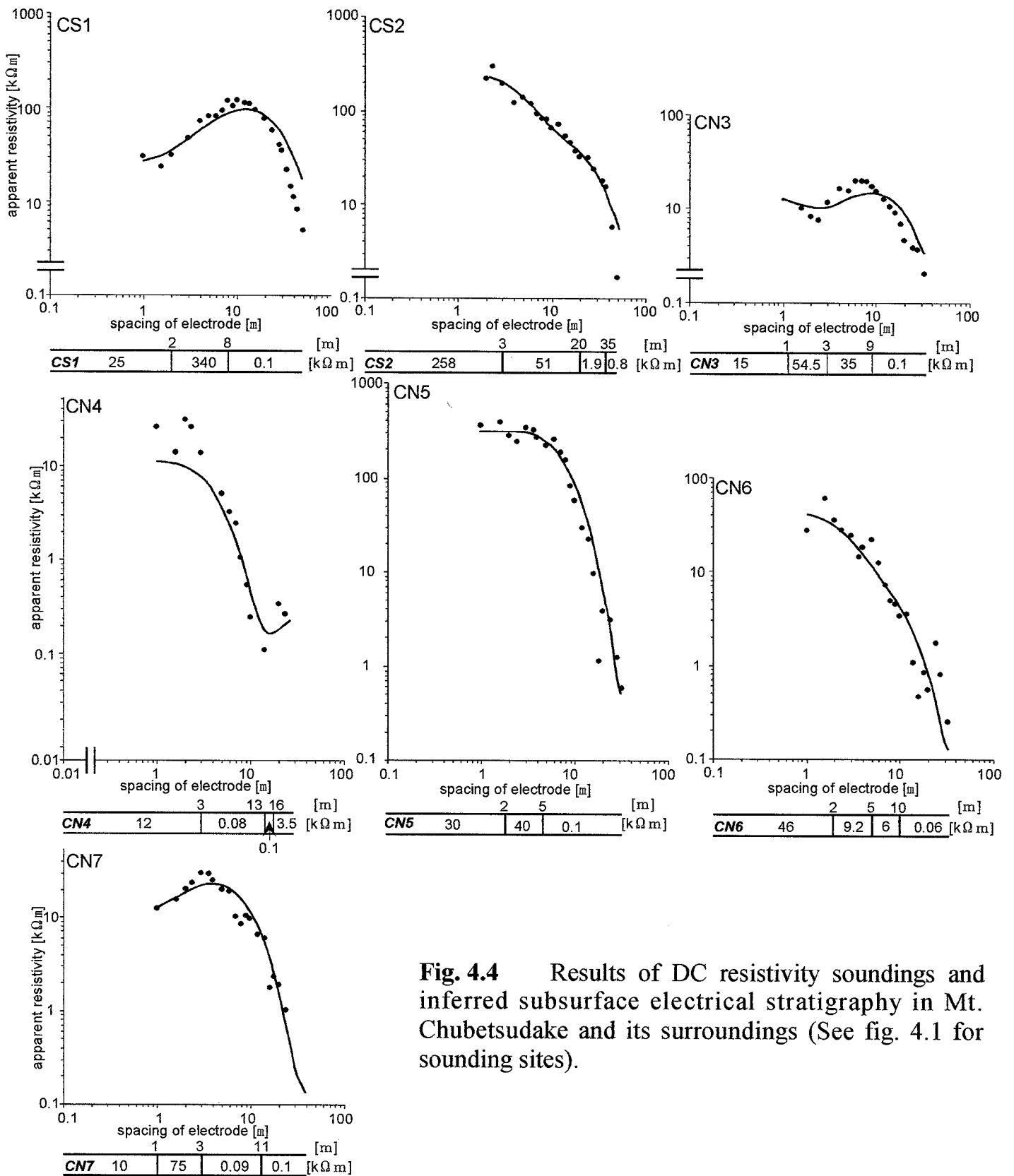


**Fig. 4.4** Results of DC resistivity soundings and inferred subsurface electrical stratigraphy in Mt. Chubetsudake and its surroundings (See fig. 4.1 for sounding sites).

Sounding at site CS1 resulted in the identification of three layers. The first layer corresponds to surface blocky boulders. The resistivity of the second layer represents frozen sandy or gravely material 6 m in thickness, and this layer is considered to be a permafrost layer. The third layer should be unfrozen because calculated resistivity values are low.

The sounding at site CS2 indicated four layers. The high resistivity of the first layer suggests the existence of frozen materials (3 m thick, with a resistivity of 258 k $\Omega$  m). Since no frozen material was found between boulders beneath the ground surface during field observation, the thickness of the frozen layer must be less than 3 m. Although the resistivity of the second layer suggests the existence of frozen material, a rapid drop in apparent DC resistivity values does not indicate an obvious contrast between frozen and unfrozen materials. The relatively high resistivity value of the second layer (51 k $\Omega$  m) is influenced by the steep slope near this site. This layer, therefore, is interpreted to correspond to unfrozen blocky boulders. The third and fourth layers are also unfrozen.

Sounding at site CN3 indicated four layers. The first layer corresponds to surface blocky boulders. The marked increase in the apparent resistivity from a depth of 2 m to 7 m indicates the existence of higher resistivity material than the surface unfrozen material. Calculated resistivities are 54.5 k $\Omega$  m and 35 k $\Omega$  m, which are in the range of frozen sand or gravel. The second and third layers are considered to be permafrost layers. The fourth layer (more than 23 m thick, with a resistivity of 0.1 k $\Omega$  m) seems to be unfrozen.

The sounding at site CN5 indicated three layers. The resistivity of the first and second layers (30 and 40 k $\Omega$  m) suggests that these layers are composed of either frozen material or unfrozen coarse boulders. It is difficult to determine this layer is permafrost or not by the value of DC resistivity alone. Resistivity values of the third layer were not in the range of frozen material.

The sounding at site CN7 indicated four layers. The first layer corresponds to unfrozen blocky boulders based on resistivity values and field observation of the surface materials. The higher resistivity of the second layer (2 m thick, with a resistivity of 75 k $\Omega$  m) compared with that of the first suggests the existence of frozen sand or gravel. However it is difficult to determine that this layer corresponds to permafrost, because the thickness of this layer is thin. A rapid drop in apparent resistivity values below a depth of 7 m indicates the absence of frozen material.

The result of the soundings at sites CN4 and CN6 did not indicate the existence of frozen materials.

#### **4-3-3-2. Mt. Hakuundake and its surroundings**

Five sounding curves and corresponding subsurface electrical stratigraphy are shown in fig. 4.5. Soundings at sites HKN8 and HKN9 were carried out on boulders while the soundings at HKN12, HKC10 and HKC11 were on earthy fine materials.

The sounding result at site HKN8 indicated five layers. The first and second layers correspond to unfrozen layers of boulders. An increase in apparent resistivity between 3 m and 16 m depth indicates the existence of higher resistivity materials than those of the first and second layers. The calculated resistivity of the third layer (6 m thick, with a resistivity of  $100 \text{ k}\Omega \text{ m}$ ) suggests the existence of frozen material, which could represent a permafrost layer. On the other hand, the resistivity decreases below a depth of 18 m and the calculated resistivities for the fourth and fifth layer are considerably lower than that of the third layer.

The sounding result at site HKN9 indicated five layers. The first layer corresponds to unfrozen soil or humus that covers the blocky coarse boulders, while the second layer corresponds to unfrozen or frozen blocky coarse boulders. Resistivities of the third and fourth layers range within the value of frozen sandy gravel, while the fifth layer is not in the range of frozen material. The thickness of the frozen layer at this site is between 14 m and 15 m and third and fourth layers correspond to permafrost.

The sounding result at site HKN12 indicated four layers. The first layer corresponds to unfrozen fine material. Due to the presence of fine material containing an amount of unfrozen water, the resistivities of the first and second layers are slightly lower than those of the first and third layers at site HKN8 locating on the blockstream. The resistivity of the second layer is slightly higher than that of the first. This layer corresponds to permafrost, which is composed of frozen fine material containing a considerable amount of unfrozen water. No frozen materials were detected within the fourth layer.

The sounding result at site HKC10 indicated five layers. The relatively high resistivity of the first layer (3 m thick, resistivity  $16 \text{ k}\Omega \text{ m}$ ) suggests the existence of frozen material within this layer. The second, third and fourth layers are in the range of

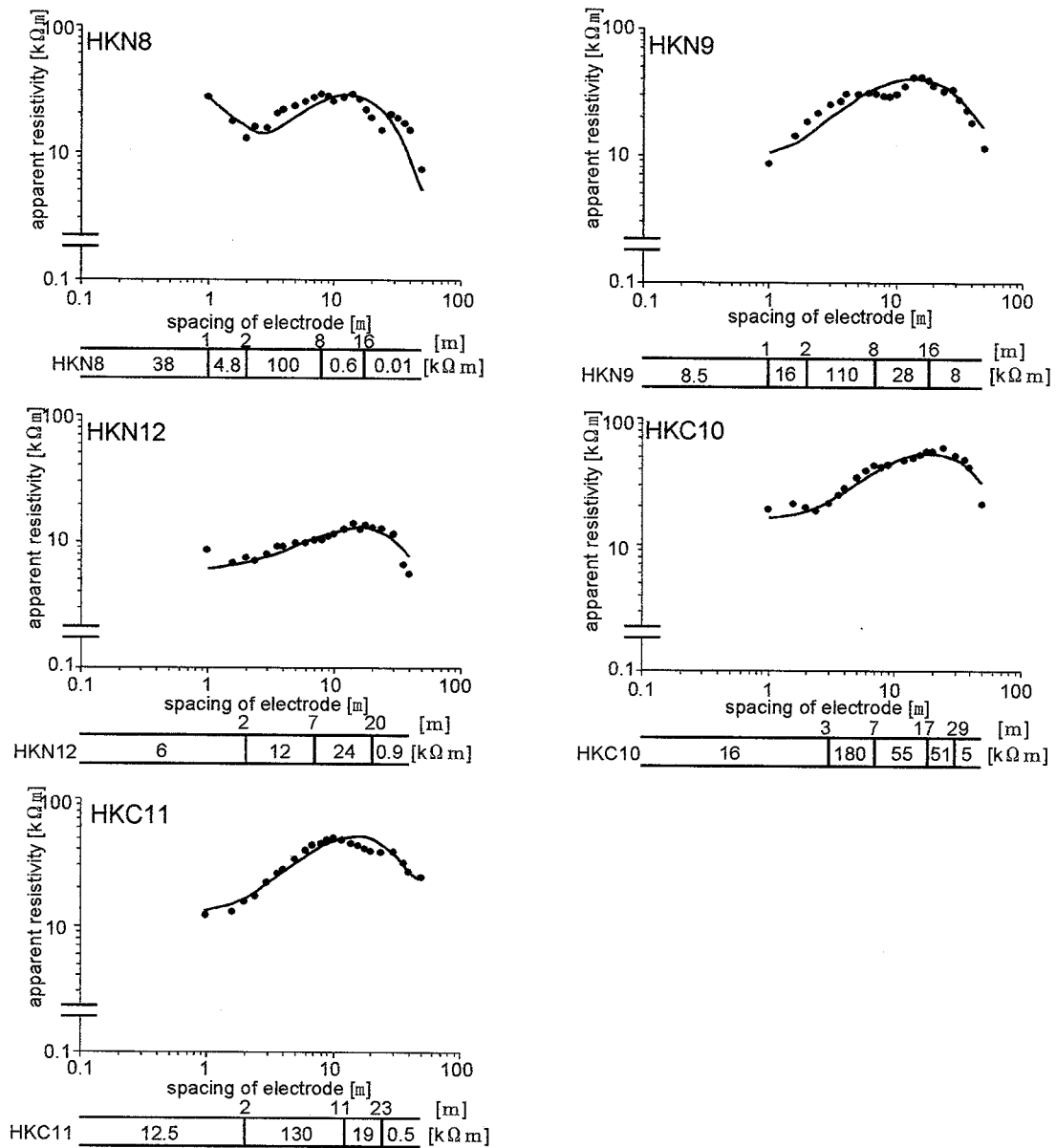


**Fig. 4.5** Results of DC resistivity soundings and inferred subsurface electrical stratigraphy beneath Mt.Hakuundake and its surroundings (See fig. 4.1 for sounding sites)

frozen material with a total thickness of 26 m. These layers are interpreted to be permafrost.

The sounding result at site HKC11 indicated four layers. The first layer, 2 m thick with a resistivity of 12.5 k $\Omega$  m, suggests the existence of frozen material. The second and third layers are in the range of frozen material with a total thickness of 21 m. These layers are interpreted to correspond to permafrost.

#### **4-4. Three temporal BTS variations and thermal processes beneath snow cover**

The BTS evolutions can be divided into three categories depending on their temporal variations:

- (1) The first category includes the sites CN3, HK6, HK18 and HK29, which show no daily fluctuation and are nearly constant during winter.
- (2) The second category includes the sites HK1, HK3, HK19 and HK20. These show both daily and annual variations even beneath snow cover during winter.
- (3) The third category includes the sites CS1 and CN5, which show no daily fluctuations and gradually decreasing until snow melting. Note that extremely low BTS values were obtained as  $-15.5$  and  $-8.4$  °C in CS1 and CN5, respectively.

In category (1), the thick snow cover prevents ground surface from daily air temperature variation. Consequently, BTS reaches an equilibrium with subsurface ground temperature in the late-winter and thus probably shows a one-dimensional thermal equilibrium (Haeberli and Patzelt, 1982; fig. 3.1). On the sites of HK6, HK18 and HK27, BTS values were nearly 0 °C, suggesting that that no perennial frozen materials were present subsurface. In contrast, the minimum BTS values at sites CN3 ( $-3$  °C) and HK29 ( $-4.5$  °C) indicate the existences of frozen materials. The differences in the BTS values are probably derived from the differences in the cooling effect during autumn. During October, subzero temperatures occurs at the sites CN3 and CN29, that is not the case at sites HK6, HK18 and HK27.

In category (2) daily temperature fluctuations were observed. The site HK1 lies on the block slope where the thickness of snow cover varies over a short distance (fig. 4.6). Winter cold heat can conduct through some large blocks, which exposed to atmosphere



**Fig. 4.6** The BTS monitoring site on the north-east facing slope of Mt. Hakuundake (HK1). Some blocks exposed above the snow cover. (The arrow indicates the site of BTS monitoring).

above snow cover. A similar explanation can be applied to the daily temperature fluctuation observed at the sites HK3, HK19 and HK20, which lie on the patches of *Pinus pumila* surrounded by wind blown grounds.

In category (3), the ground temperature decreases between November and March. These cooling trends can be explained by the existence of subsurface frozen materials. However, it is difficult to explain the one dimensional thermal equilibrium at the sites CS1 and CN5, because the minimum BTS values are extremely low,  $-15.5$  and  $-8.4^{\circ}\text{C}$ , respectively. Referring to near subsurface annual ground temperatures ( $-3.1^{\circ}\text{C}$  at 100 cm depth,  $-2.9^{\circ}\text{C}$  at 150 cm at 1710 m ASL) obtained by Sone (1990), these extremely low temperatures are unlikely to be under the condition of the one-dimensional thermal equilibrium with subsurface as shown by Haeberli and Padzelt (1982). Since these sites are located on openwork coarse debris (mostly large boulders) and topographically in the depression, subsurface cold air probably easily flows down and concentrates on these sites. This consideration can be supported by the observations on the rock glaciers in the Swiss Alps. BTS values on transverse furrows are lower than those of ridges, suggesting that subsurface cold air flow occurs between boulders (Bernhald, *et al.*, 1998; Hoelzle, 1999).

#### **4-5. BTS criteria and permafrost occurrences in the Daisetsu Mountains**

Using the results of DC resistivity sounding, the relationship between the recorded BTS values and the occurrence of permafrost has been examined empirically taking into account the thermal processes as discussed in the previous section. The relationship between the permafrost occurrence and BTS values is summarized in table 4.2. Permafrost has been found at the following sites where BTS measurements were carried out: HKN9, HKN8 (HK1), HKN12, CN3, CS1 and CN5.

The BTS values around sites HKN9 and HKN8 correspond to the permafrost probable category of Haeberli (1973), and correlated with permafrost occurrence. At the site HKN8, which is located on the same site of BTS monitoring (HK1), direct cold heat penetration is considered to be predominant factor for permafrost development. The BTS values around site HKN12 were  $-2.6$ . Similarly BTS values of  $-3.0$ ,  $-15.5$  and  $-8.4^{\circ}\text{C}$  recorded at sites CN3, CS1 and CN5 also pointed to the presence of permafrost. At the site HKN8, which is located on the same sites of BTS monitoring

**Table 4.2.** Summarized results of BTS measurements and DC resistivity soundings.

Site	Altitude (m ASL)	Surface materials <sup>1</sup>	Estimated thickness of permafrost layers(m)	BTS values (°C)	Permafrost occurrence by Haeberli (1973) <sup>2</sup>
HKN9	2130	SG	14	-5.4/-3.4	A
HKN8	2125	OB	6	-7.8	A
HKN12	2110	SG	18	-2.6/-2.1	B
CN3	1860	OB	6	-3.0	A
CN7	1845	OB	2(?)	-1.1/0.0	C
CS1	1830	OB	6	-15.5	A
CN4	1830	OB	No permafrost	-4.4/-3.4/-3.2/-2.6	A / B
CN5	1755	OB	3	-8.4	A
CN6	1725	OB	No permafrost	-0.3/ -0.7	C

<sup>1</sup> SG: Matrix-filled sand gravel. OB: Open-work boulders

<sup>2</sup> A: Permafrost probable. B: Permafrost possible. C: Permafrost not probable.

(HK1), direct cold heat penetration is considered to be predominant factor for permafrost development. The extremely low values recorded at CS1 and CN5 are thought to reflect the concentration of cold air beneath the block slope, which in turn is considered to be the predominant factor for permafrost development.

Permafrost was not detected by DC resistivity sounding at site CN6, where BTS values ranged from  $-0.7$  to  $-0.3$  °C, which lie outside the range of values pointing to the presence of permafrost. At the site CN7, where BTS ranges from  $-1.1$  to  $-0.0$  °C, it is difficult to determine whether the second layer indicates seasonal frost or permafrost, because the estimated thickness of frozen layer is only 2 m.

Disagreement was found at the site CN4. Permafrost has not been detected by DC resistivity sounding, in spite of low BTS values ranging from  $-4.4$  to  $-2.6$  °C, which correspond to permafrost probable and possible categories.

Thermal processes revealed by BTS monitoring provide additional information for examination of BTS criteria. The areas with extremely low BTS occur where winter cold heat can penetrate despite snow accumulation. This means that BTS can be used for identifying the sites with low ground surface temperature during winter. In addition to the one-dimensional thermal equilibrium, lateral heat conduction and subsurface cold air concentration between boulders should be considered. In both situations, permafrost was identified by DC resistivity sounding (HK1, CS3 and CN5). Also moderately low BTS values were obtained where daily temperature fluctuations have not been observed due to thick snow cover (CN3). These sites have been under the condition of the one-dimensional thermal equilibrium as shown in Haeberli and Patzelt (1982). Permafrost were identified beneath CN3 where BTS in equilibrium was  $-3$  °C. It is obvious that no permafrost underlie beneath the sites HK6, HK18 and HK29, because subzero temperature has not occurred on the ground surfaces.

It should be concluded, from what has been said above, that the empirical diagnostic BTS value of Haeberli (1973) appears to be useful in the investigation of permafrost. The BTS criteria in the Daisetsu Mountains can be used on the sites with three thermal processes beneath snow cover; one dimensional thermal equilibrium, direct cold heat penetration and cold air concentration.

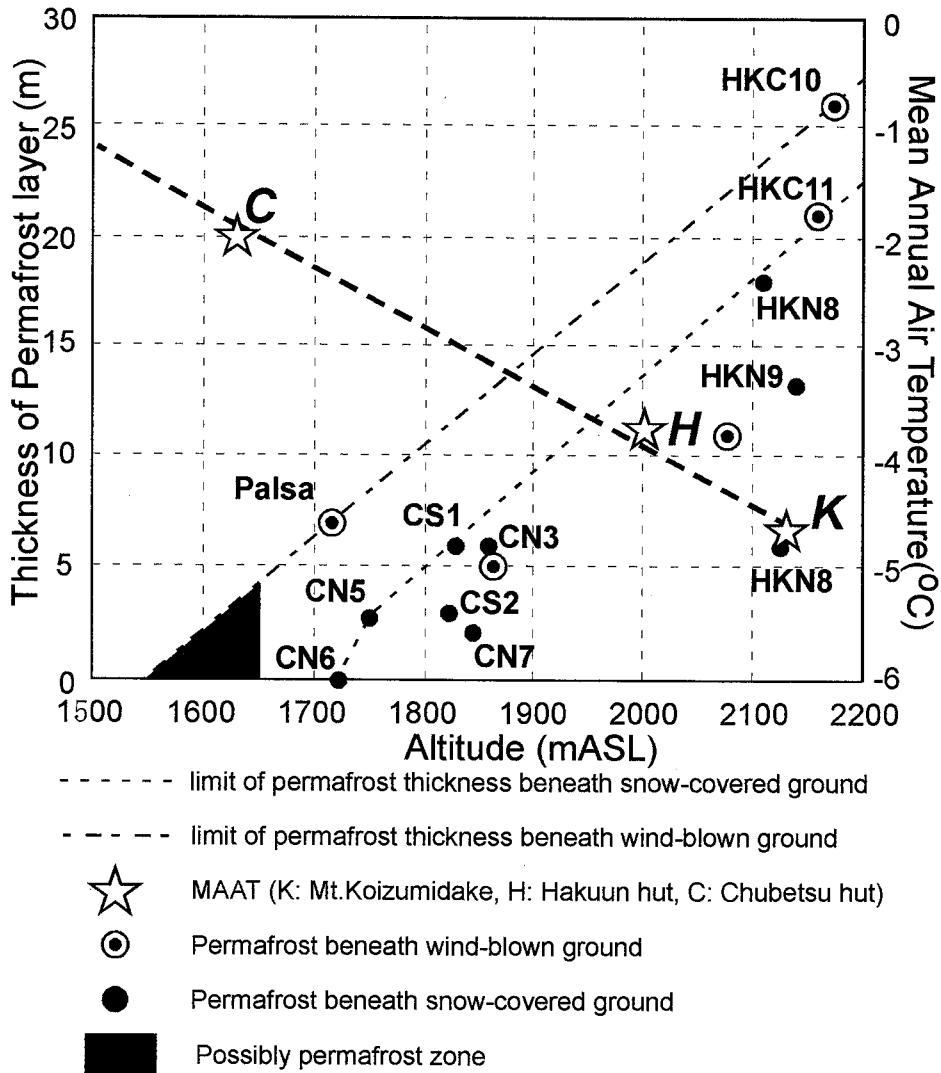
#### 4-6. Altitudinal variations of permafrost in the Daisetsu Mountains

Fig. 4.7 shows the relation between permafrost thickness and elevations and includes data obtained in the previous studies (Fukuda and Kinoshita, 1974; Fukuda and Sone, 1992; Sone, 1990; 2000). This figure also shows the MAAT trend with elevations. The thickness of permafrost layers increase with increasing elevations and decreasing MAAT. The thickest permafrost at different altitudes is found beneath wind-blown ground (HKN10, HKN11 and palsa). In these sites, the frost penetration during winter is deep. Areas affected by such conditions are most likely to develop permafrost under the present climatic conditions. Previous studies on permafrost occurrence have focused on the wind-blown ground, using annual air temperatures (Fukuda and Sone, 1992; Sone, 1990; Sone and Takahashi, 1988; Sone, *et al.*, 1988). Extrapolating the thickness of permafrost under the wind-blown ground, the lower limit of mountain permafrost is estimated to be 1550 m ASL, on the basis of MAAT at nearly  $-1.0$  °C, which corresponds to that on the southern limit of circumpolar permafrost (Brown, 1967).

The occurrences of permafrost beneath the snow-covered ground in the Daisetsu Mountains have been identified for the first time in this study. In general, the thicknesses of permafrost layers are less than those of wind-blown grounds. By extrapolating the thickness of permafrost, the lower altitudinal limit of mountain permafrost is estimated to lie between approximately 1650 and 1750 m ASL.

Compiling the lower limit estimated by both wind-blown and snow-covered grounds, the lower altitudinal limit of the permafrost should be 1650 m ASL in the Daisetsu Mountains, because the wind-blown ground is restricted only above 1650 m ASL (Sone, 1990). At this altitude, MAAT is approximately between  $-2$  and  $-3$  °C. These MAATs correspond to those in the lower limit of mountain permafrost in the world (Fujii, 1980).

BTS and DC resistivities indicate that below 1900 m elevation permafrost was only identified on the debris slope below steep cliffs (CS1, CN3). Extraordinary thick permafrost is known to occur in the palsa (Takahashi and Sone, 1988). This is probably due to the fact that peaty materials produces a considerable difference in thermal conductivities between frozen and unfrozen state and is favorable for permafrost development (Brown and Péwé, 1973). This situation is similar to that of the sporadic permafrost in circumpolar region. At CN3 site locating below the steep bedrock cliff, snow remains until late spring or mid-summer. This means that the total amount of



**Fig. 4.7** Altitudinal variations in MAAT and the thickness of permafrost layer (See fig. 4.1 for locations).

direct solar radiation is considerably less than that of the adjacent snow free area during summer. According to Funk and Hoelzle (1992), mountain permafrost is assumed to exist at low altitudes in places where direct solar radiation is reduced. This is in agreement with our study. Site CS1 is located in a depression below the talus slope where cold lateral air concentration between boulders may play an important role in developing and preserving this permafrost. The same explanation can be applied to permafrost at site CN5 that is located on the coarse boulders in the transverse furrows. Although low BTS has been observed, apparent DC resistivity values did not show obvious increases with depth. This disagreement is probably due to the limitation of DC resistivity sounding technique, which assumes that subsurface layers are horizontal. In this site, extremely small permafrost probably exists.

DC resistivity sounding and BTS measurements indicate that permafrost exists beneath snow-covered ground on the north-facing slope at elevations above 2100 m (*i.e.*, HKN8, HKN9, and HKN12). These sites have a thickness of permafrost between 6 m and 18 m, which are less than those of wind-blown ground. At these sites, the duration of frost penetration is shorter than that of wind-blown ground. The difference of permafrost thickness between three sites on the north-facing slope of Mt. Hakuundake is most probably due to the snow remaining condition, which controls the total amount of solar radiation reaching the ground surface during summer. As mentioned before, the snow disappears by mid-spring at site HKN8, whereas it remains until early summer at sites HKN9 and HKN12. This seems to cause the different thickness of permafrost layers between snow-covered and wind-blown ground.

The thickness of permafrost considerably varies above 2100 m ASL. As described above, these differences mainly depend on the factors such as snow cover status and slope orientation.

## **Chapter 5 Spatial Variations of Permafrost Distribution**

### **5-1. Introduction**

Evidence of the occurrence of permafrost in the Daisetsu Mountains is limited. In the Mt. Hakuundake region the occurrence of permafrost and its associated structures has only been studied at two sites beneath the wind-blown bare grounds (Fukuda and Kinoshita 1974, Sone *et al.*, 1988, Fukuda and Sone 1992). At the eastern side of Mt. Koizumidake, Fukuda and Kinoshita (1974) found permafrost beneath wind-blown ground through seismic reflection, DC resistivity sounding and drilling investigations. Year-round geothermal observations through a borehole (3.3 m in depth) and DC resistivity values on wind-blown ground at Hokkaidaira (2075 m ASL.) also indicated the existence of permafrost at the depth between 1.4 m and 8.5 m (Fukuda and Sone, 1992). A heat conductive model incorporating latent heat effect has been used to predict the temporal changes in thickness of active layer at the Hokkaidaira plateau (Nakayama *et al.*, 1993). Although these studies showed one-dimensional permafrost structure such as depth of permafrost bottom and active layer, spatial distribution of the permafrost has not yet been illustrated.

This chapter focuses on the *micro-scale* spatial distribution of mountain permafrost in the Daisetsu Mountains. The micro-scale is defined here as a spatial resolution less than 25 m (Hoelzle, *et al.* 2001). Intensive and detail field surveys were required in order to satisfy such a resolution. DC resistivity imaging technique together with shallow ground temperature (SGT) measurements was applied at some sites encompassing a range of surface materials, topographic characteristics and slope aspects (fig.5.1, table 5.1).

### **5-2. Local factors controlling the presence and structure of permafrost**

#### **5-2-1. Snow cover and plant distribution**

Snow has very complex influences on the ground thermal regimes in mountain areas. In general, snow is a poor heat conductor, so that short-term variations in air temperature and radiation rarely reach the snow-covered ground, where the snow cover is thick enough. A thick early winter snow cover prevents cooling of the ground. In contrast,

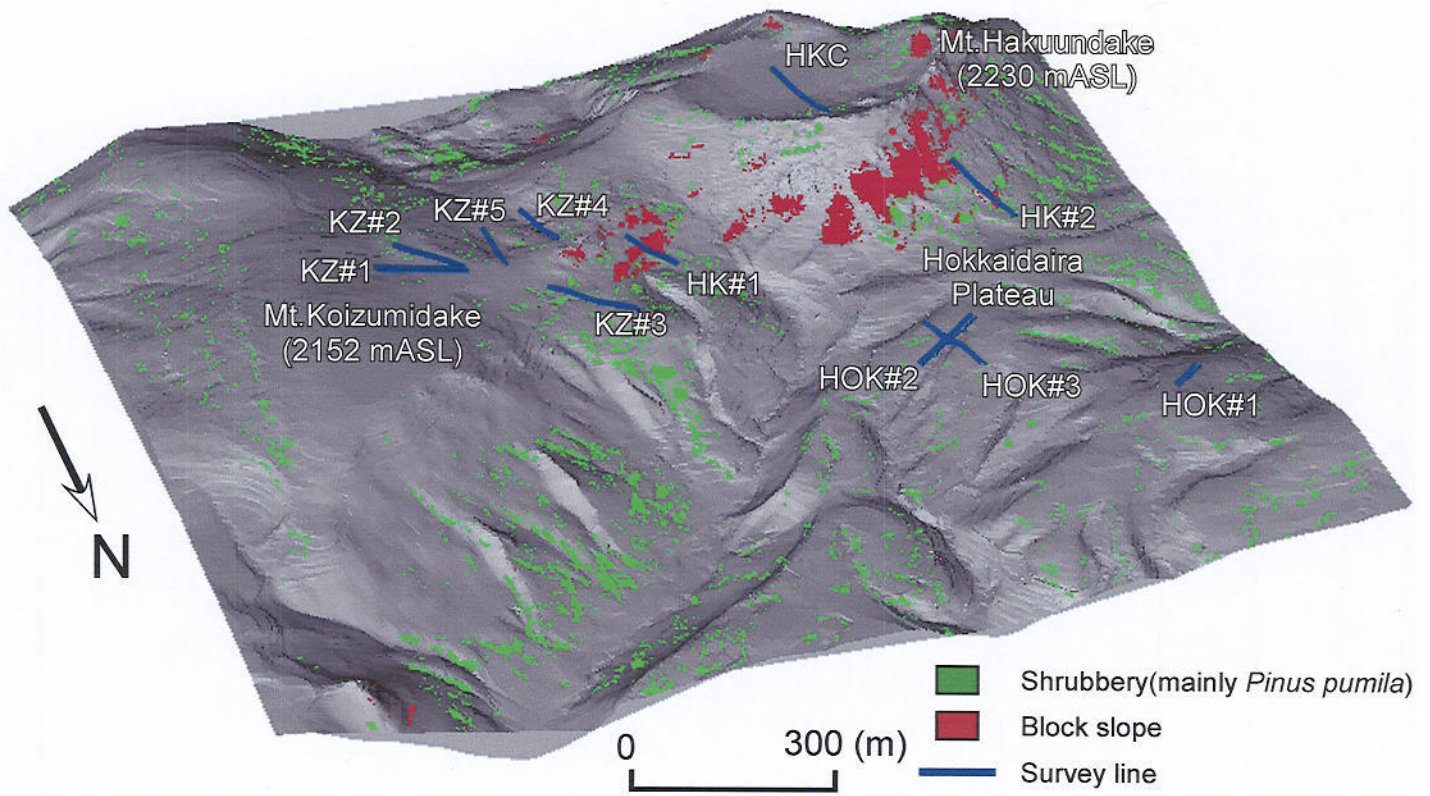


**Fig. 5.1** Digital Elevation Model of Mt. Hakuundake and its surroundings. **HOK#1, HOK#2 and HOK#3:** Survey lines on the Hokkaidaira plateau. **KZ#1, KZ#2, KZ#3, KZ#4 and KZ#5:** Survey lines on Mt. Koizumidake area. **HK#1 and HK#2:** Survey lines on the block slope on the northern slope of Mt. Hakuundake. **HKC:** Survey line on the Mt. Hakuundake volcanic crater floor. Green colored zones indicate the patch of shrubbery (mainly *Pinus pumila*), Red colored zones indicate the areas of block slopes.

**Table 5.1** Slope aspect and surface materials at each survey line. See fig.5.1 for the location of each survey line.

Line	Aspect	Surface Materials	Survey Methods			
			Plant Identification	DC resistivity imaging	Shallow ground temp.	MAST
HOK#1	SW	Fine, Sand-gravel	○	○	○	
HOK#2	NE	Fine, Sand-gravel	○	○	○	
HOK#3	NE	Fine, Sand-gravel	○	○	○	
HK#1	NW	Coarse, blocky boulders		○		○
HK#2	NW	Fine, sand-gravel, Coarse blocky boulders		○		
HKC	S	Fine, sand-gravel, peaty		○	○	
KZ#1	SE	Fine, sand-gravel	○	○	○	
KZ#2	SE	Fine, sand-gravel	○	○	○	
KZ#3	NW	Fine, peat, sand-gravel	○		○	
KZ#4	S	Fine, sand-gravel	○	○	○	
KZ#5	S	Fine, sand gravel	○	○	○	

permafrost easily develops beneath the snow-free ground, if the mean annual air temperature is below 0 °C.

Snow distribution is primarily determined by local relief and surface roughness. In the Daisetsu Mountains, snow accumulates mainly on wind leeward hollows, while only thin snow can cover convex flat summit areas and windward ground during winter. Some snow patches are formed and remain until summer on wind leeward hollows. The snow cover status of an area during both summer and winter is reflected by the local vegetation distribution as shown in fig. 5.2. *Alpine wind-blown dwarf scrub* is distributed on the windward bare ground where less snow accumulates even in winter. *Alpine snow-hostile scrub* tends to be distributed on the fringe of windward bare ground. In early winter, snow is firstly trapped by this scrub and then starts to accumulate, while snow disappears from this scrub in early spring. *Alpine snow-bed communities* and *alpine snow meadow* are distributed on the areas below the snow cover during winter. Snow remains until early summer on these areas. *Alpine snow-bed communities* are distributed on the areas where snow remains until summer or early autumn. Due to the lower amount of solar radiation received due to insulation effect of snow, less plants are distributed here. The plant species included in each community are described by Ito and Sato (1981) as listed in table 5.2.

### **5-2-2. Potential solar radiations**

Potential solar radiation is thought to be an important factor determining the presence of permafrost in European mountains. Some distribution models are based primary on the distribution of the amount of potential solar radiation (Hoelzle, 1992; Keller1992; Funk and Hoelzle, 1992; Hoelzle and Haeberli; 1995, Hoelzle, 1996).

### **5-2-3. Surface and subsurface materials**

The influence of surface materials on the distribution of permafrost is primarily a reflection of grain size (i.e. coarse or fine), which determines the thermal characteristics. In the context of significance in permafrost distribution, surface materials can be divided into two groups, depending on thermal characteristics: coarse and fine materials. As discussed in chapter 4, subsurface airflow can occur beneath the coarse blocky

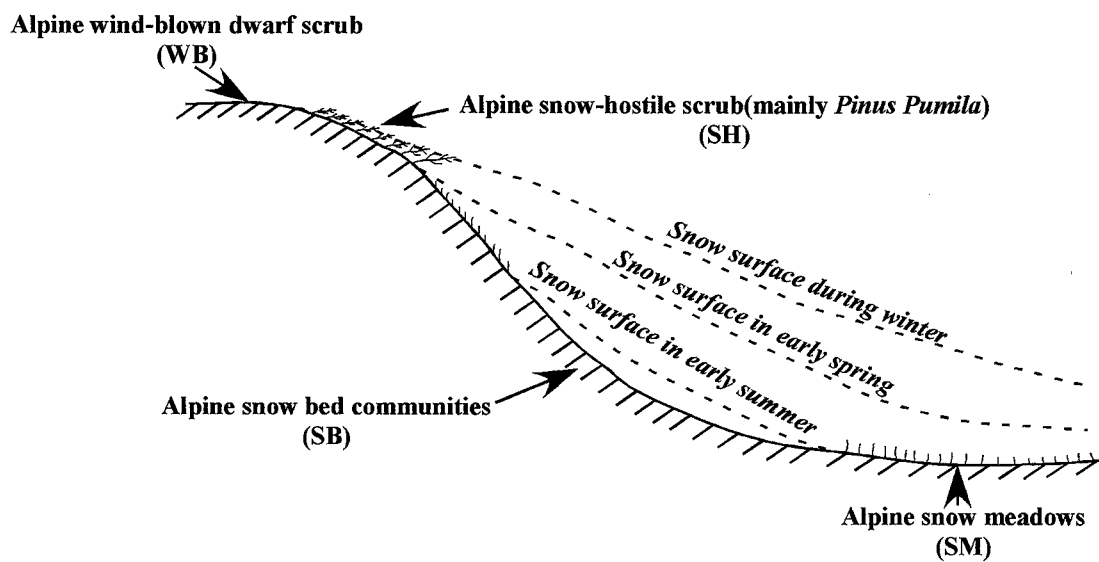


**Fig. 5.2** Schematic diagram showing relation between snow cover status and plant communities

**Table 5.2** Plant communities and plant species distributed above timberline in the Daisetsu Mountains  
(after Ito and Sato, 1981).

<i>Alpine wind-blown dwarf scrub</i>	WB	<i>Alpine snow-hostile scrub</i>	SH	<i>Alpine snow-bed communities</i>	SB-A
<i>Loiseleurina procumbens</i>	ミネズオウ	<i>S.betulifolia</i> v.aemiliana	エゾノマルバシモツケ	<i>Arnica unalaschcensis</i>	エゾウサギギク
<i>S.yanagisawae</i>	ウスユキトウヒレン	<i>V.uliginosum</i>	クロマメノキ	<i>Veronica stelleri</i> v.longistyla	エゾヒメクワガタ
<i>Diapensia lapponica</i> v. obovata	イワウメ	<i>Hierochloe alpina</i>	ミヤマコウボウ	<i>Ligularia hodgsonii</i>	ミヤマアキノキリンソウ
<i>A.arctica</i> v.villosa	シロサマニヨモギ	<i>Arctous alpinus</i> v.japonicus	ウラシマツツジ	<i>Juncus beringensis</i>	ミヤママイ
<i>P.miyabei</i>	メアカンキンバイ	<i>Rhododendron aureum</i>	キバナシャクナゲ	<i>Cirsium kamtschaticum</i> ssp.pectinellum v.alpium	ミヤマサワアザミ
<i>Bryanthus gmelinii</i>	チシマツガザクラ	<i>Empetrum migrum</i> v.japonicum	ガンコウラン	<i>Pedicularis chamissonis</i> v.japonica	ヨツバシオガマ
<i>Oxytropis japonica</i> v.sericea	エゾオヤマノエンドウ	<i>Pinus pumila</i>	ハイマツ	<i>Gentiana nipponica</i>	ミヤマリンドウ
<i>S.pauciflora</i>	エゾマメヤナギ	<i>Coptis trifolia</i>	ミツバオウレン	<i>S.reinii</i>	ミネヤナギ
<i>S.laciniata</i>	クモマユキノシタ	<i>S.miyabei</i>	エゾノシロバナノシモツケ	<i>D.caespitosa</i> v.festucaefolia	ヒロハノコメススキ
<i>A.trifurcata</i>	エゾハハコヨモギ	<i>Pubus pedatus</i>	コガネイチゴ	<i>P.multivittatum</i>	ハクサンボウフウ
<i>Arctericia nana</i>	コメバツガザクラ	<i>T.ajanensis</i>	シラネニンジン	<i>Sieversia pentapetala</i>	チングルマ
<i>C.stenantha</i> v.taisetsuensis	タイセツイワスゲ	<i>V.vitis-idaea</i>	コケモモ	<i>Sanguisorba canadensis</i> ssp.latifolia	タカネトウチソウ
<i>Penstemon frutescens</i>	イワブクロ	<i>Cassiope lycopodioides</i>	イワヒゲ	<i>L.oligantha</i>	タカネスズメノヒエ
<i>Polygonum ajanense</i>	ヒメイワタデ	<i>Potentilla matsumurae</i>	ミヤマキンバイ	<i>Harrimanella stelleriana</i>	ジムカデ
<i>C.sesquiflora</i>	ミヤマノガリアス	<i>C.flavocuspis</i>	ミヤマクロスゲ	<i>Deschampsia flexuosa</i>	コメススキ
<i>Dicentra peregrina</i>	コマクサ			<i>Carex pyrenoica</i>	キンスゲ
<i>Arenaria arctica</i> v.arctica	エゾタカネツメクサ	<i>Alpine snow meadows</i>	SM	<i>Anemone narcissiflora</i> v.sachalinensis	エゾノハクサンイチゲ
<i>Patrinia sibirica</i>	チシマキンレイカ	<i>Anemone narcissiflora</i> v.sachalinensis	エゾノハクサンイチゲ	<i>Phyllodoce caerulea</i>	エゾツガザクラ
<i>Campanula lasiocarpa</i>	イワギキョウ	<i>Parnassia palustris</i> v.tenuis	コウメバチソウ	<i>Campanula lasiocarpa</i>	イワギキョウ
<i>Luzula arcuata</i> ssp.unalascensis	クモマスズメノヒエ	<i>L.oligantha</i>	タカネスズメノヒエ	<i>Phyllodoce aleutica</i>	アオノツガザクラ
<i>S.betulifolia</i> v.aemiliana	エゾノマルバシモツケ	<i>Phyllodoce aleutica</i>	アオノツガザクラ	<i>C.chamissonis</i>	チシマギキョウ
<i>V.uliginosum</i>	クロマメノキ	<i>Arnica unalaschcensis</i>	エゾウサギギク	<i>P.cuneifolia</i>	エゾコザクラ
<i>Hierochloe alpina</i>	ミヤマコウボウ	<i>Veronica stelleri</i> v.longistyla	エゾヒメクワガタ	<i>Cassiope lycopodioides</i>	イワヒゲ
<i>Arctous alpinus</i> v.japonicus	ウラシマツツジ	<i>Ligularia hodgsonii</i>	ミヤマアキノキリンソウ	<i>Potentilla matsumurae</i>	ミヤマキンバイ
<i>Rhododendron aureum</i>	キバナシャクナゲ	<i>Juncus beringensis</i>	ミヤママイ	<i>C.flavocuspis</i>	ミヤマクロスゲ
		<i>Cirsium kamtschaticum</i> ssp.pectinellum v.alpium	ミヤマサワアザミ	<i>Salix yezoalpina</i>	エゾタカネヤナギ
				<i>Alpine snow-bed communities</i>	SB-B
				<i>C.flavocuspis</i>	ミヤマクロスゲ
				<i>P.cuneifolia</i>	エゾコザクラ
				<i>Juncus beringensis</i>	ミヤママイ
				<i>Arnica unalascensis</i>	エゾウサギギク
				<i>Lichen</i>	地衣類
				<i>Moss</i>	蘚苔類

materials with an open work structure (Harris and Pederson 1998; Bernhard *et al.*, 1998). Fine materials can be divided into sand-gravel and peat. Peaty materials show different thermal conductivities between frozen and unfrozen states (Brown and P  w  , 1973). This thermal characteristic is favorable for permafrost development.

### 5-3. Results and interpretations

#### *HOK#1*

The survey line of HOK#1 is located on the south-west facing slope of the Hokkaidaira plateau (table 5.1 and fig. 5.1). The ground surface materials are composed of matrix-filled sand-gravel. *Alpine wind-blown dwarf scrub* is distributed along the entirety of the line (fig. 5.4), suggesting that virtually nearly no snow accumulates even in winter.

Shallow ground temperatures (SGTs) were measured in early October 2000, corresponding to the end of autumn when ground temperatures reach a maximum for the year. Ground temperatures ranged from 1 to 3   C at 1m depths and from 0 to 0.2   C at 1.3 m (fig. 5.4a). These values point to the presence of permafrost below 1.5 m along the survey line. Fig. 5.4b shows the inverted DC resistivity tomogram with topography along this line. High resistivity zones between 64 k   m and 256 k   m (green to yellow colored) were found below 6 to a depth of more than 12 m. Both of SGT and DC resistivity values indicate that permafrost under this line. The active layer varies between 1 and 2 m in thickness. The thickness of the high resistivity zones is seen to increase with increasing slope inclination. This probably indicates the change in the thickness of unconsolidated sediments. The weathered unconsolidated materials on the slope areas have become thicker than those of summit areas due to gravity driven slow mass movements such as solifluction.

#### *HOK#2*

The survey line of HOK#2 is located on the north-east facing slope of the Hokkaidaira plateau (table 5.1 and fig. 5.1). Frost fissure polygons were observed on the wind blown ground surrounding this survey line (Sone and Takahashi, 1986). Between the stations at



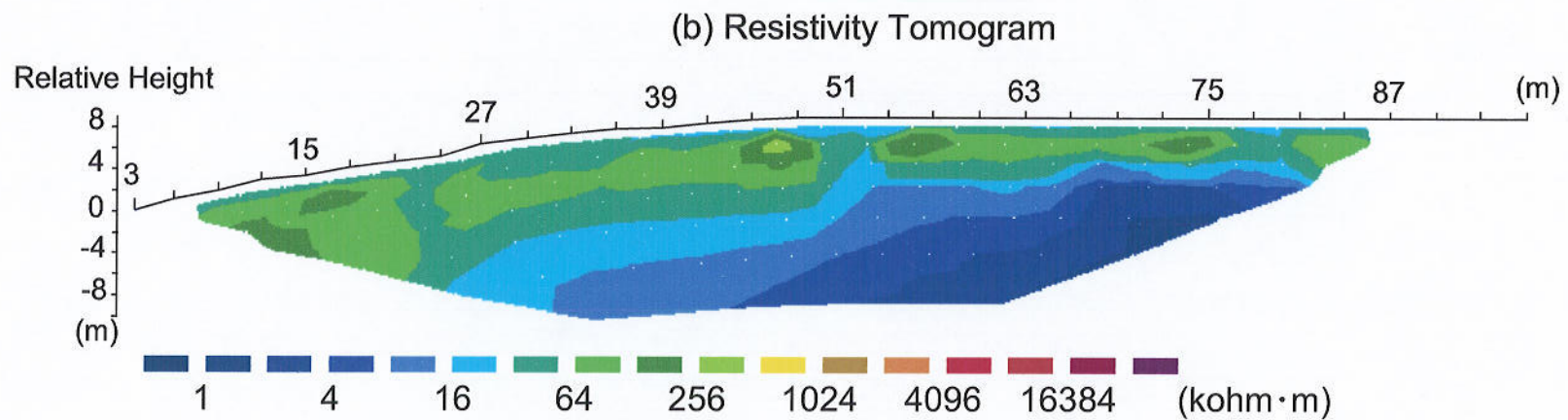
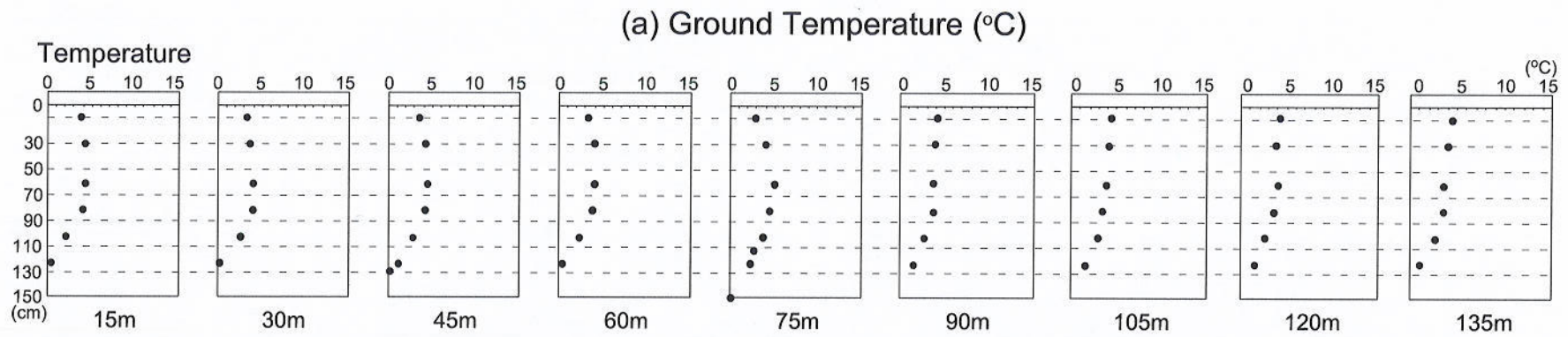


**Fig. 5.4** Distribution of (a) shallow ground temperatures and (b) DC resistivities along HOK#1 survey line

0 m and 40 m the ground surface materials are composed of sand-gravels. The distribution of *alpine wind-blown dwarf scrub* implying that there is nearly no snow accumulation along this section. Between 40 m and 150 m the ground surface contains a higher proportion of silt. The vegetation is primarily *alpine snow-bed* and *alpine snow-meadow* communities (fig. 5.5), although some species belonging to *alpine snow-hostile scrubs* are distributed around the stations 45 m and 50 m.

SGTs are seen to decrease with increasing depth between the 10 m and 40 m station, whilst equi-thermal values are recorded between 50 m and 80 m station (fig. 5.6a). Ground temperatures decrease with increasing depth within the frost crack. The inverted DC resistivity shows that the value of DC resistivities between the 10 m and 40 m stations are several hundreds  $k\Omega$  m, considerably higher than the values recorded between 50 m and 80 m (several tens  $k\Omega$  m, fig. 5.6b). This suggests that permafrost only exists between the station 10 m and 40 m, and is absent from the rest of the survey line.

### HOK#3

Survey line of HOK#3 lies perpendicular to HOK#2 (table 5.1 and fig. 5.1), with the two survey lines crossing at the 70 m station, which is located on the topographic convex point. *Alpine wind-blown dwarf scrub* is seen to dominate between the station at 0 and 70 m and between 93 and 150 m (fig. 5.7), pointing to an absence of snow cover even during winter in these areas. *Alpine snow-hostile scrub* is distributed between the stations 50 m and 70 m and between 85 m and 110 m, with *alpine snow bed* and *snow meadow communities* between the stations 60 m and 100 m. Such a vegetation assemblage points to significant snow cover between 70 m and 90 m.

SGT decrease with increasing depths between the station 10 m and 60 m and between the station 100 m and 150 m (fig. 5.8a). Frozen materials have been found at the station 20 m. SGT measurements at the 120 m station were hampered by shallow lying bedrock, which made it very difficult to penetrate the ground surface with the boring stick. Ground temperature profiles were equi-thermal between the station 70 m and 90 m. DC resistivity tomograms showed good agreement with this shallow ground temperature distribution (fig. 5.8b). High resistivity zones more than  $64 k\Omega$  m (green colored zones) were identified beneath the station between 10 m and 60 m, 85 m and 105 m and

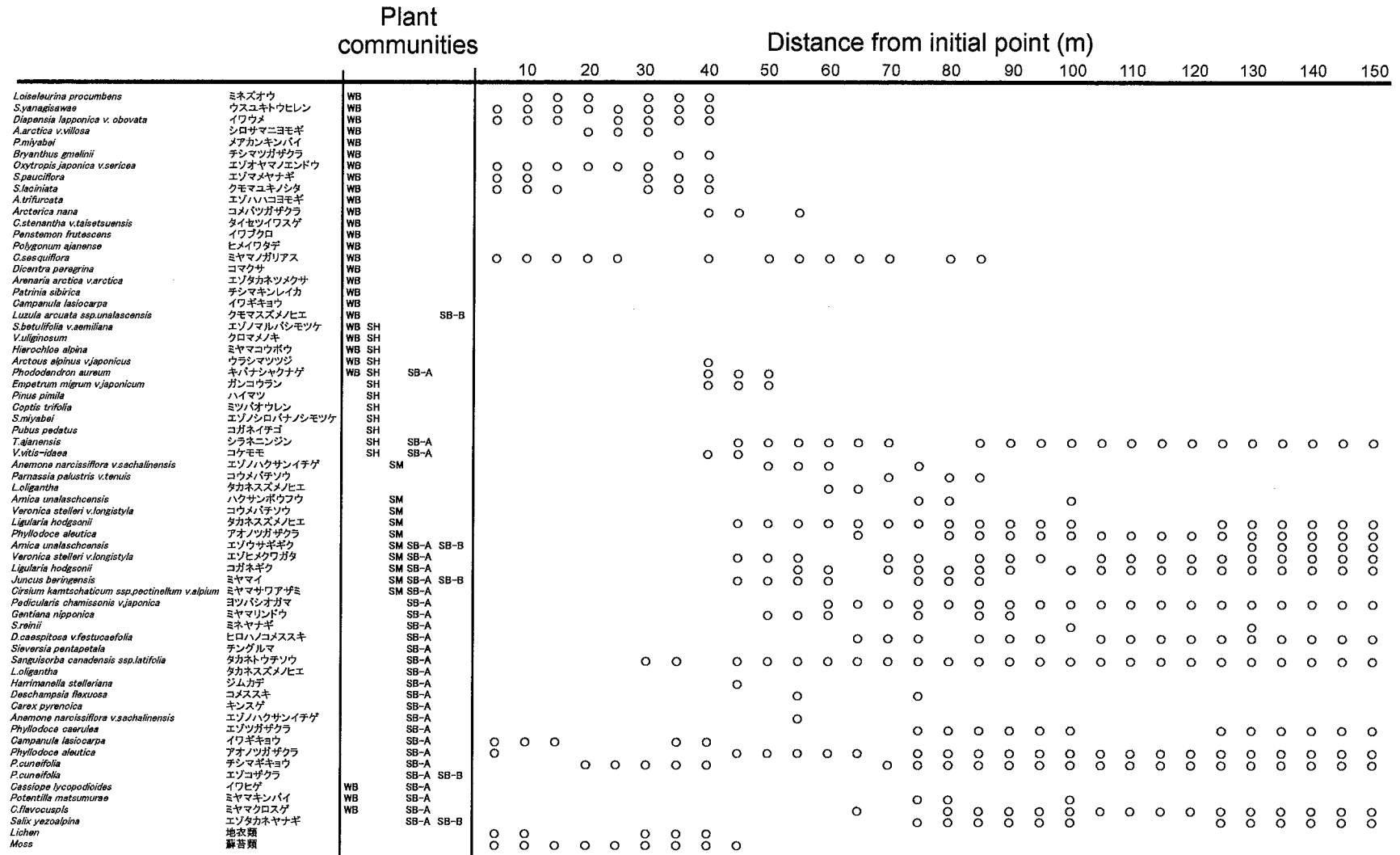
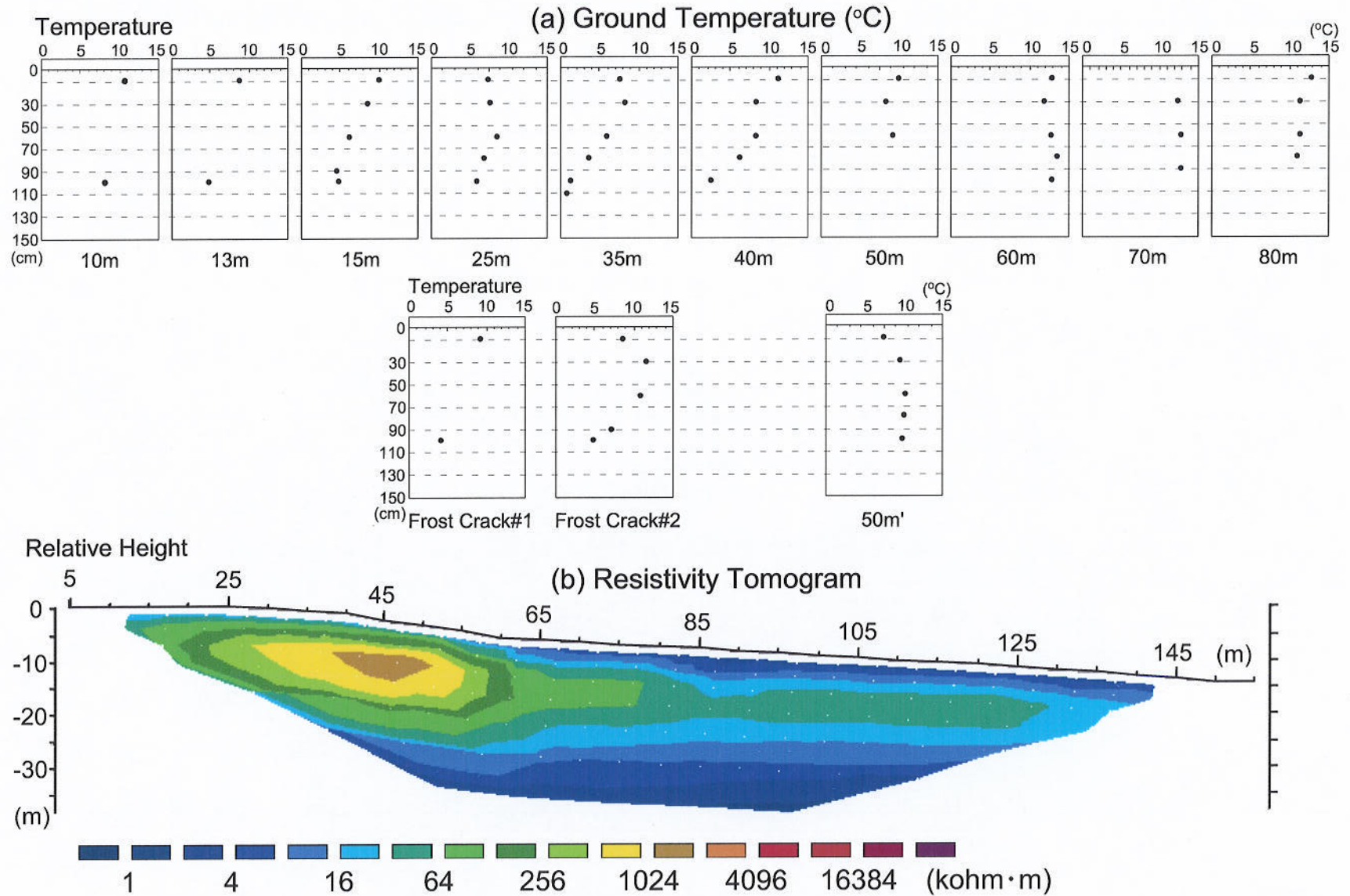


Fig. 5.5 Identification and distribution of plant species along HOK.#2 survey line (See Table 5.2 for classification of communities).



**Fig. 5.6** Distribution of shallow ground temperatures (a) and DC resistivities (b) along HOK#2 survey line. Ground temperature profiles within the frost crack are also shown.

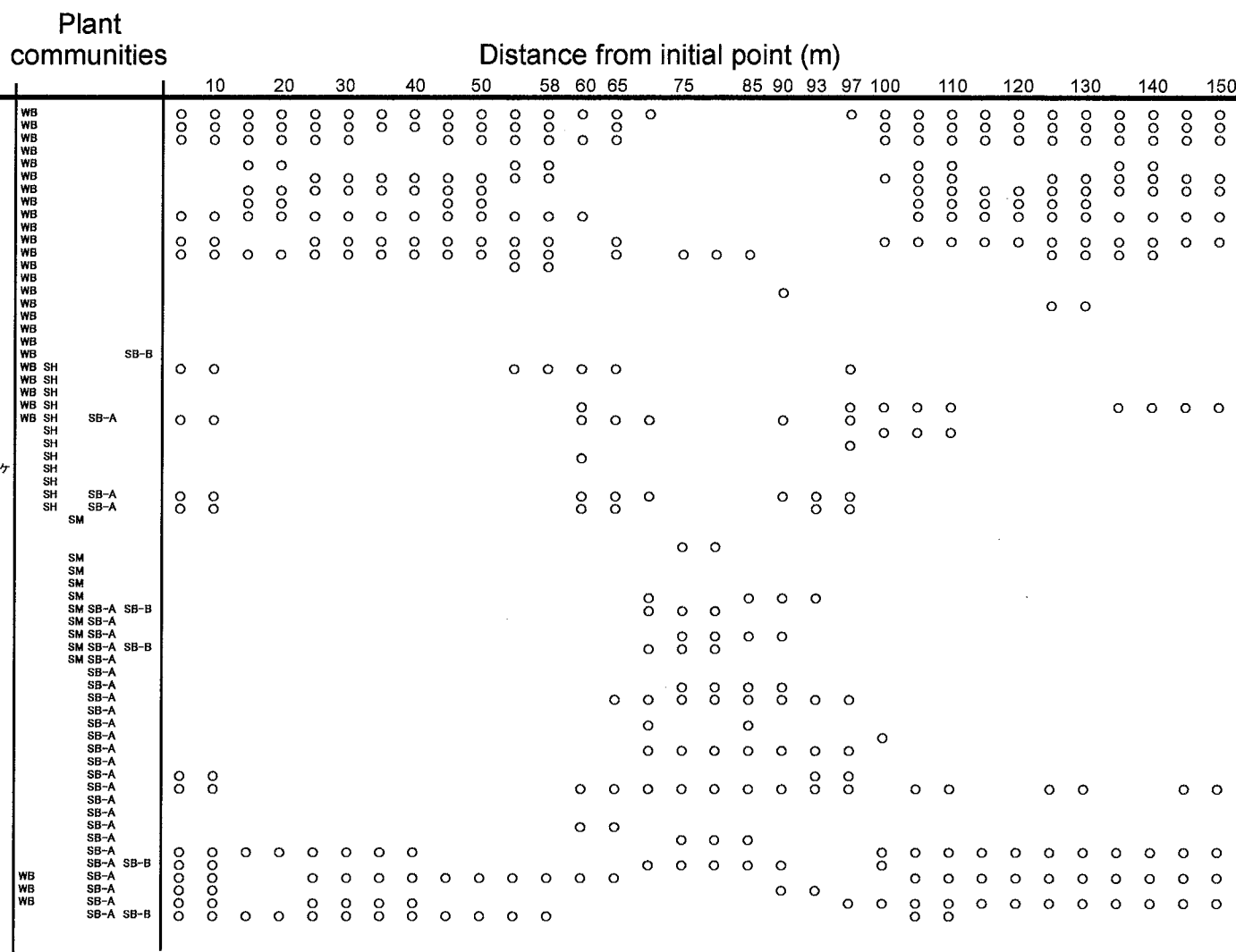


Fig. 5.7 Identification and distribution of plant species along HOK#3 survey line (See Table 5.2 for classification of communities).

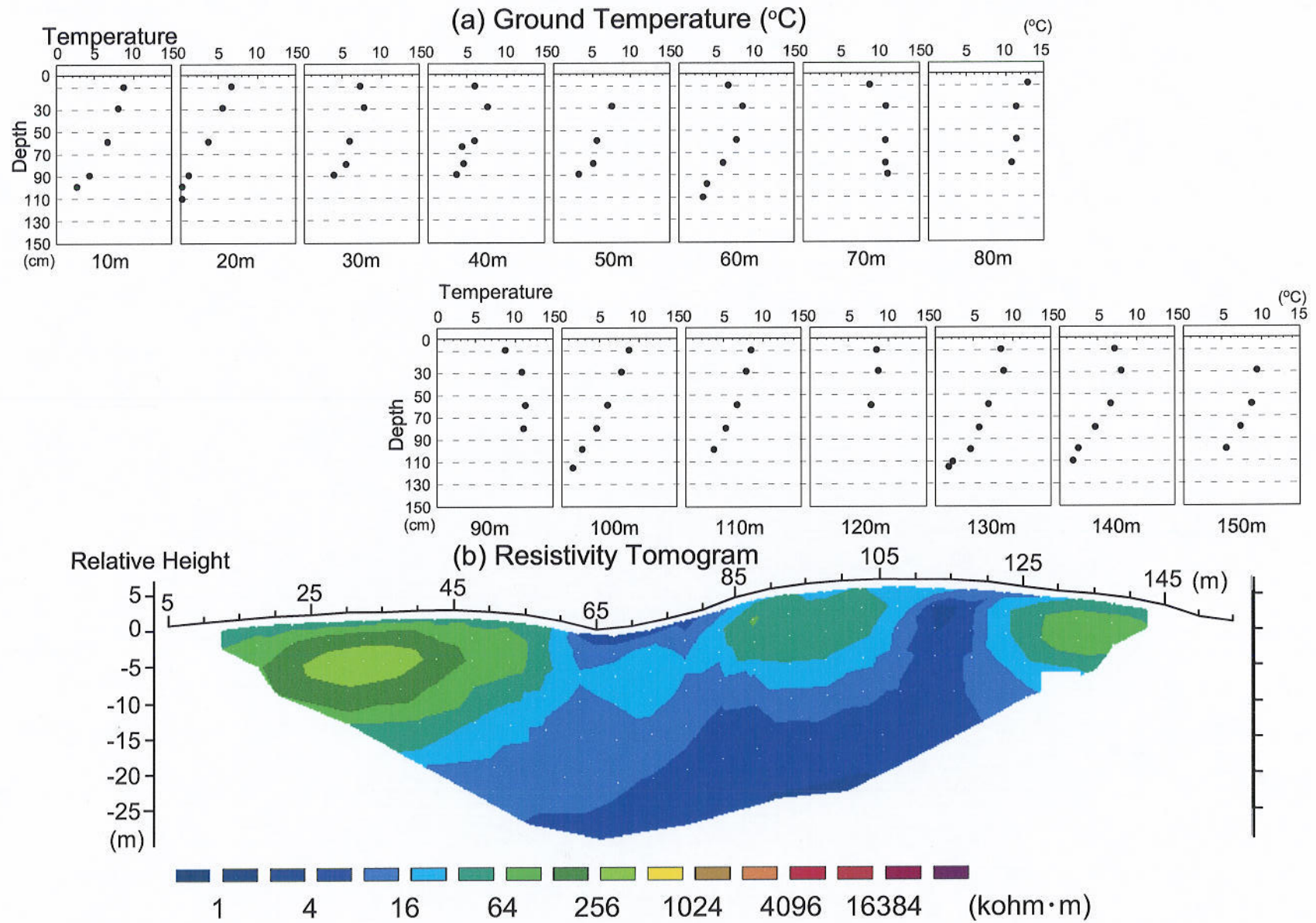


Fig. 5.8 Distribution of (a) shallow ground temperatures and (b) DC resistivities along HOK#3 survey line.

between 125 m and 140 m. These zones are thought to correspond to permafrost. Around the station at 120 m, DC resistivity values were several thousands  $\Omega$  m (blue colored zone), despite the presence of *alpine wind-blown dwarf scrub*. Since bedrock has been identified at shallower depth beneath at this station, DC resistivity may not detect frozen materials.

#### *KZ#1*

The survey line of KZ#1 is located on the south-east facing slope (table 5.1 and fig. 5.1). *Wind-blown dwarf scrub* is seen to dominate between the stations at 5 m and 65 m and between the stations at 125 m and 150 m (fig.5.9), whilst *alpine snow hostile scrub*, *alpine snow bed* and *snow meadow* are to be found between the stations at 70 m and 120 m. Such a plant distribution suggests that nearly no snow accumulates even in winter between the stations at 5 m and 80 m and between 125 m and 150 m, while much snow accumulate between the station 80 m and 120 m. The ground surface materials are composed of sand-gravel between 5 m and 80 m and between the stations 125 m and 150 m, whilst higher silt content is observed between 80 m and 125 m.

SGT is equi-thermal between the stations at 15 m and 45 m and between 75 m and 105 m, while slightly decreasing with increasing depths at the station 65 m and between the station 115 m and 145 m (fig. 5.10a). It is difficult to predict the presence of permafrost beneath this line by these ground temperature profiles alone, because ground temperature does not show significant decrease with increasing depths. Fig. 5.10b shows the inverted DC resistivity tomograms with topography. High resistivity zones more than 64 k $\Omega$  m (green colored zones) were distributed between the stations at 10 m and 25 m, around the station 65 m and between the stations 120 m and 145 m. Such zones were found in areas where the ground temperature showed a slight decrease with increasing depths. Along this line, permafrost underlies the wind-blown ground.

#### *KZ#2*

Survey line KZ#2 is located on the south-facing slope (table 5.1 and fig. 5.1). The ground surface materials are composed of matrix-filled sand-gravel. *Wind-blown dwarf scrub* is distributed along the entirety of the line (fig. 5.11), indicating a nearer total

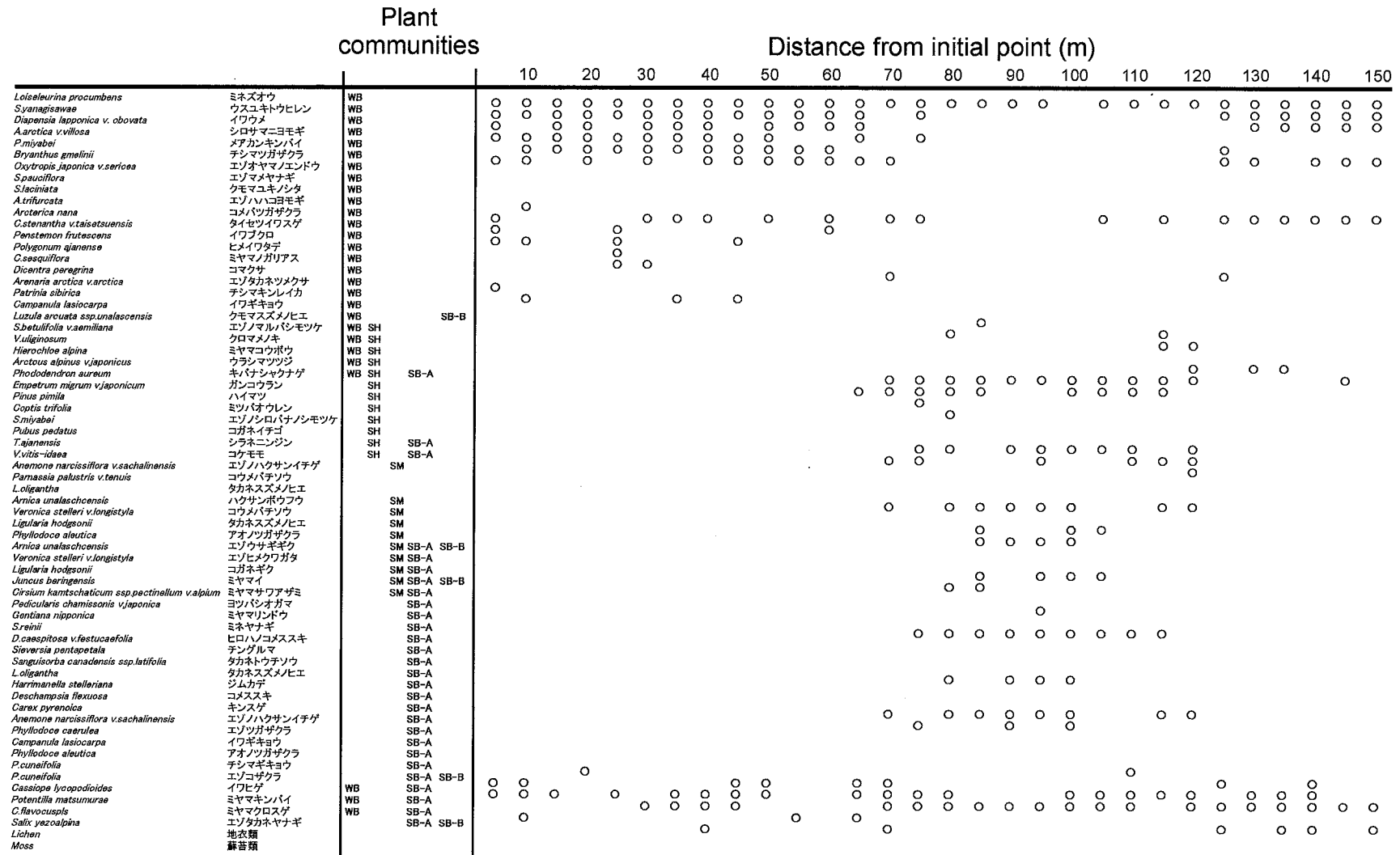
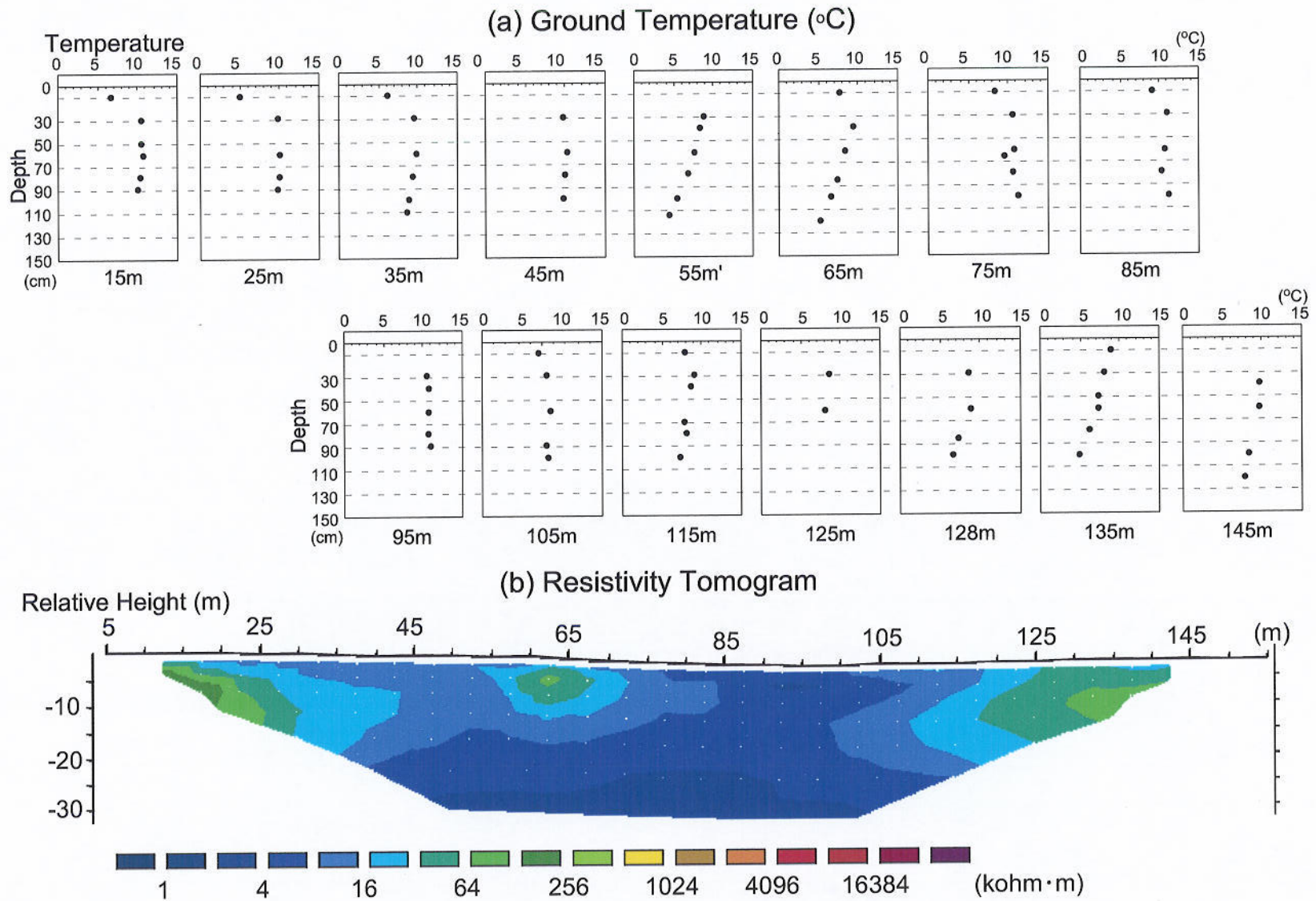


Fig. 5.9 Identification and distribution of plant species along KZ#1 survey line (See Table 5.2 for classification of communities).



**Fig. 5.10** Distribution of (a) shallow ground temperatures and (b) DC resistivities along KZ#1 survey line.

absence of snow accumulation during the winter.

SGT are almost equi-thermal between the stations 15 m and 105 m, while slightly decreasing with increasing depths between the stations 120 m and 150 m (fig. 5.12a). It is difficult to predict the presence of permafrost beneath this line by these ground temperature profiles alone, because ground temperature does not show significant decrease with increasing depths and these values at maximum depths are not as low as would be anticipated. Fig. 5.12b shows the inverted DC resistivity tomograms with topography. High resistivity zones more than  $64 \text{ k}\Omega \text{ m}$  (green colored zones) were distributed underneath throughout this line. Referring to the resistivity values, permafrost is present below the thick active layer.

### *KZ#3*

The survey line KZ#3 is located on the northwest-facing slope (table 5.1 and fig. 5.1). *Wind-blown dwarf scrub* and *alpine snow-hostile scrub* are distributed along the entirety of the line (fig. 5.13). Such a plant distribution suggests that nearly no snow accumulates even in winter on this line. The ground surface materials are composed of peat between the stations 15 m and 60 m, matrix-filled sand gravel between the stations 75 m and 141 m.

SGTs show a significant decreasing with increasing depths and are low at the maximum depth between the station 15 m and 75 m (fig. 5.14). The stations with such a low ground temperature occur in peaty materials.

### *KZ#4*

The survey line KZ#4 is located on the south-facing slope (table 5.1 and fig. 5.1). The ground surface materials are composed of matrix-filled sand gravels. The plant distribution is primarily *alpine snow-bed communities* between the stations 10 m and 50 m (fig. 5.15). There is no vegetation cover between the station 50 m and 150 m. Such plant distribution suggests that much snow accumulates during winter and remains until summer along this line.

SGTs are almost equi-thermal throughout this line and show a high temperature at the maximum depth (fig. 5.16a). A DC resistivity tomogram does not show the existence



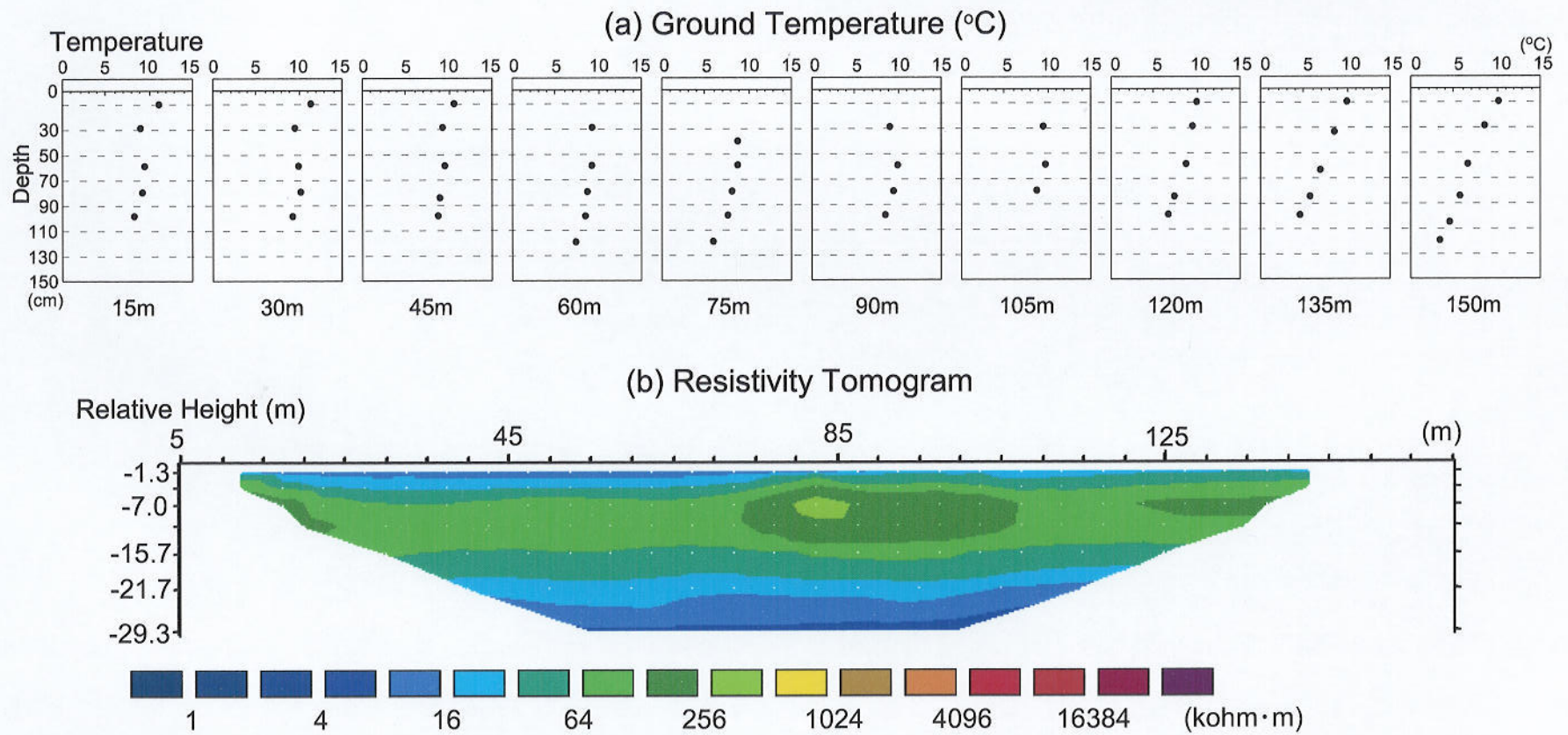


**Fig. 5.12** Distribution of (a) shallow ground temperatures and (b) DC resistivities tomogram along KZ#2 survey line.

Plant communities

Distance from initial point (m)

		10	20	30	40	50	58	60	65	70	80	90	100	110	113	120	127	130	140	141	145	150	
<i>Loiseleuria procumbens</i>	ミネズオウ	WB																					
<i>Syanagisawae</i>	ウスユキトウヒレン	WB																					
<i>Diapensia lapponica</i> v. <i>obovata</i>	イワウメ	WB	○	○	○	○	○	○	○	○	○	○	○	○	○	○	○	○	○	○	○	○	○
<i>A. arctica</i> v. <i>villosa</i>	シロサマニヨモギ	WB																					
<i>P. miyabei</i>	メアカンキンバイ	WB	○	○	○	○	○	○	○	○	○	○	○	○	○	○	○	○	○	○	○	○	○
<i>Dryanthus imelinii</i>	チシマツグザクラ	WB	○	○	○	○	○	○	○	○	○	○	○	○	○	○	○	○	○	○	○	○	○
<i>Oxytropis japonica</i> v. <i>sericea</i>	エゾオヤマノエンドウ	WB																					
<i>S. pauciflora</i>	エゾマメヤナギ	WB																					
<i>Silaciniata</i>	クモマユキノシタ	WB																					
<i>A. trifurcata</i>	エゾノハコブモギ	WB																					
<i>Arcteria nana</i>	コメバツグザクラ	WB																					
<i>Ostenantha</i> v. <i>taiseitsuensis</i>	タイセツイワスゲ	WB																					
<i>Penstemon frutescens</i>	イワブクロ	WB																					
<i>Polygonum ajanense</i>	ヒメイワタデ	WB																					
<i>C. sesquiflora</i>	ミヤマノガリアス	WB																					
<i>Dicentra peregrina</i>	コマクサ	WB																					
<i>Arenaria arctica</i> v. <i>arctica</i>	エゾタカネツメクサ	WB																					
<i>Patrinia sibirica</i>	チシマキンレイカ	WB	○	○	○	○	○	○	○	○	○	○	○	○	○	○	○	○	○	○	○	○	○
<i>Campanula lasiocarpa</i>	イワギキョウ	WB																					
<i>Luzula arcuata</i> ssp. <i>unalaschensis</i>	クモマスズメノヒエ	WB																					
<i>S. betuifolia</i> v. <i>aemiliana</i>	エゾノマルバシモツケ	WB SH	○	○	○																		
<i>V. uliginosum</i>	クロマメノキ	WB SH																					
<i>Hierochloa alpina</i>	ミヤマコウボウ	WB SH																					
<i>Arctostaphylos alpina</i>	ウラシマツツジ	WB SH																					
<i>Phododendron aureum</i>	キバナシヤクナゲ	WB SH																					
<i>Empetrum nigrum</i> v. <i>japonicum</i>	ガンゴウラン	SH																					
<i>Pinus pumila</i>	ハイマツ	SH	○	○	○	○	○	○	○	○	○	○	○	○	○	○	○	○	○	○	○	○	○
<i>Coptis trifolia</i>	ミツバオウレン	SH																					
<i>S. miyabei</i>	エゾノシロバナシモツケ	SH																					
<i>Pubis pedatus</i>	コガネイチゴ	SH																					
<i>T. ajanensis</i>	シラネニンジン	SH																					
<i>V. vitis-idaea</i>	コケモモ	SH	○	○	○	○	○	○	○	○	○	○	○	○	○	○	○	○	○	○	○	○	○
<i>Anemone narcissiflora</i> v. <i>sachalinensis</i>	エゾノハクサンイチゲ	SM																					
<i>Parnassia palustris</i> v. <i>tenuis</i>	コウメバチソウ																						
<i>L. oligantha</i>	タカネズメノヒエ	SM																					
<i>Arnica unalaschensis</i>	ハクサンボウフウ	SM																					
<i>Veronica stelleri</i> v. <i>longistylis</i>	コウメバチソウ	SM																					
<i>Ligularia hodgsonii</i>	タカネズメノヒエ	SM																					
<i>Phyllodoce aleutica</i>	アオノツグザクラ	SM																					
<i>Arnica unalaschensis</i>	エゾウサギギク	SM SB-A SB-B																					
<i>Veronica stelleri</i> v. <i>longistylis</i>	エゾヒメクワガタ	SM SB-A																					
<i>Ligularia hodgsonii</i>	コガネギク	SM SB-A																					
<i>Juncus beringensis</i>	ミヤママイ	SM SB-A SB-B																					
<i>Cirsium kamtschaticum</i> ssp. <i>pectinellum</i> v. <i>alpinum</i>	ミヤマサワアザミ	SM																					
<i>Pedicularis chamissonis</i> v. <i>japonica</i>	ヨツバシオガマ	SB-A																					
<i>Gentiana nipponica</i>	ミヤマリンドウ	SB-A																					
<i>S. reinii</i>	ミネヤナギ	SB-A																					
<i>D. caespitosa</i> v. <i>festucaeifolia</i>	ヒロハノコメスキ	SB-A																					
<i>Sieversia pentapetala</i>	チングルマ	SB-A																					
<i>Sanguisorba canadensis</i> ssp. <i>latifolia</i>	タカネトウチソウ	SB-A																					
<i>L. oligantha</i>	タカネズメノヒエ	SB-A																					
<i>Harrimanella stelleriana</i>	ジムカデ	SB-A																					
<i>Deschampsia flexuosa</i>	コメスキ	SB-A																					
<i>Carex pyrenica</i>	キンズゲ	SB-A	○	○	○																		
<i>Anemone narcissiflora</i> v. <i>sachalinensis</i>	エゾノハクサンイチゲ	SB-A																					
<i>Phyllodoce caerulea</i>	エゾツグザクラ	SB-A																					
<i>Campanula lasiocarpa</i>	イワギキョウ	SB-A																					
<i>Phyllodoce aleutica</i>	アオノツグザクラ	SB-A																					
<i>P. cuneifolia</i>	チシマギキョウ	SB-A																					
<i>P. cuneifolia</i>	エゾツグザクラ	SB-A SB-B																					
<i>Cassiope lycopodioides</i>	イワヒゲ	WB	○	○	○																		
<i>Potentilla matsumurae</i>	ミヤマキンバイ	WB																					
<i>C. flavocuspis</i>	ミヤマクロスゲ	WB	○	○	○	○	○	○	○	○	○	○	○	○	○	○	○	○	○	○	○	○	○
<i>Salix yezoalpina</i>	エゾタカネヤナギ	WB																					
Lichen	地衣類																						
Moss	蘚苔類																						

Fig. 5.13 Identification and distribution of plant species along KZ#3 survey line (See Table 5.1 for classification of communities).

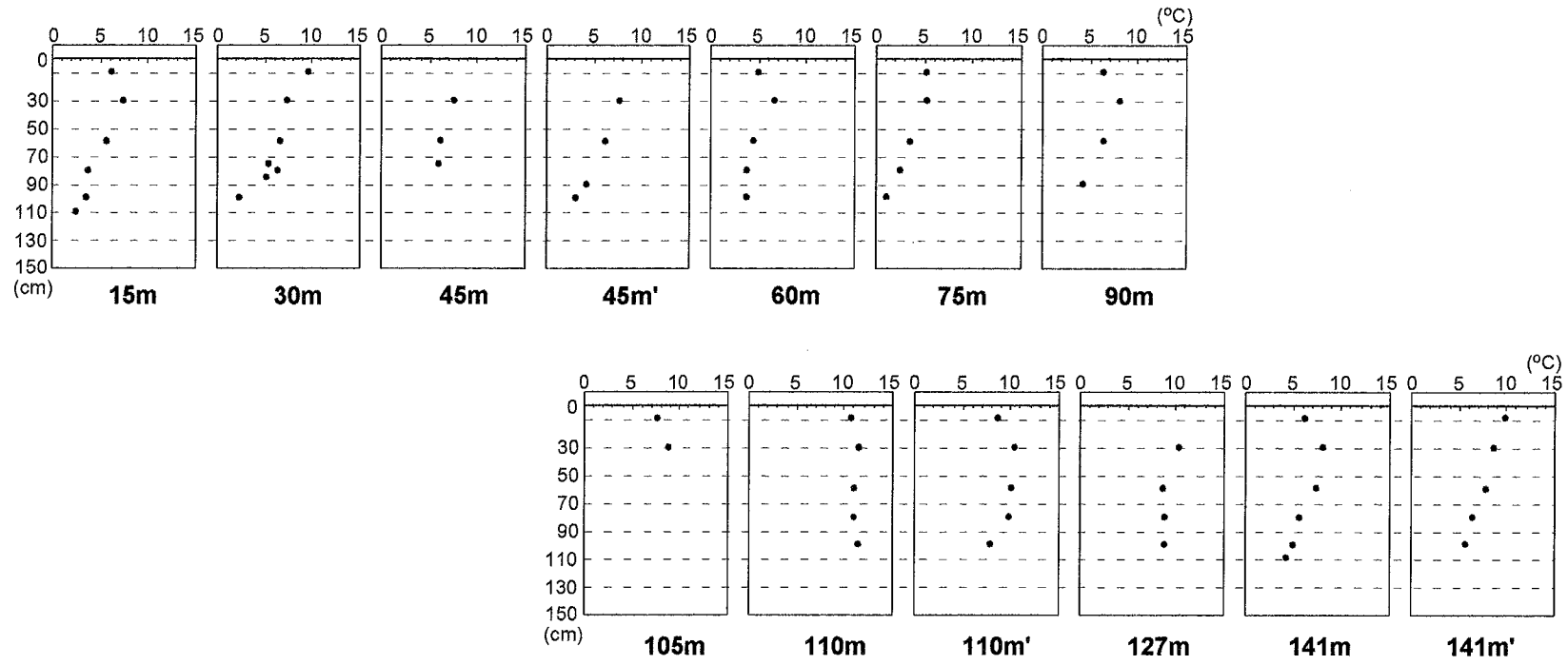


**Fig. 5.14** Distribution of shallow ground temperature along KZ#3 survey line.

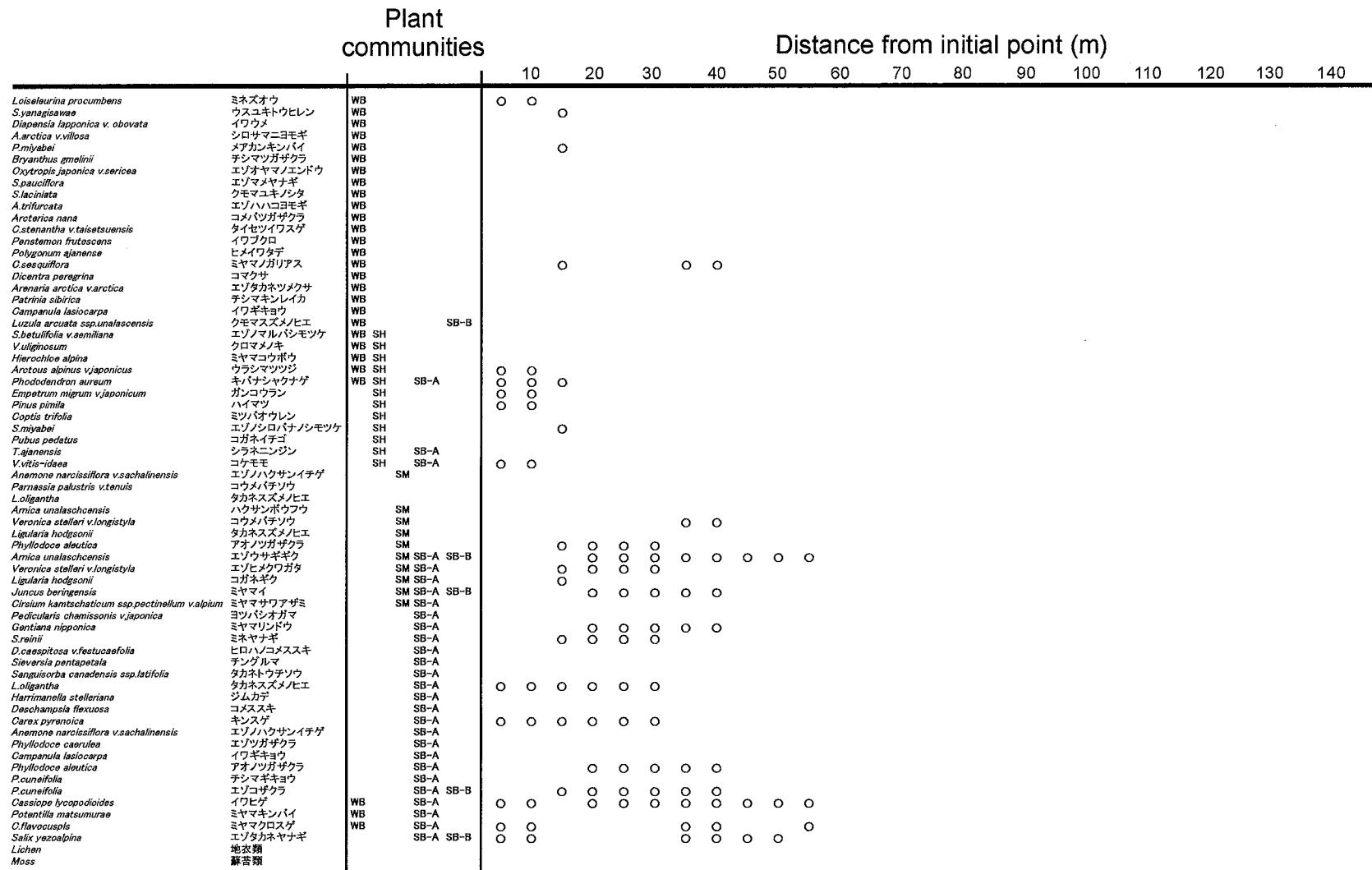
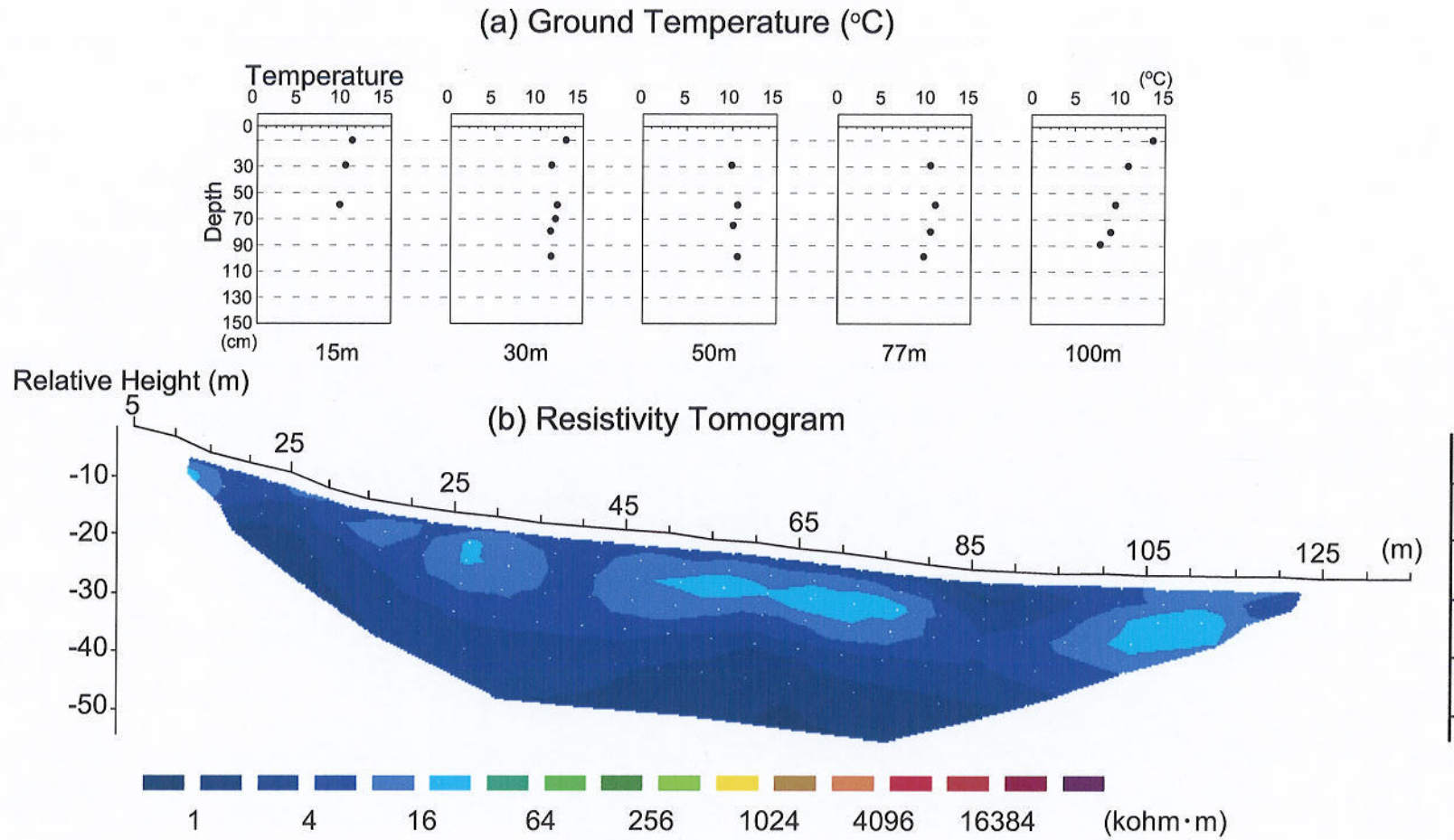


Fig. 5.15 Identification and distribution of plant species along KZ#4 survey line (See Table 5.1 for classification of communities).



**Fig. 5.16** Distribution of (a) shallow ground temperatures and (b) DC resistivities along KZ#4 survey line.

subsurface frozen materials along this line (fig. 5.16b).

#### *KZ#5*

The survey line KZ#5 is located on the south-facing slope (table 5.1 and fig. 5.1). *Alpine wind-blown dwarf scrub* is distributed between the station at 0 m and 30 m, whilst *alpine snow-bed* and *alpine snow-meadow communities* between station 45 m and 150 m (fig. 5.17). Some of species belonging to *alpine snow-hostile scrubs* are distributed around the stations 30 m and 50 m. This vegetation distribution suggests that nearly no snow accumulates between the stations at 0 m and 30 m, whilst significant snow accumulations occur on the stations between 45 m and 150 m. The ground surface materials are composed of sand-gravel between the stations at 0 m and 30 m, whilst the ground surface materials between the station 30 m and 150 m are composed of higher silt content.

SGT decreases with increasing depth between 10 m and 30 m, while showing equi-thermal values between the stations 35 m and 140 m (fig. 5.18a). At the station 20 m, frozen materials were identified below the depth of 110 cm. The inverted resistivity tomogram with topography is illustrated in fig. 5.18. High zones of resistivity of more than 64 k $\Omega$  m (green colored zone) underlies the stations between 10 and 40 m. Referring to SGTs, these zones should be permafrost.

#### *HK#1*

The survey line HK#1 is located on the northwest-facing slope (fig. 5.1). The ground surface materials are composed of coarse blocky boulders throughout this line (table 5.1). DC resistivity imaging showed the presence of high resistivity (> 64 k $\Omega$  m) zone at 2-8 m depth (fig. 5.19a). Negative MAST (= -2.0 °C, fig. 5.19b) on this block slope suggests that this high resistivity zone corresponds to coarse boulders containing perennial frozen materials.

#### *HK#2*

The survey line HK#2 is located on the northwest-facing slope (fig. 5.1). The ground

Plant communities		Distance from initial point (m)														
		10	20	30	40	50	60	70	80	90	100	110	120	130	140	150
<i>Loiseleurina procumbens</i>	ミネズオウ	WB	○	○	○	○	○	○	○	○						
<i>Syanagisawae</i>	ウスユキトウヒレン	WB	○	○	○	○	○	○	○	○						
<i>Diapensia lapponica</i> v. <i>obovata</i>	イワウメ	WB	○	○	○	○	○	○	○	○						
<i>Aarctia v. villosa</i>	シロサマニヨモギ	WB														
<i>P.miyabei</i>	メアカンキンバイ	WB														
<i>Bryanthus gmelinii</i>	チシマツグザクラ	WB	○	○	○	○	○	○								
<i>Oxytropis japonica</i> v. <i>sericea</i>	エリオヤマエンドウ	WB														
<i>Spassiflora</i>	エノメヤナギ	WB														
<i>S.laciniata</i>	クモマユキノシタ	WB														
<i>A.trifurcata</i>	エノハハコヨモギ	WB														
<i>Arcteria nana</i>	コメバツグザクラ	WB	○	○	○	○	○	○	○							
<i>C.stenantha</i> v. <i>taisetsuensis</i>	タイセツイワスゲ	WB														
<i>Penstemon frutescens</i>	イワブクロ	WB				○										
<i>Polygonum ajanense</i>	ヒメイワタデ	WB														
<i>C.sesquiflora</i>	ミヤマノガリアス	WB						○								
<i>Diantha peregrina</i>	コマクサ	WB														
<i>Arenaria arctica varctica</i>	エノタカネツメクサ	WB														
<i>Patrinia sibirica</i>	チシマキンレイカ	WB														
<i>Campanula lasiocarpa</i>	イワギキョウ	WB														
<i>Luzula arcuata</i> ssp. <i>unalascentis</i>	クモマスズメノヒエ	WB														
<i>S.betullifolia</i> v. <i>aemiliana</i>	エノノマルバシモツゲ	WB SH				○	○	○	○	○						
<i>Vuliginosum</i>	クロマメキ	WB SH														
<i>Hierochloa alpina</i>	ミヤマコウボウ	WB SH														
<i>Arctos alpinus v. japonicus</i>	ウラシマツツジ	WB SH														
<i>Phododendron aureum</i>	キバナシヤクナゲ	WB SH	○													
<i>Empetrum nigrum v. japonicum</i>	ガンコクラン	SH				○	○	○	○	○						
<i>Pinus pinnata</i>	ハイマツ	SH				○	○	○	○	○						
<i>Coptis trifolia</i>	ミツバオウレン	SH														
<i>S.miyabei</i>	エノシロバナノシモツゲ	SH														
<i>Pubis pedatus</i>	コガネイチゴ	SH														
<i>T.ajanensis</i>	シラネニンジン	SH				○	○	○	○	○						
<i>V.vitis-idaea</i>	コゲモモ	SH				○	○									
<i>Anemone narcissiflora</i> v. <i>sachalinensis</i>	エノノハクサンイチゲ	SM														
<i>Parnassia palustris</i> v. <i>tenuis</i>	コウバチソウ															
<i>L.oligantha</i>	タカネズメノヒエ															
<i>Arnica unalaschensis</i>	ハクサンボウフウ	SM														
<i>Veronica stelleri</i> v. <i>longistyla</i>	コウバチソウ	SM														
<i>Ligularia hodgsonii</i>	タカネズメノヒエ	SM														
<i>Phyllocladus aleutica</i>	アオノツグザクラ	SM														
<i>Arnica unalaschensis</i>	エノノサギギク	SM SB-A SB-B														
<i>Veronica stelleri</i> v. <i>longistyla</i>	エノヒメクワガタ	SM SB-A														
<i>Ligularia hodgsonii</i>	コガネギク	SM SB-A														
<i>Juncus beringensis</i>	ミヤマイ	SM SB-A SB-B														
<i>Cirsium kamtschaticum</i> ssp. <i>pectinellum</i> v. <i>alpinum</i>	ミヤマサワアザミ	SM SB-A														
<i>Pedicularis chamissonis</i> v. <i>japonica</i>	ヨツバシオガマ	SB-A														
<i>Gentiana nipponica</i>	ミヤマリンドウ	SB-A														
<i>S.rainii</i>	ミネヤナギ	SB-A														
<i>D.caespitosa</i> v. <i>festucaeifolia</i>	ヒロハノコムスキ	SB-A														
<i>Sieversia pentapetala</i>	チングルマ	SB-A														
<i>Sanguisorba canadensis</i> ssp. <i>latifolia</i>	タカネトウチソウ	SB-A														
<i>L.oligantha</i>	タカネズメノヒエ	SB-A														
<i>Harrimanella stelleriana</i>	ジムカデ	SB-A														
<i>Daschampsia flexuosa</i>	コムススキ	SB-A														
<i>Carex pyrenaica</i>	キンスゲ	SB-A														
<i>Anemone narcissiflora</i> v. <i>sachalinensis</i>	エノノハクサンイチゲ	SB-A														
<i>Phyllocladus caerulea</i>	エノツグザクラ	SB-A														
<i>Campanula lasiocarpa</i>	イワギキョウ	SB-A														
<i>Phyllocladus aleutica</i>	アオノツグザクラ	SB-A														
<i>P.cuneifolia</i>	チシマギキョウ	SB-A														
<i>P.cuneifolia</i>	エノコザクラ	SB-A SB-B														
<i>Cassiope lycopodioides</i>	イワヒゲ	WB	○	○	○	○	○	○	○	○						
<i>Potentilla matsumurae</i>	ミヤマキンバイ	WB	○	○	○	○	○	○	○	○						
<i>C.flavocuspis</i>	ミヤマクワガタ	WB	○	○	○	○	○	○	○	○						
<i>Salix yezoalpina</i>	エノタカネヤナギ	SB-A SB-B	○	○	○	○										
<i>Lichen</i>	地衣類															
<i>Moss</i>	蘚苔類															

Fig. 5.17 Identification and distribution of plant species along KZ#5 survey line (See Table 5.2 for classification of communities).

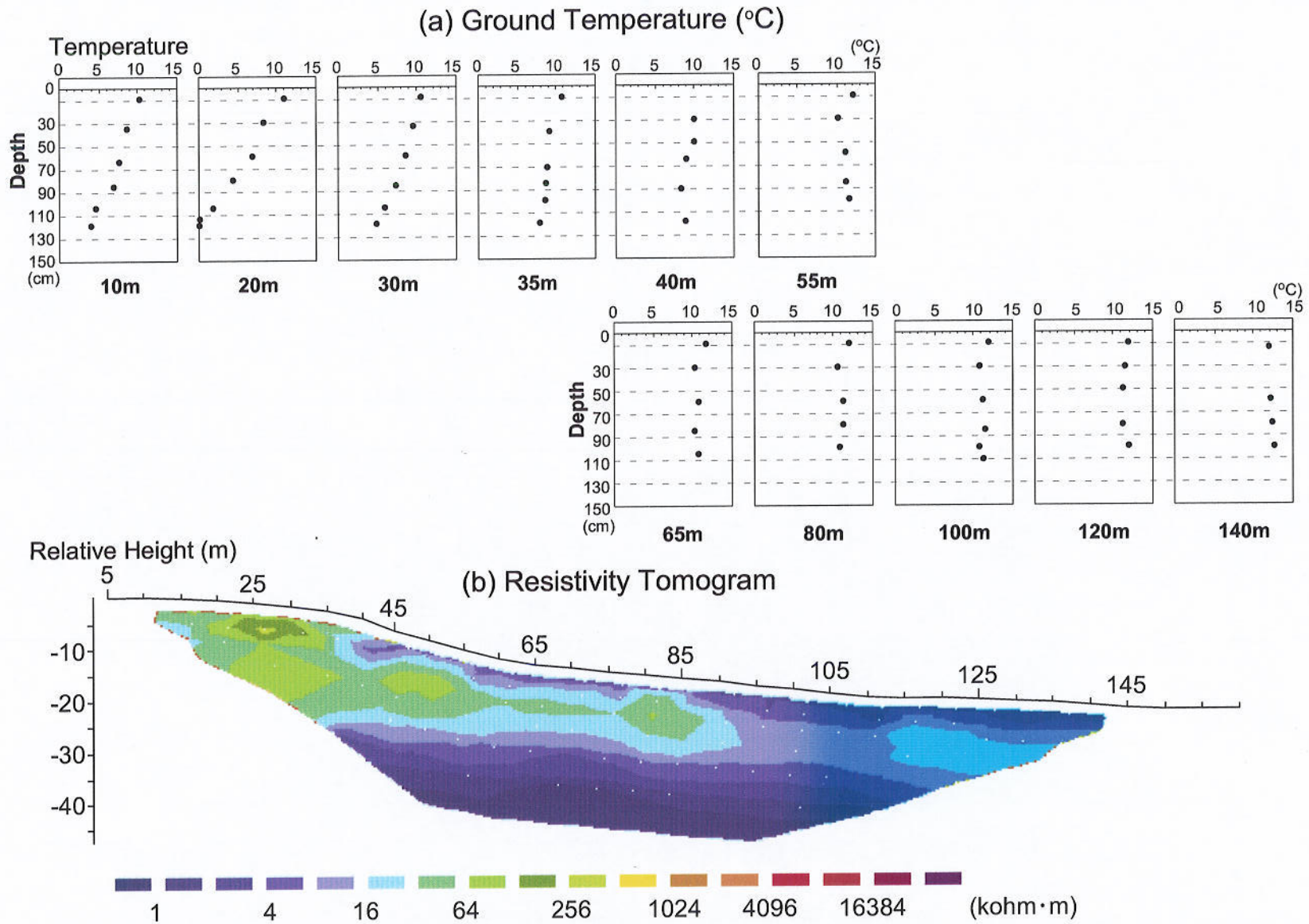


**Fig. 5.18** Distribution of (a) shallow ground temperatures and (b) DC resistivities along KZ#5 survey line.

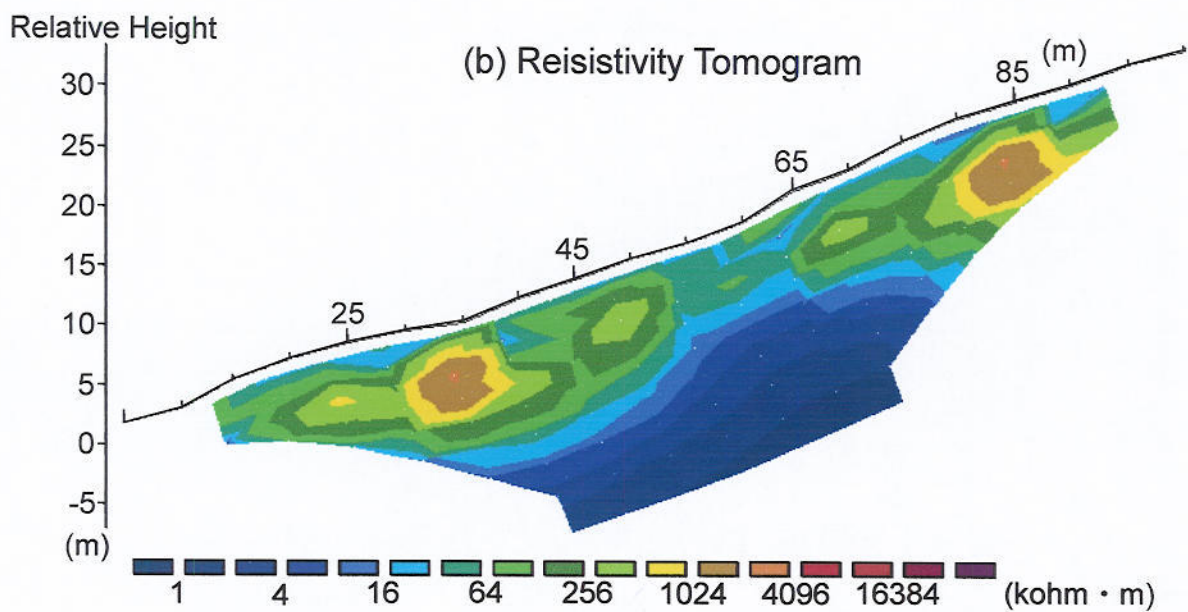
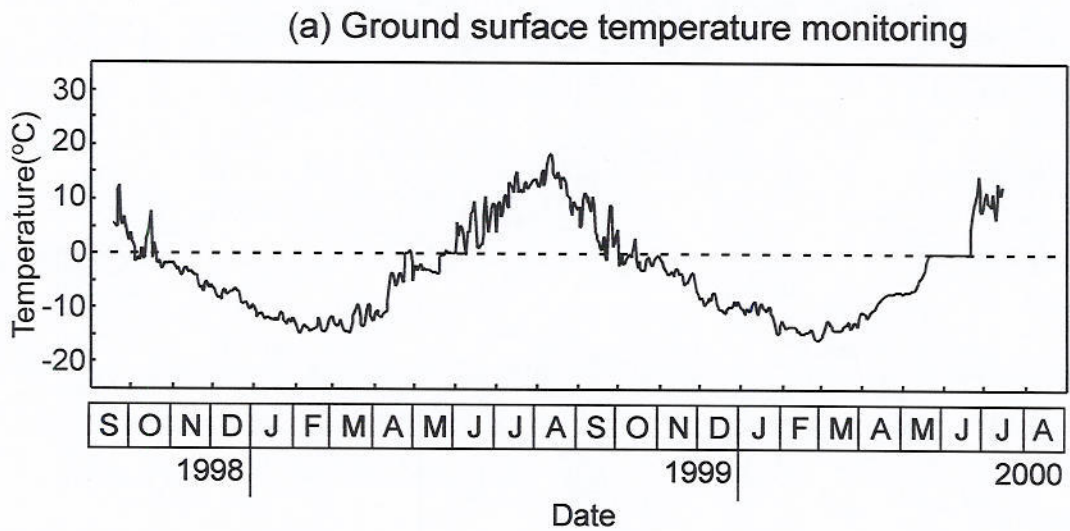


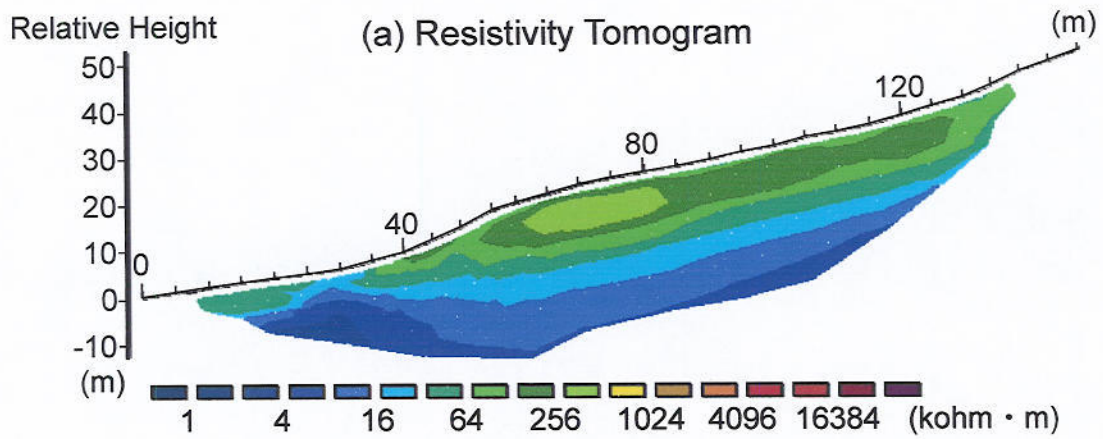
**Fig. 5.19** (a) Temporal variation of ground surface temperature and (b) DC resistivity tomogram along HK#1 survey line.

surface materials are composed of sand gravel with a significant silt component between the stations 0 m and 40 m, open-work coarse boulders between the stations 40 m and 140 m. These coarse boulders show lobate shapes, having obvious concave and convex topographic breaks. DC resistivity imaging showed the presence of high resistivity ( $> 64 \text{ k}\Omega \text{ m}$ ) zones only beneath the lobate landforms only, approximately 10 m in thickness (fig. 5.20a). Although no additional information is available along this line, this high resistivity zone probably corresponds to permafrost. This is because that the block slope exposed to atmosphere above snow cover even in winter (fig. 5.20b) and should be under same thermal condition as HK#1.

### *HKC*

The survey line HKC is located on the volcanic crater floor (fig. 5.1). A hummocky topography composed of peaty materials is observed around the line. As described previously, no snow accumulates here even in winter. The ground surface materials are composed of sand gravel between 0 m and 90 m, while the ground surface materials have a high peat and silt contents between 90 m and 165 m.

DC resistivity tomograms and SGT distribution show a good correlation. SGT is seen to decrease with increasing depth and sometimes reaches  $0 \text{ }^{\circ}\text{C}$  along the line (fig. 5.21a). A boring stick was not able to penetrate into the ground at the station 109 m due to the existence of bedrock at shallow depth. Fig. 5.21b also shows the inverted DC resistivity tomogram along this line. High resistivity zones ( $> 64 \text{ k}\Omega \text{ m}$ ) were identified below the surface with approximately 25 m in depth. Between the stations 110 m and 120 m, the DC resistivities were slightly low ( $< 64 \text{ k}\Omega \text{ m}$ ). Since bedrock was found at shallow depth (50 cm), DC resistivities would be expected to be low even if frozen material underlay this station. The DC resistivity tomogram showed that a high resistivity zone does not underlie between the stations 165 m and 185 m. Since SGT at the station 165 m is equi-thermal and was relatively high at the depth of 100 cm, it can be concluded that no frozen material exists below these stations.



(b) View of the block slope of HK#2.

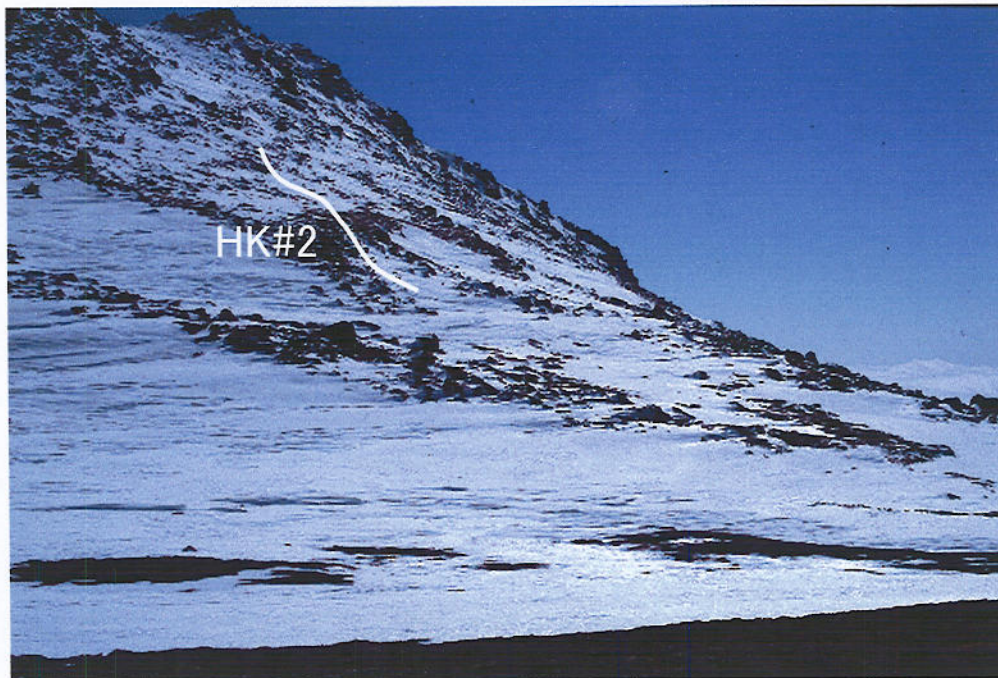


**Fig. 5.20** (a) DC resistivity tomogram along HK#2 survey line and (b) View of the HK#2 in early April.

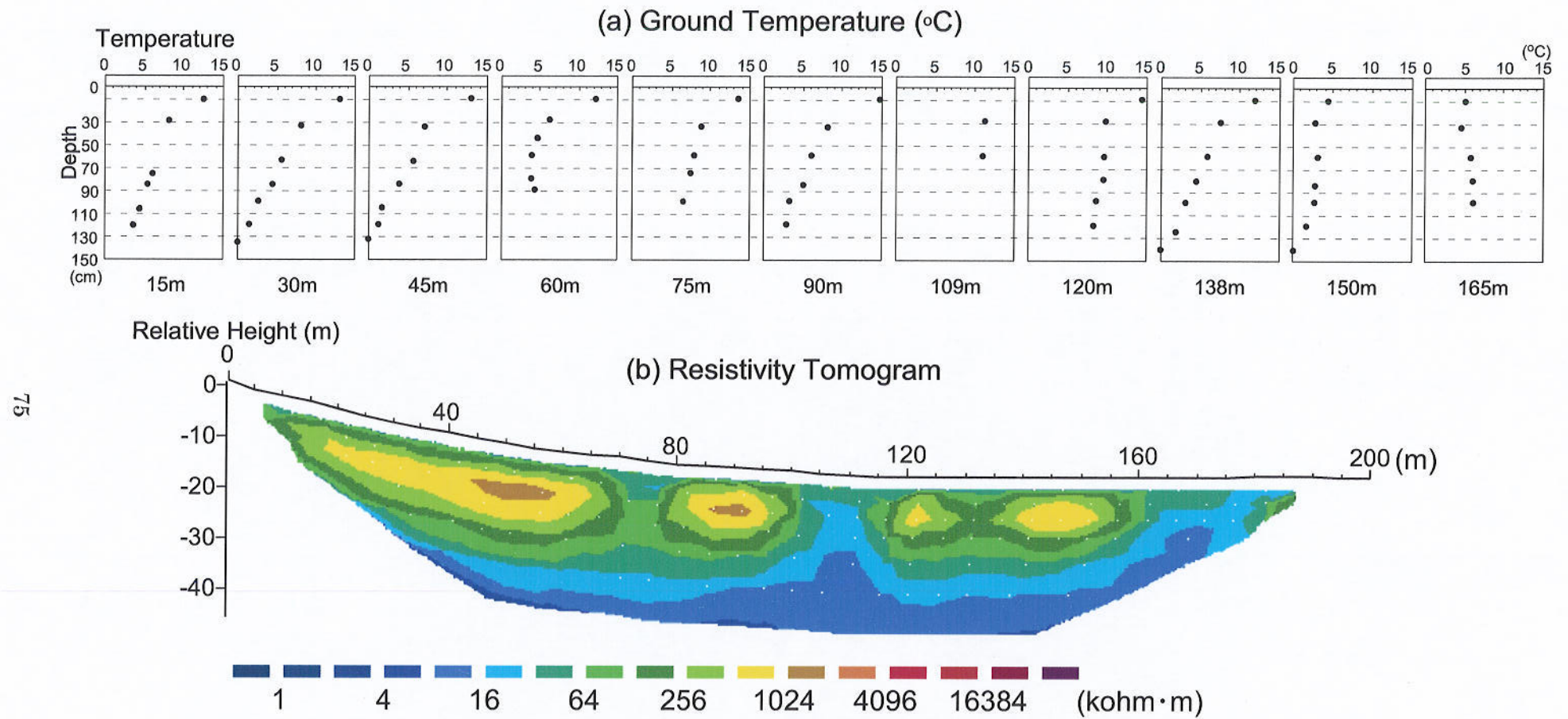


**Fig. 5.21** Distribution of (a) shallow ground temperatures and (b) DC resistivities along HKC survey line.

#### **5-4. Micro-scale permafrost distribution and the factors controlling permafrost presence**

Permafrost was found to underlie all locations in wind-blown sites where less snow accumulates even in winter (HOK#1, KZ#2, KZ#3 and HKC). Permafrost was not identified beneath the snow-covered ground (KZ#4). DC resistivity and ground temperature regimes were seen to change suddenly across the boundaries between wind-blown and snow-covered ground (HOK#2, HOK#3, KZ#1 and KZ#5). This indicates that the permafrost distribution is strongly controlled by accumulation and duration of snow cover both in winter and summer.

The accumulation of snow cover during the winter can also explain the existence of permafrost beneath the blocky surface (HK#1). Daily fluctuation in ground surface temperature occurred even in winter (fig. 5.19b). Since blocky coarse surface is accompanied by a significant surface undulation, snow tends to accumulate in the hollows between boulders, while it is rare on the top of boulders. Under such conditions, winter frost is able to penetrate into the ground, leading to the development of permafrost by the same process as that in the wind-blown ground. The difference in the thickness of permafrost between wind-blown ground (25 m in thickness at HKC) and blocky slope (several m in thickness at HK#1) can be explained by the difference in the thermal effect of snow cover. Subsurface lateral cold air flow may also contribute to development of such permafrost (Humlum, 1997; Harris and Pedersen, 1998, Bernhard *et al.*, 1998).

Lower ground temperatures were identified beneath the peaty materials (KZ#3). It is known that the ground thermal regime is influenced by organic materials, which favor the development of permafrost (Williams and Smith, 1989). The thermal conductivity of peat, which is low in unfrozen state but high in frozen, keeps ground temperatures low in summertime. This thermal characteristic of peat has been thought to play an important role in controlling the presence of permafrost at lower altitudes in the Daisetsu Mountains (Takahashi and Sone, 1988). On the other hand, although peat may contribute to the presence of permafrost, this factor is not of primary importance in the areas investigated in this study. A more important factor should be the snow cover status as stressed above.

Slope orientation influences the amount of solar radiation received by the ground

surface. The effects of differential insulation are particularly clear in mountainous regions. For example, permafrost has been identified at low altitudes in places where direct solar radiation is extremely reduced in European Alps (Funk and Hoelzle, 1992; Kneisel *et al.*, 2000). In this study, the active layer was found to be thicker on the southern slopes (KZ#1 and KZ#2) than in the northern slope (KZ#3). An explanation for this difference is the difference in the total amount of potential solar radiation received at each slope during the summer. However, it must be pointed out that low ground temperatures were recorded at HOK#1, which was located on the southwest-facing slope. Both slope aspect and inclination may affect the total amount of potential solar radiation incoming ground surface. On the basis of quantitative calculations, the effect of potential solar radiation will be discussed in the subsequent chapter.

## Chapter 6 Spatial Mountain Permafrost Modelling

### 6-1. Introduction

In the context of spatial mountain permafrost modelling, two conceptual frameworks have been suggested: physically based *process-oriented models* and regionally calibrated *empirical-statistical models* (Hoelzle *et al.*, 2001). *The process-oriented models* are based on the main energy exchange process between the atmosphere and the ground surface. This model requires an extensive set of input data on meteorological conditions such as short-wave net radiation, long-wave incoming radiation and turbulent fluxes. This is in addition to information on snow distribution and ground surface characteristics such as albedo, surface roughness, emissivity and topography (Mittaz, *et al.*, 2000a, b).

*Empirical-statistical models* are somewhat simpler, incorporating various kinds of calculated and measured climatic factors including freezing or thawing indices, potential direct solar radiation and MAAT (Nelson and Outcalt, 1987; Funk and Hoelzle, 1992; Hoelzle, 1996; Hoelzle and Haeberli, 1995; Hoelzle *et al.*, 1993). Although the complex energy exchange processes at the surface and within the active layer are not treated explicitly, these models are quite reliable if well calibrated locally or regionally. As was shown in chapter 5, a wealth of data has been presented pointing to the occurrence of permafrost in the study region. In addition to this data is also needed for the modelling to proceed on meteorological conditions such as short-wave net radiation and long-wave incoming radiation. Consequently an empirical statistics approaches has been adopted to the spatial modelling of mountain permafrost in the summit areas of the Daisetsu Mountains.

The purpose of this chapter is primary to present a spatial model of mountain permafrost in the Daisetsu Mountains with the resolution less than approximately 25 m. This resolution is comparable to that used for the field observations and measurements. Two proxies, which indicate permafrost distribution, were considered and calculated spatially; the distribution of the amount of potential solar radiation (PR) during summer and the cumulative annual freezing and thawing indices (CFTI) on the ground surface with the thermal insulation effect of snow cover. Among them, PR has been thought to be good proxy indicating the permafrost distribution in European Mountains (Funk and

Hoelzle, 1992; Hoelzle and Haerberli, 1995; Hoelzle, 1996).

## 6-2. Analytical procedure and data collection

In recent years, Geographical Information Systems (GIS) have been used more and more in the field of permafrost research (Keller 1992; Funk and Hoelzle, 1992; Haerberli *et al.*, 1993; Anisimov, 1996; Hoelzle, 1996; Li *et al.*, 1998; Etzelmüller 2001; Hoelzle *et al.*, 2001; Gruber and Hoelzle, 2001). This is because permafrost models require high-resolution spatial data such as elevation, land-type, and climatic data and GIS can manipulate these data efficiently. Since some permafrost models can be easily integrate with GIS data models, GIS methods have become the essential components of many models.

A precise topographic map of Mt. Hakuundake and its surroundings was drawn based on photogrammetrical procedure (using *Leica SD2000*, scale of 1:5000 with 2 m contour interval) and was interpolated into the quadrate 2 m unit grid cells. In addition to the elevation data, the land-covers were also mapped. The patches of shrubbery and the blocky slopes were mapped by photogrammetry. General purpose GIS software; *Arc/View ver. 3.2* with its *Avenue Scripts* was used for the data processing.

## 6-3. Modelling the distribution of potential radiation (PR)

### 6-3-1. Computational procedures

The energy of the potential direct solar radiation (PR) received by a surface element in a day under clear sky conditions is calculated by following;

$$I_p = \int_{t_r}^{t_s} I_0 \cos(\vec{N}, \vec{S}) dt \quad (6.1)$$

where  $I_p$  is PR,  $I_0$  is the incoming radiation from the sun (called here solar radiation),  $\vec{N}$  is the vector perpendicular to the surface,  $\vec{S}$  is the vector towards the sun, and  $t_r$  and  $t_s$  are times of sunrise and sunset. In order to calculate  $I_p$  for one point,  $\vec{N}$ ,  $\vec{S}$ ,  $I_0$ ,  $t_r$  and  $t_s$  have to be determined.  $\vec{N}$  is determined by derivation of slope angle and aspect of

each grid cell. The vector towards the sun  $\vec{S}$  at time  $t$  is represented by the two angles, the zenith angle  $\Theta$ , and the azimuth angle,  $a$  :

$$\cos \Theta = \cos H^* \cos \Phi^* \cos \delta + \sin \Phi^* \sin \delta \quad (6.2)$$

$$\sin a = \sin H^* \frac{\cos \delta}{\sin \Theta} \quad (6.3)$$

where  $H^*$  is the time angle,  $\Phi^*$  the latitude and  $\delta$  the solar declination. The time angle describes how far east or west the Sun is from the local meridian. It is zero when the Sun is on the meridian and decreases at a rate of  $15^\circ$  per hour. Solar declination is the angle between the direction to the Sun and the plane of the Earth's equator and is given by;

$$\delta = 23.45 \sin(360^\circ (284 + N)/365) \quad (6.4)$$

where  $N$  is the Julian day. The declination varies from  $23.45^\circ\text{S}$  to  $23.45^\circ\text{N}$ .

### 6-3-2. The algorithm

The flowchart in fig. 6.1 shows calculation of solar radiation at a site and the program written in *Avenue Scripts (Arc/View ver. 3.2)*. This program calculates the integrated inner product between vectors perpendicular to the surface and the direction to the sun, and prompts for latitude, day numbers when calculations are to begin and end, as well as the time interval to be used.

Initially topographic parameters such as vector perpendicular to the surface ( $\vec{N}$ ) are calculated for each grid cell. These parameters remain stable throughout calculation. Sunrise and sunset time were determined by substituting  $\Theta$  for  $90^\circ$  in the left side member of equation 6.2. Once the sunrise and sunset times are calculated, solar radiation is integrated from sunrise and sunset during a day. At this point, it is necessary to decide the time interval between solar irradiance calculations. This decision depends on both the accuracy required and the terrain, and should be balanced against computational expense. The program calculates the total incoming solar radiation at

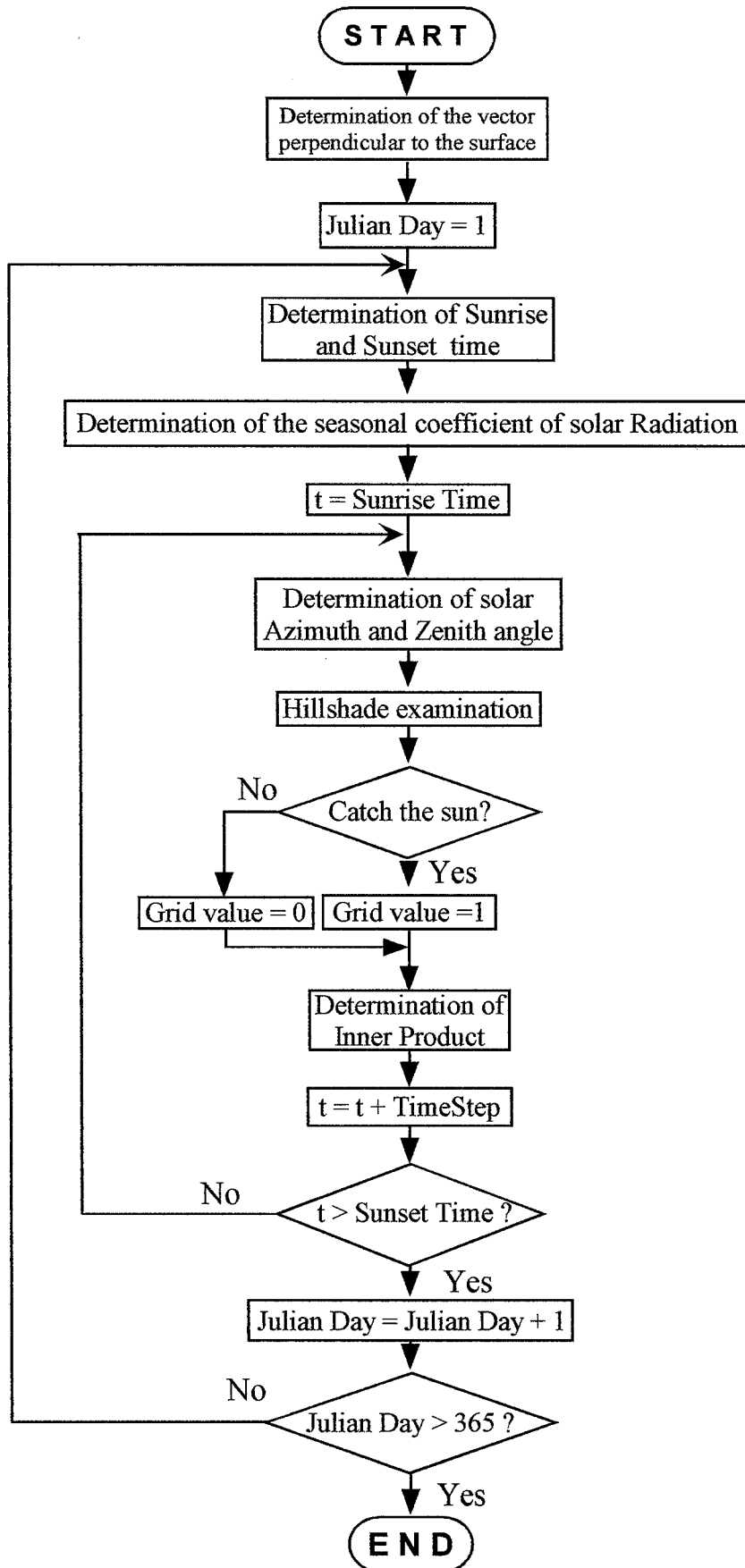


**Fig. 6.1** Flowchart for calculating potential solar radiation

every grid cell in 15 minutes increments. Solar azimuth and zenith angles at each time are determined by equations 6.2 and 6.3. Next the index for illumination  $r$  was calculated at every grid cells. The *HILLSHADE* command in *Arc/View* creates a shaded relief grid by considering the illumination angle and shadows from a grid elevation, solar azimuth and zenith angles. Shadows are assigned as value of zero and illuminated grid cells are given by a value of one.

The potential solar radiation has a dimension of  $\text{kW h m}^{-2}$ . After the completion of the calculation from 1 May to 30 October, a weighting coefficient was multiplied to the calculated cumulative inner products between vector perpendicular to the surface and the direction to the sun. This weighting coefficient was determined by the result of PR monitoring around the summit of Mt. Hakuundake (fig. 6.2). The relation between measured potential solar radiation and calculated inner vector showed good linear correlation ( $R^2 = 0.88$ , fig. 6. 2). The weighting coefficient is determined to be 0.1422 (fig. 6.2), and then will be multiplied to all grid cells.

#### **6-4. Modelling the distribution of CFTI**

In order to calculate the distribution of CFTI, distribution of snow cover has been simulated geometrically (Ishikawa and Sawagaki, 2001). Assuming annual temporal changes of snow cover distribution and of thermal effect, CFTI have been simulated spatially.

##### **6-4-1. Modelling the distribution of snow cover**

###### **6-4-1-1. Model**

In order to simulate the snow cover distribution, a snow-transport model has been developed numerically (Liston and Sturm, 1998; Greece *et al.*, 1999). This model requires meteorological data such as air temperature, relative humidity, wind speed, wind direction and precipitation. However, it is difficult to apply this numerical model to the areas without these meteorological records. Instead, a simple geometrical model will be suggested here.

First, areas favorable for snow accumulation on the basis of the flow separation theory were considered (Chang, 1976). In mountain areas above the timberline, the

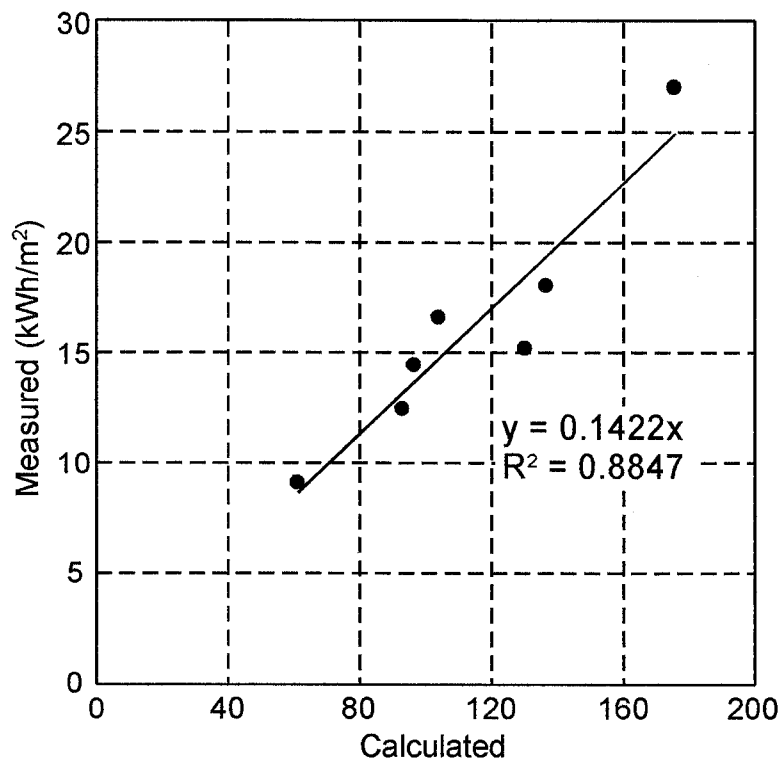


**Fig. 6.2** Correlation between calculated non-dimensional potential solar radiation and measured potential solar radiation (After Takahashi, 1995). Axis of abscissa is dimensionless

distribution of snow cover is controlled not only by the amount of precipitation but also by the wind speed, direction and the local relief. If the wind speed has an infinitely large velocity and thus the shear stress is large enough, the surface wind streamlines deflect owing to local relief (fig. 6. 3). The wind streamlines, separate away from the surface at concave topographic breaks (figs. 6.3a and 3b), upstream of obstacles (fig. 6.3c), and even along a curved surface (fig. 6.3d). Snow transportation occurs upstream of separation and downstream of reattachment, while snow accumulates at the separation, where wind velocities are reduced below the wind shear velocity (Liston and Sturm, 1998). Numerical solution of wind streamline separation over complex topography is difficult, because a number of boundary conditions are required, such as wind direction, velocity and topographic parameters at all sites and all times.

In the present model based on Digital Elevation Model (DEM), each elevation cell is increased iteratively, assuming that the terrain is covered with snow. According to the observations in the Daisetsu Mountains by Yamada *et al.* (1978), significant amounts of snow accumulate over the concave terrain, while less accumulates over the convex windward ground (fig. 6.4). This snow cover distribution is due to the strong wind that blows in this mountain. The snow is ablated on the convex terrain, while accumulated on the concave due to snow transport by wind drift.

In order to simulate this snow accumulation spatially, the  $3 \times 3$  neighborhood statistics were applied as shown in fig. 6.5. The elevation value of the center grid cell (grid cell No. 5 in fig. 6.5) is substituted by the maximum value within nine neighborhood grid cells, multiplying the empirically based weighting factor  $r$ , ranging from 0 to 1. This data processing is shown by:

$$Elev.(CenterGrid) = r * Maxof GridCell(All3x3Grids). \quad (6.5)$$

The advantages of this data processing are that the elevation values of a grid on concave terrain, increases more rapidly than that on a convex and that the elevation values of a grid on convex terrain unchanged.

Due to snow transport by wind drift, the thickness of snow cover varies with the slope aspect and inclination. For simulating this variation  $r$  was determined by multiplying the coefficient depending on the slope aspect ( $CA$ ) and inclination ( $CI$ ) as follows:

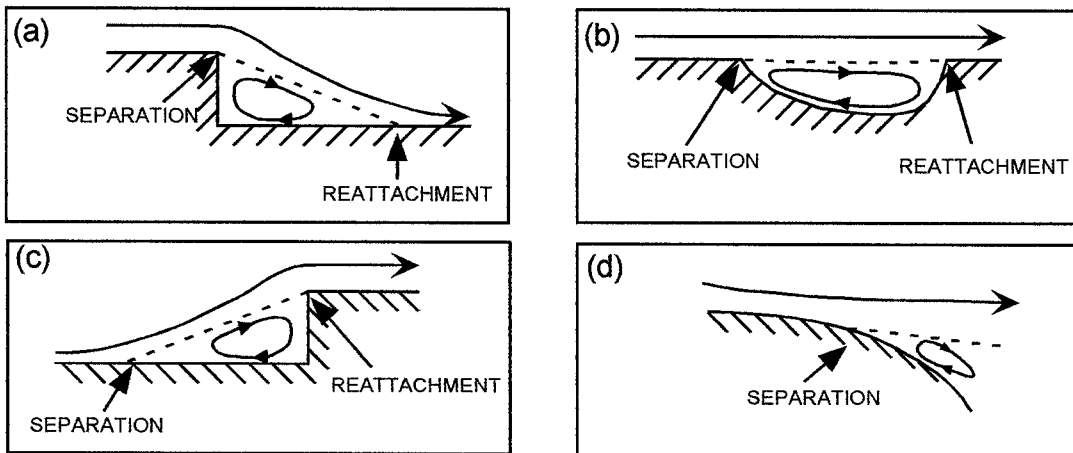


**Fig. 6.3** Separation of flow (after Chang, 1976)

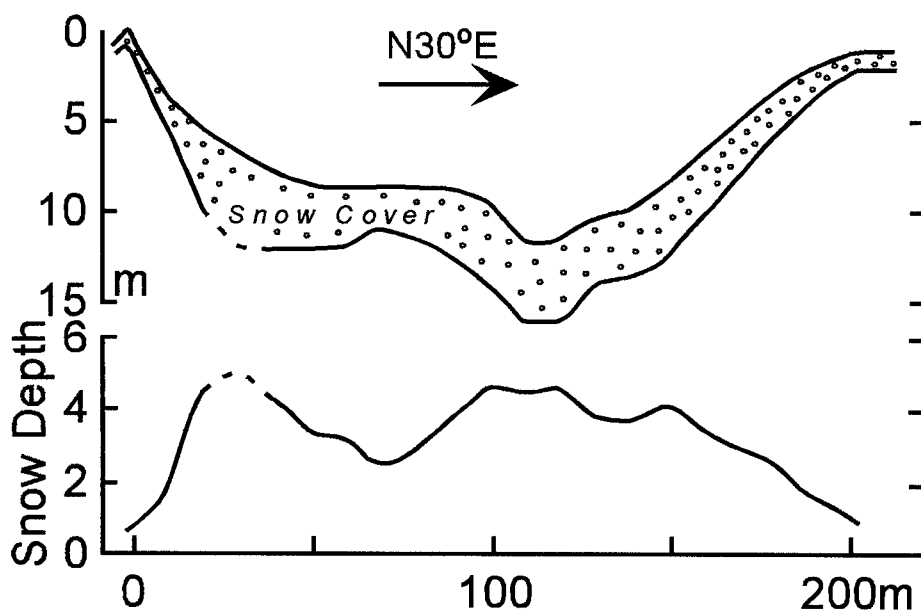


**Fig. 6.4** Snow distribution at 1600 m ASL above timberline on the western slope of Mt. Asahidake areas (see figs. 2.1 and 2.2 for location, after Yamada *et al.* 1978)

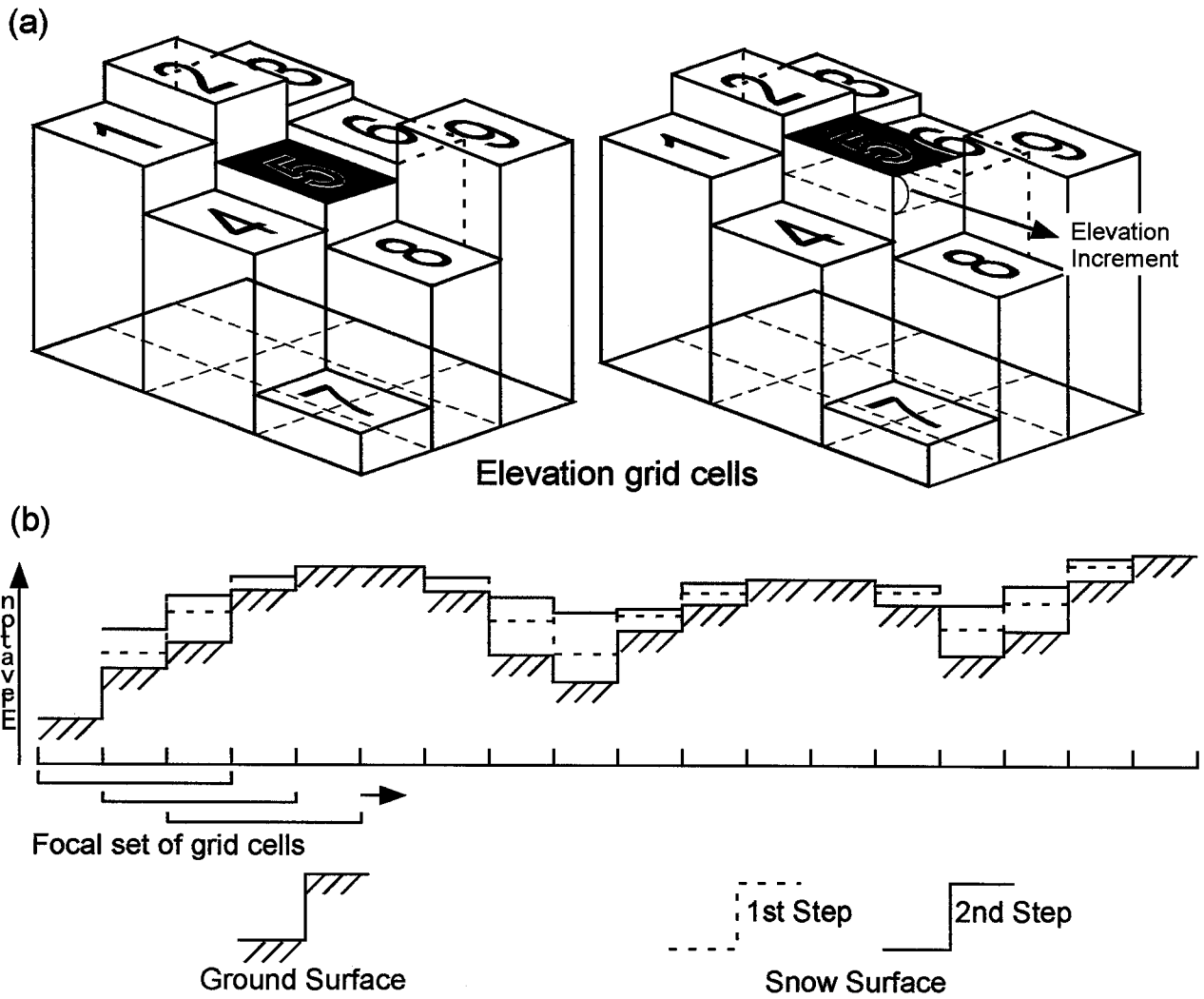


**Fig. 6.5** DEM-based simulation of snow cover distribution. (a) 3x3 neighborhood calculation for increment the terrain elevation and (b) its iteration for the regional snow cover simulation presented by cross-section.

$$r = CA * CI. \quad (6.6)$$

The coefficient depending on the slope aspect ( $CA$ ) was approximated by the following trigonometric function:

$$CA = a * \cos(\theta - \alpha) + b. \quad (6.7)$$

Where  $\theta$  is the slope aspect ranging from 0 (northern slope) to 360 degrees following a clockwise rotation, the parameters  $a$ ,  $b$  and  $\alpha$  are determined by the frequencies of wind directions during the winter. Equation 6.7 takes account for the wind deflection due to local topography. Fig. 6.6 shows the frequencies of wind directions during winter obtained at a ropeway station in the eastern slope of Asahidake (1600 m ASL above timberline). Westerly winds are predominant, while easterly winds are rare. This suggests that snow accumulates easily on the eastern leeward slopes, while less snow accumulates on the western slopes. For approximation of these wind frequencies the parameters of  $a$ ,  $b$  and  $\alpha$  were determined as 0.3, 0.5, and 90, respectively.

Yamada *et al.* (1978) also observed that snow does not accumulate on slopes steeper than  $60^\circ$ , which corresponds to the angle of repose for snow cover, and that the depth of snow cover decreases with inclination. The coefficient depending on the inclination ( $CI$ ) was approximated by the following quadric functions:

$$CI = \left( \frac{\phi - 60}{60} \right)^2 \quad \{0 \leq \phi \leq 60\} \quad \text{and} \\ CI = 0 \quad \{60 \leq \phi \leq 90\} \quad (6.8)$$

where  $\phi$  is the inclination ranging from 0 (flat) to 90 (vertical) in degree.

After completing the processing on one grid cell as described above (equation 6.5), the next set of  $3 \times 3$  grid cells including the overlapping 6 grid cells was initiated: *i.e.* the focal grid cell is No. 6, overlapping grid cells are No.2,3,5,6,8 and 9 (fig. 6.5). This processing is done for all grid cells (fig. 6.5b).  $r$  is recalculated as topography changes with snow depth. After a number of iterations, it appears that leeward concave terrains are covered with thick snow cover, while the windward convex and flat summit terrains

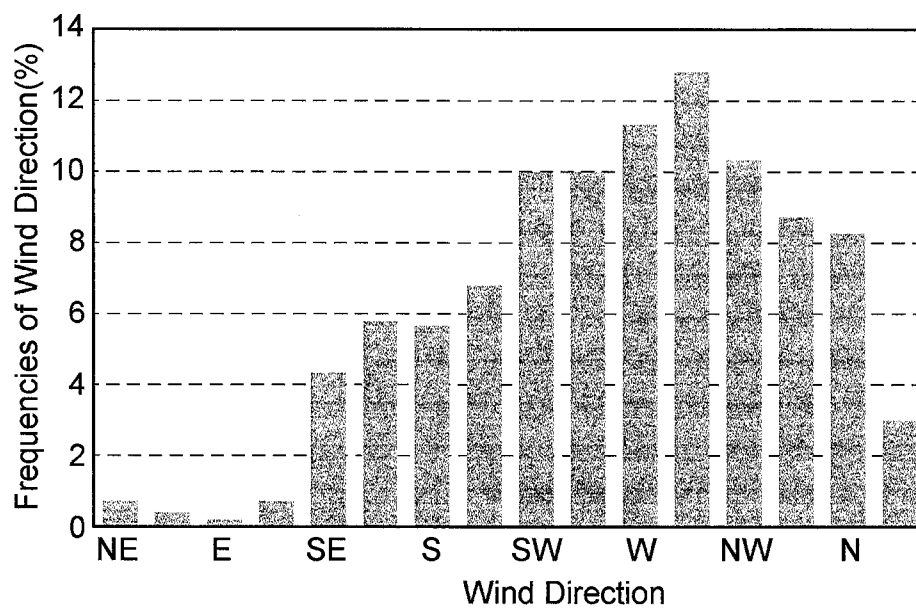


**Fig. 6.6** Frequency of the wind directions above timberline during winter at the Sugatami Ropeway Station at the eastern slope of Asahidake (after Yamada *et al.*1978).

remain snow free (fig. 6.5b).

Iterative calculations were carried out in order to increase the elevation of each grid cell in the DEM. The numbers of grid cells with less than 1.0 m snow cover decreased with increasing iterations (fig. 6.7), simulating that the concave terrain is covered with snow. After 15 iterations, no more significant decrease occurred. This indicates that snow has filled concave terrains where the streamlines separate away from the surfaces and snow accumulates as shown schematically in fig. 6.4.

#### **6-4-1-2. Model validation**

Since the model is based on empirical ways, it is not possible to derive any quantitative data from the model. Rather, it should be viewed as producing qualitative maps showing relative distribution patterns of snow cover. The simulated spatial distribution of snow cover was validated by cross-referencing the model output with the vegetation distribution, which coincides with the snow cover distribution, and by analysis of an oblique air photograph.

Temporal-spatial variation of snow cover produces obvious differences in vegetation communities as described in chapter 5 (fig. 5.2). Fig. 6.8 shows the simulated distribution of the snow cover after 5, 10, 15 and 20 iterations. Assuming that these figures also represent the evolution of snow cover distribution from early- to mid-winter, the snow starts to accumulate mainly on the eastern leeward slopes of the patches of *Pinus pumila*, as typically shown in the eastern slope of Mt. Koizumidake and Hokkaidaira plateau, and southwest slope of Mt. Koizumidake (Iteration 5, fig. 6.8). The flat summit areas remain snow free, where few *Pinus pumila* patches were distributed. Since *Pinus pumila* is usually buried in snow until early to late winter (Okitsu and Ito, 1984) and indicates the boundary between snow covered and wind-blown grounds (fig. 5.2), this simulated snow cover evolution should be reasonable.

For qualitative checks of the simulated spatial distribution of snow cover, an oblique photograph taken in mid-April, when the thickest snow accumulates in a year, was used (fig. 6.9). The model showed that concave topographic areas are likely to be covered with snow, while the flat mountain ridges and the eastern windward slopes are remained snow-free. Furthermore, the model simulated that less snow accumulates on the frontal

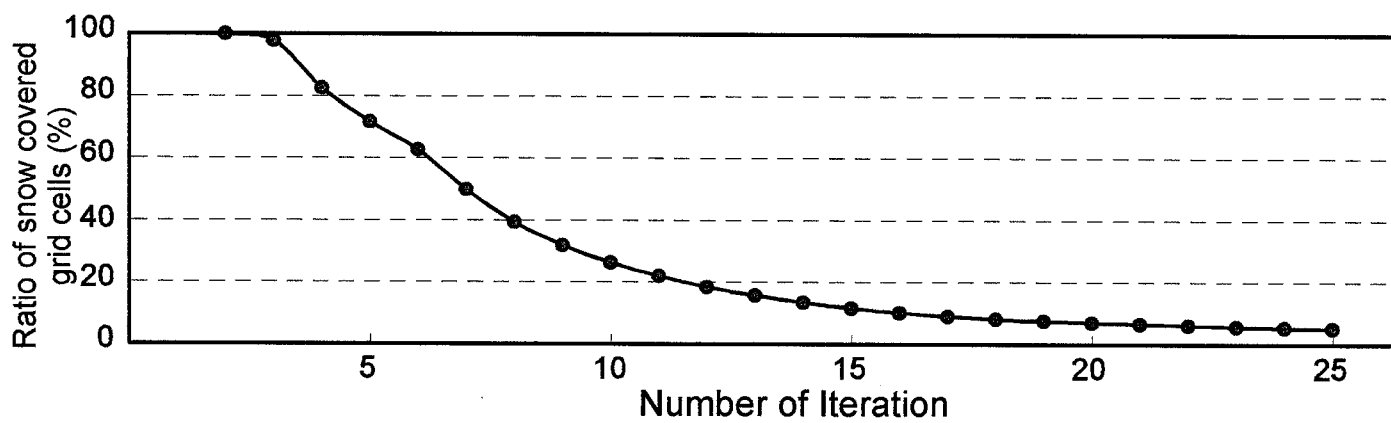


**Fig. 6.7** Cumulative percentages of the grids with snow depth shallower than 1.0 m.

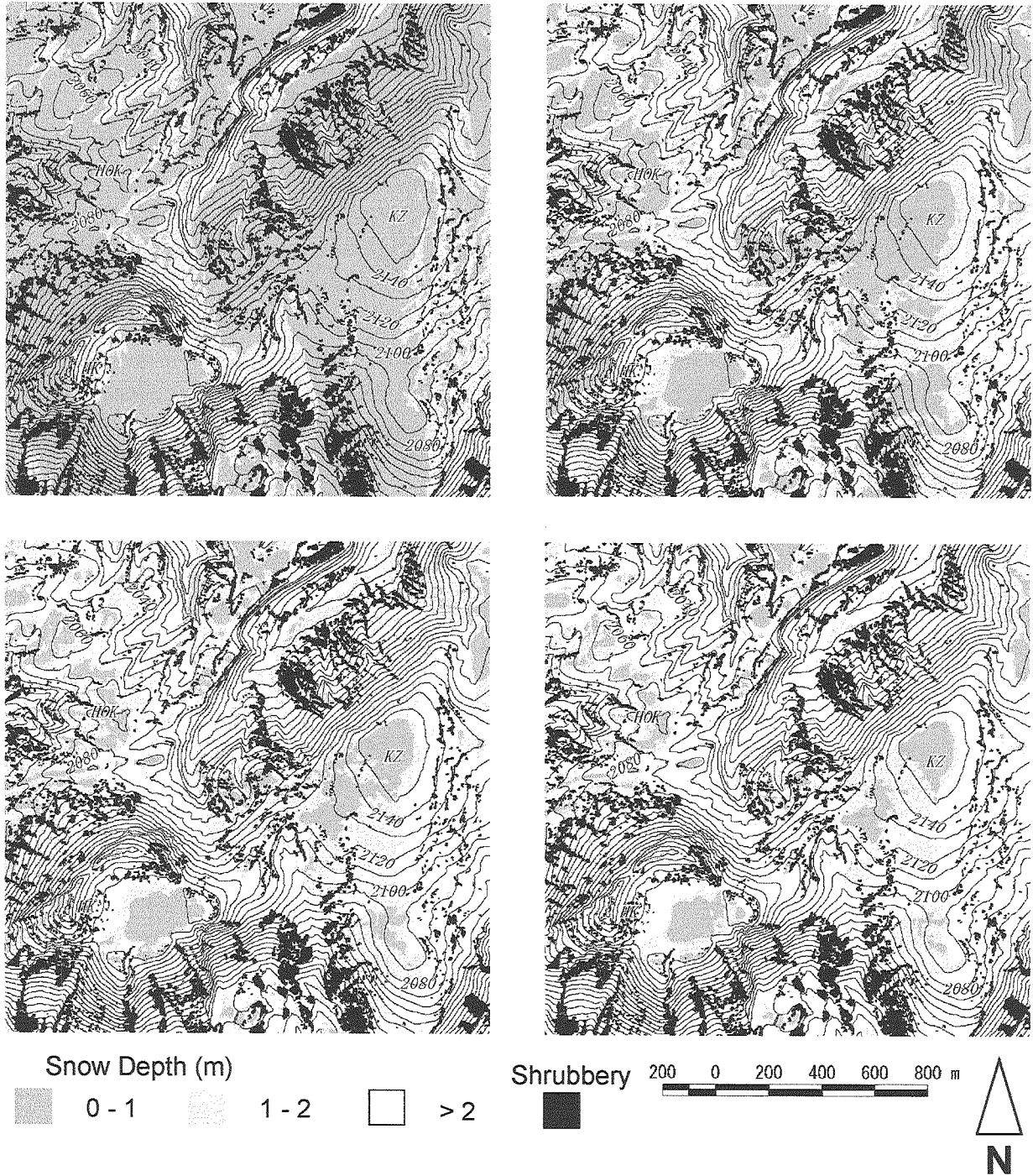


**Fig. 6.8** Simulated spatial distribution of snow cover after 5, 10, 15 and 20 iterations. HK : Mt Hakuundake, KZ; Mt. Koizumidake

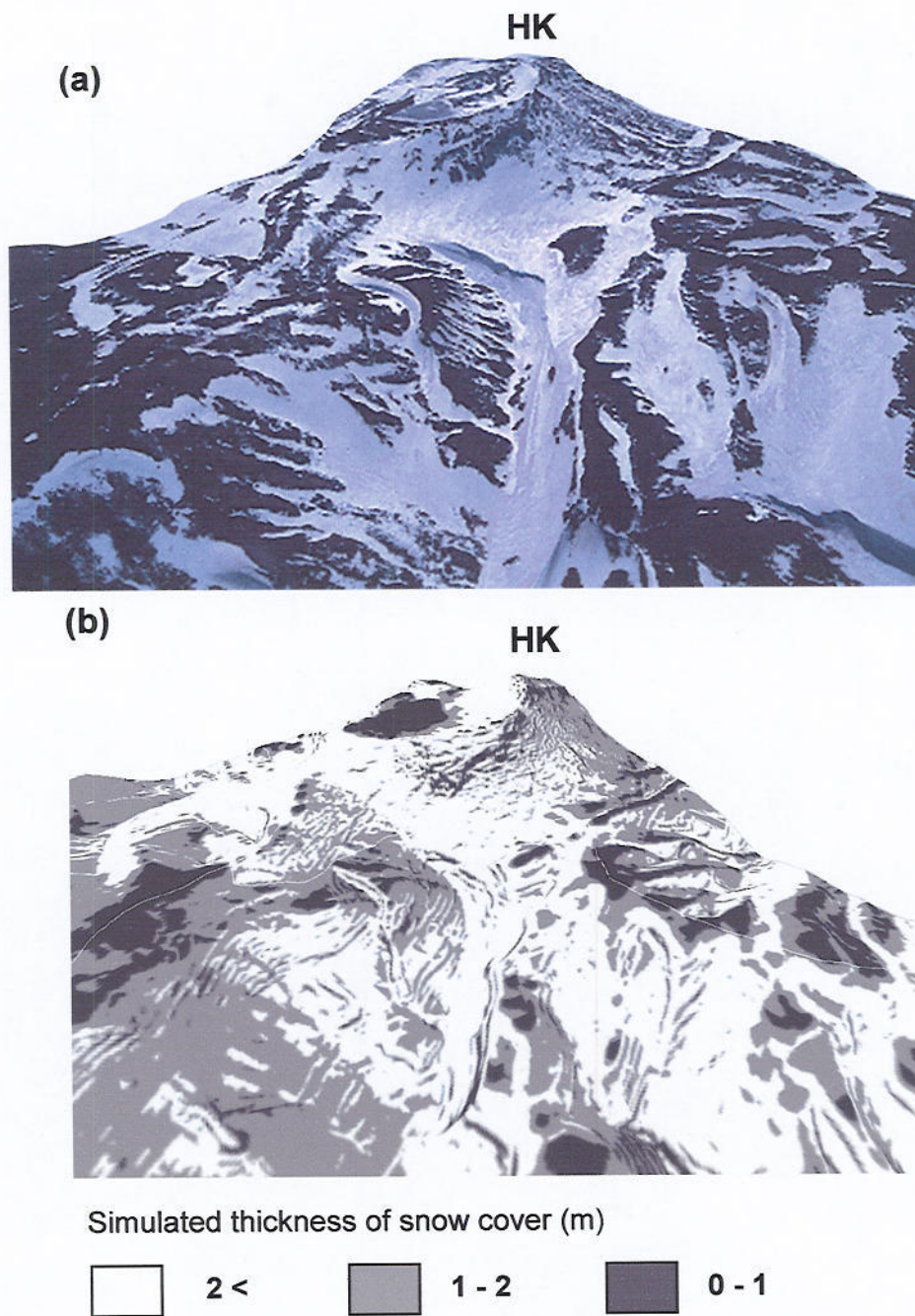


**Fig. 6.9** Comparison between (a) oblique aerial photograph and (b) the simulated spatial distribution of snow cover in the Mt. Hakuundake (HK) and its surroundings

slopes of the lobate-shaped landforms and on the steep bedrock cliffs indicated (fig. 6.9). The model also delineated the boundaries between areas covered with snow and less snow accumulation on the flat summit areas.

## **6-4-2. Modelling CFTI**

### **6-4-2-1. Background**

Spatial modelling permafrost should be based upon analysis of surface energy exchanges. Surface energy exchanges were represented by freezing and thawing indexes on the ground surface. The freezing index is the total of the mean daily temperatures below freezing point in a year, while the thawing is the total of the mean daily temperatures above freezing point in a year. Permafrost can develop where the value of freezing index is larger than that of thawing (Harris 1981a, 1981b).

### **6-4-2-2. Assumption of thermal effect by snow cover and snow cover evolution**

As described previously, ground surface temperatures are strongly controlled by the thickness and duration of snow cover, which has a very complex influence on the ground thermal regime (*e.g.* Goodrich, 1982). In general, short-term variations in air temperature and radiation rarely reach the snow-covered ground, where the snow cover is thick enough. A thick snow cover in early winter prevents cooling of the ground. In contrast, remaining snow cover in spring and summer prevents heating of the ground surfaces. Therefore, thermal effects of snow cover should be considered both temporally and spatially.

Fig. 6.10 shows the representative annual variations of ground surface temperature (GST) at sites with different snow cover conditions during 1999-2000 together with air temperature variations during same period. Owing to the thermal insulation effect by snow cover, annual and daily fluctuations of GSTs are significantly different. On the site with *alpine snow hostile scrub*, where moderate thickness of snow cover accumulates (fig. 5.2), temporal variations of GST coincide with those of air temperature. On sites with *alpine snow-hostile scrub*, where moderate thickness snow cover accumulates (fig. 5.2), fluctuations of temporal variations of GST are damped during winter but coincide with those of air temperature during summer. On sites with *alpine snow-bed*

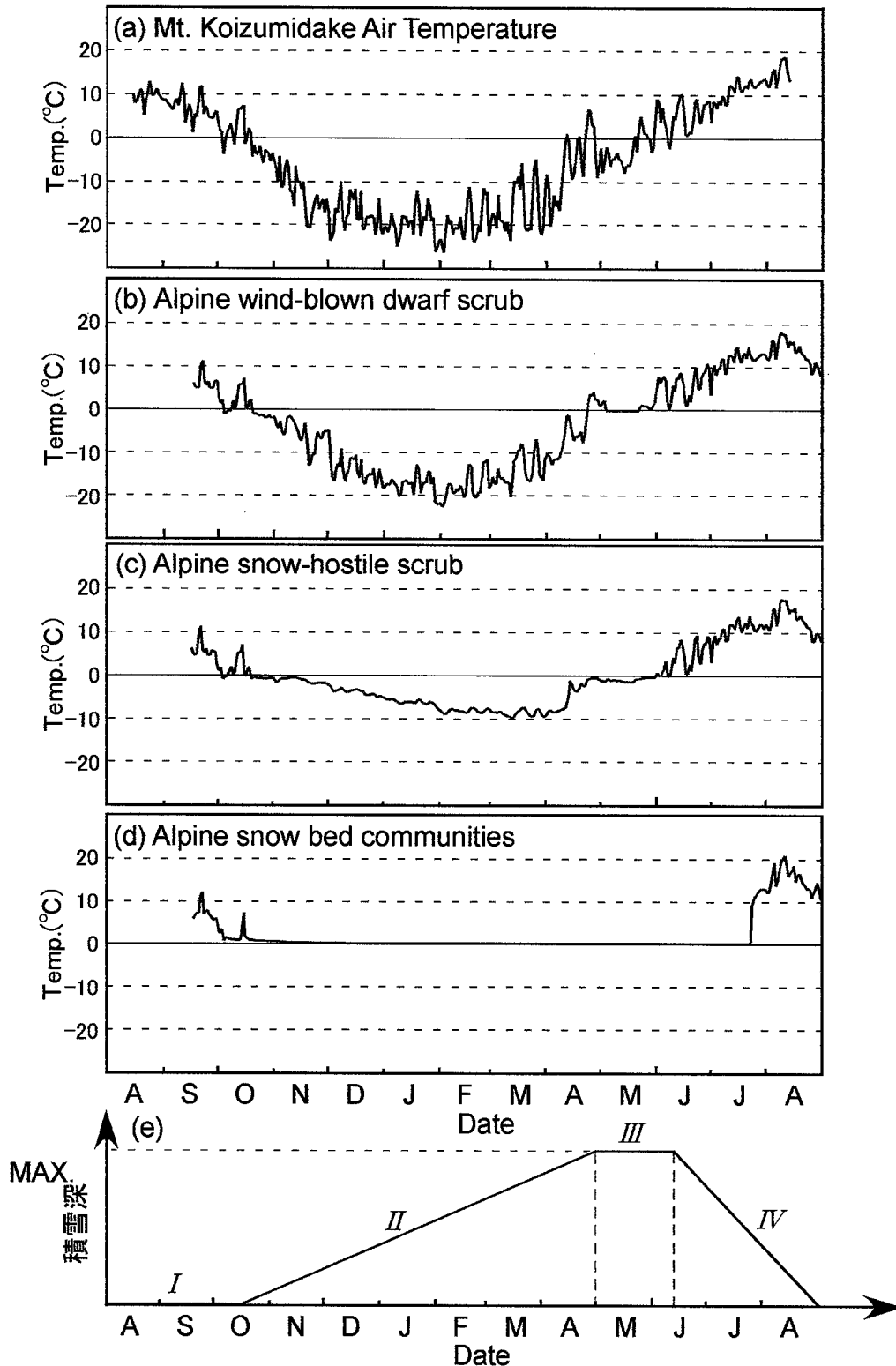


**Fig. 6.10** Annual air (a) and ground surface temperature (b,c,d) variation at the representative sites with different snow cover conditions. Assumed snow cover evolution are also shown in (e). Stage *I*, *II*, *III* and *IV* correspond to the periods of snow free, dry snow, maximum of snow cover and snow melting, respectively. The maximum thickness of snow cover at each grid cell is assumed to be that simulated in fig. 6.9.

*communities*, where thick snow cover accumulate, GST shows no temperature fluctuations and remain 0 °C during winter, spring and early summer. Until the end of July, GSTs show fluctuations and coincide well with those of air temperature. Common behavior was observed among three GST variations. GST remains stable and is nearly 0 °C until end of April to completion of snow melting. This duration depends on the thickness of snow cover at each site.

Snow cover evolutions were assumed based on the field observations and snow cover distribution simulated in the previous section (figs. 6.10e and table 6.1). In normal years, first snowfall occurs between mid-September and early-October in the summit areas of the Daisetsu Mountains. This snow cover, however, soon disappears, because positive daily air temperatures are dominant during this period (fig. 6.11a). After the mid-October, air temperatures turn negative (fig. 6.11a). This suggests that the snow is likely to linger until this time. By the end of April, subzero air temperatures are dominant (fig. 6.10a). Accordingly, during 15 October and 1 May in next year the thickness of snow cover at each grid cell is assumed to increase linearly such that:

$$SC_{m,n+1} = SC_{m,n} + \left( \frac{SCM_m}{198} \right) \quad (288 \leq n \leq 365) \quad (6.9)$$

$$SC_{m,n+1} = SC_{m,n} + \left( \frac{SCM_m}{198} \right) \quad (1 \leq n \leq 121) \quad (6.10)$$

where  $SC_{m,n}$  is the thickness of snow cover at grid  $m$ , at Julian day  $n$ ,  $SCM_m$  is the maximum thickness of snow cover simulated at grid  $m$  (fig. 6.9), the Julian days 288, 365, 1 and 121 corresponds to 15 October, 31 December, 1 January and 1 May, respectively. The number 198 represents the duration between 15 October and 1 May and corresponds to the duration with snow accumulation.

Between the beginning of May and mid-June, the thickness of snow cover at every grid cells was assumed to be constant, because most of the incoming energy is used for the phase change of snow cover. Until mid-June, the thickness of snow cover assumed to be decreasing by linear trend. Miyamoto (1999) observed that a snow patch at the northeastern slope of Mt. Koizumidake has disappeared around 20 August in 1994, and that between end of August and early September in 1996 and 1997 the thickness of

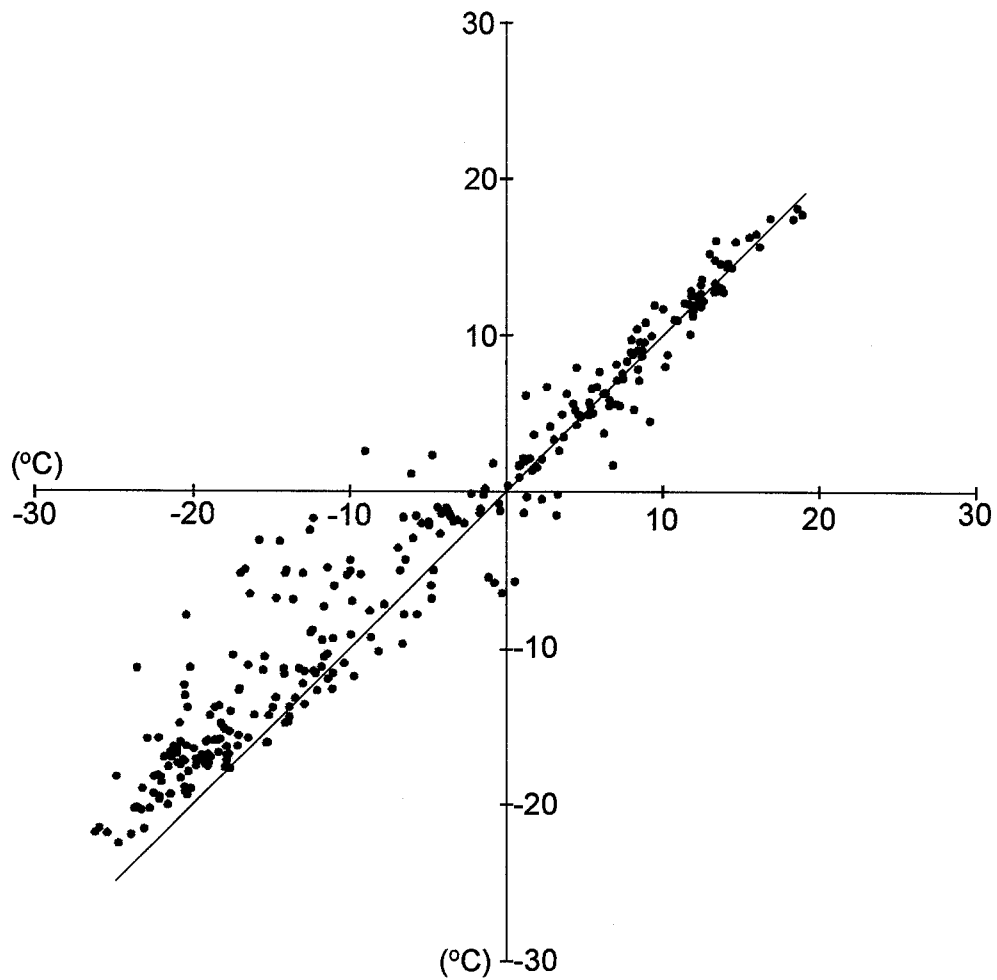


**Fig. 6.11** Comparison between daily mean ground surface temperature and daily mean air temperature during a year on the wind-blown ground, where nearly no snow accumulate during a year (Axis of abscissa: daily mean air temperature; Axis of ordinate: daily mean ground surface temperature).

snow cover decreased by almost linear trend. This snow patch is the largest one among Mt. Hakuundake in the simulated area (Miyamoto, 1999), suggesting that the duration of this snow patch should be the longest of all the snow patches except some perennial snow patches in the simulated area. The thickest snow cover has been estimated on a grid cell within this snow patch (fig. 6.9). Using such observations it is assumed that all the snow disappears at 31 August in the simulated area and that the thickness of snow cover at each grid cell decreases by a linear trend as following equation:

$$SC_{m,n+1} = SC_{m,n} - \left( \frac{SCM}{79} \right) \quad (165 \leq n \leq 244) \quad (6.11)$$

where a number 165 and 244 are correspond to 15 June and 1 September, respectively.  $SCM$  is the maximum thickness of snow cover estimated among all grid cells and was substituted for 8.1. If  $SC_{m,n}$  reaches zero at a grid cell, calculation by equation 6.11 will not be carried out at this grid cell. Until 1 September to 15 October, it is assumed that all grid cells are snow free.

### 6-4-2-3. Model

According to the temporal variations in thermal insulating effect and the evolution of snow cover as assumed above, the temporal GST variations can be divided into four stages: Dry snow, Wet snow, Snow melting and Snow free stage. The GSTs at each stage were determined as follows.

#### (I): Dry snow stage

This corresponds to the period from early winter to spring. During this stage, the ground surface is covered with dry snow, which insulates the winter frost penetration as long as the snow cover is thick enough. The amplitudes of daily and annual variations in GST decrease with increasing thickness of snow cover. Although despite the fact that air temperatures show daily fluctuation, the ground surface temperatures remain 0 °C on the snow-covered ground due to the insulating effect by thick snow cover (fig. 6.10d). Where snow cover is moderate by thick, the amplitudes of daily fluctuation are smaller than those of wind-blown ground, but larger than those of snow-covered ground (fig.

6.10).

(II): Wet snow stage

This corresponds to the period from late spring to early summer. During this period, since the temperatures of snow cover reached melting point, GSTs remain at 0 °C at all sites where snow accumulates. The duration of this stage depends on the timing of snow melting and thus on the amounts of snow cover thickness. Obviously, snow disappears earlier on wind-blown ground than on snow-covered ground.

(III): Snow melting stage

This corresponds to a period from early- to late-summer. GST beneath the snow cover remain at 0 °C. On the other hand, daily mean GST does approach air temperatures at the sites where snow has disappeared (fig. 6.11).

(IV): Snow free stage

This corresponds to a period from late-summer to early winter, before the first snowfall. During this stage, the lack of snow cover means that ground surface temperatures are close to air temperatures (fig. 6.11). The duration of this stage also depends on when snow first disappeared and on when the first snowfall comes.

CFTI at grid cell  $m$  is calculated by the following equations;

$$CFTI_m = \sum_{n=1}^{365} GT_{m,n} \quad (6.12)$$

where  $CFTI_m$  is the CFTI at grid cell  $m$  and  $GT_{m,n}$  is the daily mean GST at day  $n$  at grid cell  $m$ . Referring to the correlation between daily mean air temperatures and daily mean GST on the wind-blown ground (fig. 6.11), daily mean air temperatures are approximated to  $GT_{m,n}$  at a grid cell without snow cover.

In the grids with snow cover, the insulation due to snow cover have been determined by comparison between means of daily air temperature and those of ground surface temperature monitored at a number of sites. The snow insulating index ( $SII$ ) was defined by follows:

$$GST_{MIN} + GST_{MAX} = SII * (AT_{MIN} + AT_{MAX}) \quad (6.13)$$

where  $GST_{MAX}$ ,  $GST_{MIN}$  are daily maximum and minimum GST, respectively and  $AT_{MAX}$ ,  $AT_{MIN}$  are daily maximum and minimum air temperature, respectively. Daily mean GST ( $GT$ ) and air temperature ( $AT$ ) are approximated by:

$$GT = \frac{GST_{MIN} + GST_{MAX}}{2} \quad \text{and}$$

$$AT = \frac{AT_{MIN} + AT_{MAX}}{2}. \quad (6.14)$$

Therefore, daily mean GST at grid  $m$  at day  $n$  is determined by:

$$GT_{m,n} = SII_{m,n} * AT_n \quad (6.15)$$

where  $AT_n$  represents daily mean air temperature at day  $n$  and  $SII_{m,n}$  the snow insulating index at grid  $m$  at day  $n$ .

$SII_{m,n}$  is a variable depending on the thickness of snow cover. In order to determine  $SII_{m,n}$ , the mean ratio of daily air and to surface temperature means (MRAG) was considered. Fig. 6.12 shows the relation between MRAG during 15 March and 31 March, when the thickest snow cover accumulates in a year, and the thickness snow cover simulated as shown in fig. 6.9. In areas with 2.5 m of snow cover daily air temperature are sent to fluctuate affecting the ground surface whilst areas with more than 2.5 m show almost no response. Assuming linear correlation between MRAG and the thickness of snow cover less than 2.5 m,  $SII_{m,n}$  was approximated such that:

$$SII_{m,n} = -0.4 * SC_{m,n} + 1 \quad (0 \leq SC_{m,n} \leq 2.5) \quad (6.16)$$

$$SII_{m,n} = 0 \quad (2.5 < SC_{m,n}). \quad (6.17)$$

In this calculation, daily mean air temperatures were computed by the field measurements during August 1998 and July 1999.

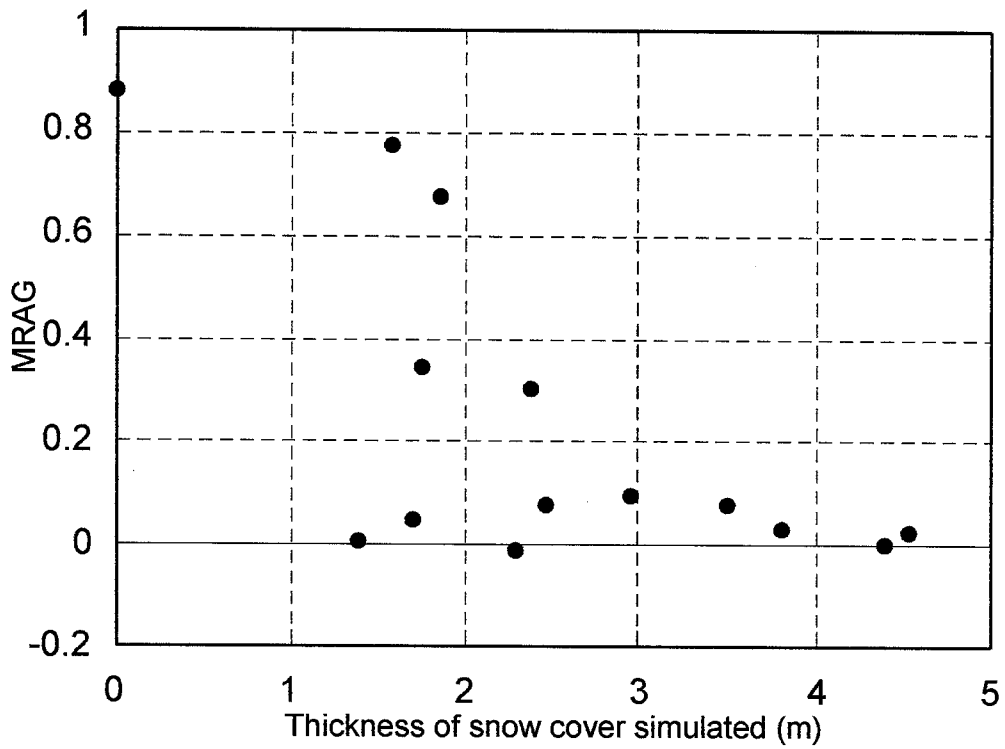


**Fig. 6.12** Relation between mean ratio of daily mean between air and ground surface temperatures (MRAG) and the thickness of snow cover between 15 March and 30 April, during which the snow cover is thickest in a year.

#### **6-4-2-4. Result and validation**

Fig. 6.13 shows the calculated distribution of CFTI over the areas simulated. These CFTI values were validated by the results of annual ground surface temperature monitoring during the same period at a number of sites (fig. 6.14). The coefficient of correlation and the slope of correlated line are 0.8374 and 1.0968, respectively. The intercept of this correlated line is 97.7, which is within the error of temperature sensors. These correlation values suggest that this model can simulate CFTI very well.

### **6-5. Correlation between the proxies estimated and field evidences of permafrost occurrences**

#### **6-5-1. Correlation between PR and Permafrost occurrence**

The distribution of total amount of potential solar radiation (PR) over the study sites from 01 May until 30 October was shown in fig. 6.15. PR received ranges from 2 to 778 kW h m<sup>-2</sup> over the area. This map demonstrates that the northern slopes of Mt. Hakuundake and Mt. Koizumidake receive the lowest levels of radiation in response to the large slope gradient. The small PR areas coincide well with block slopes, *i.e.* HK#1 and HK#2, where permafrost is considered to be present by DC resistivity imaging and MAST (figs. 5.19 and 5.20). The occurrence of permafrost underneath the block slopes may be due to this reduced PR. The same explanation can be applied to the predicted occurrence of permafrost on the outer side of Mt. Hakuundake crater and the northern slope of Mt. Koizumidake where permafrost probably underlie (fig. 6.15).

On the other hand, special variation in the amount of PR is insignificant on the flat summit areas. For examples, ground temperatures at 1.0 m depth show large variations and permafrost is found beneath the stations with low ground temperature along the lines HOK#2 and HOK#3, (figs. 5.6 and 5.8), although no significant differences in PR were found along these lines. In the Mt. Koizumidake areas, the SGTs on the northern slope (site: KZ#3) were higher than those of the southern slope (site: KZ#1), although permafrost has been found at both sites (figs. 5.10 and 5.14). The difference in active layer can be explained by these differences in PR.

Some permafrost distribution models based on the distribution of PR have been

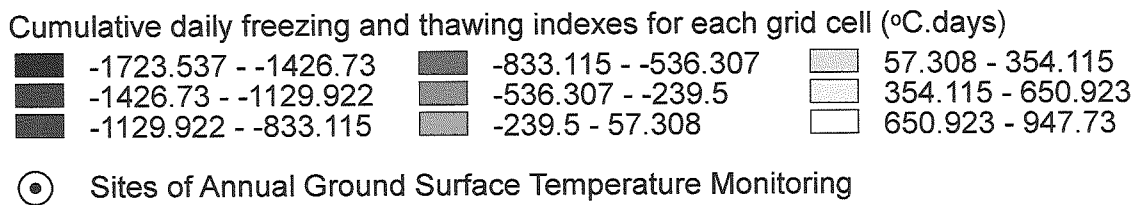
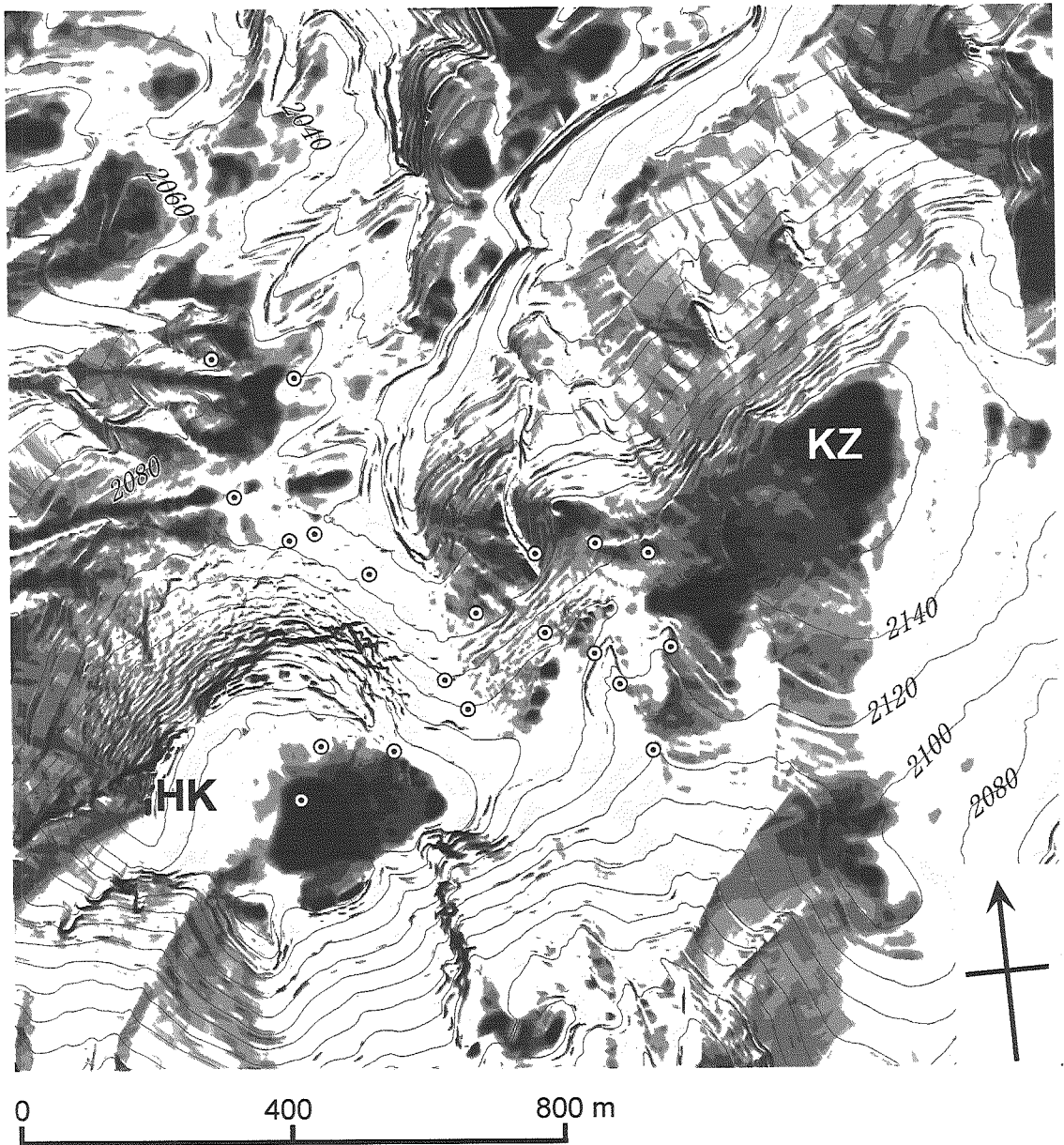


**Fig. 6.13** Simulated distribution of cumulative freezing and thawing indexes through a year (1998 - 1999). HK: Mt. Hakuundake, KZ: Mt. Koizumidake  
Contour Interval is 10 m.

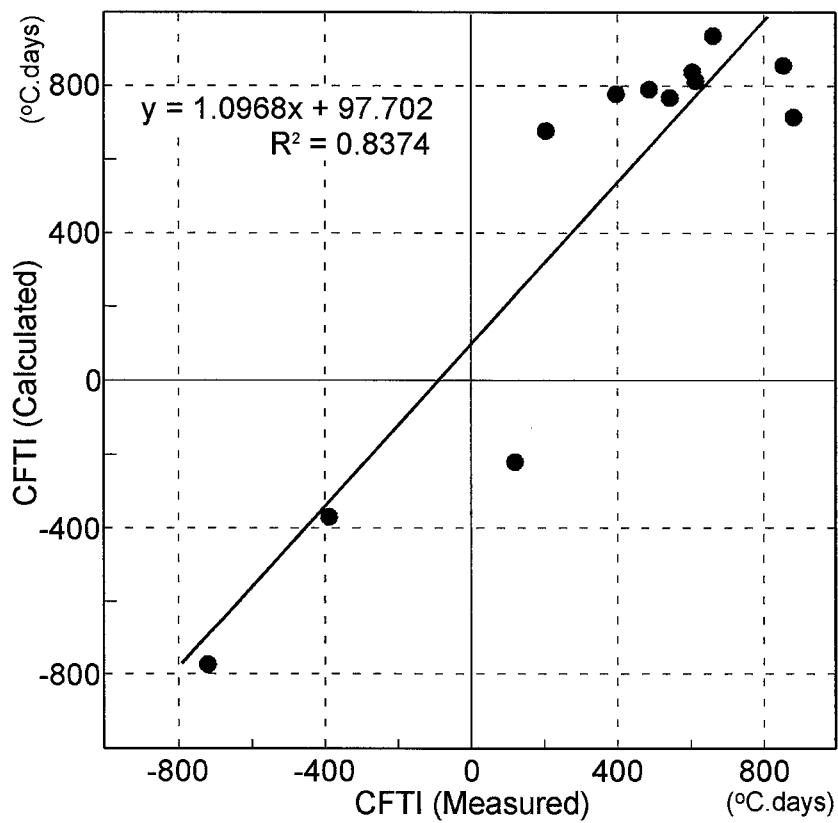
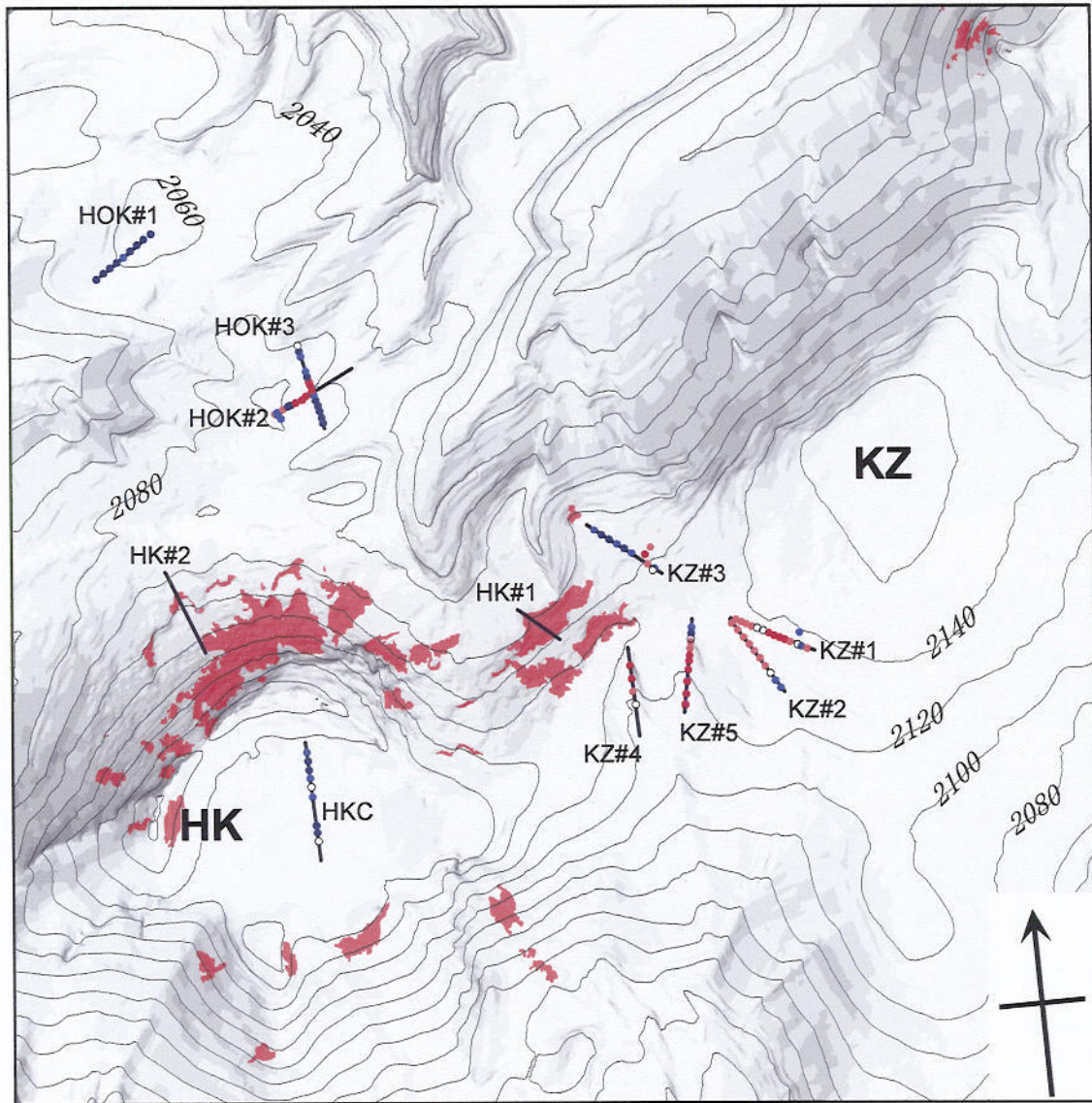
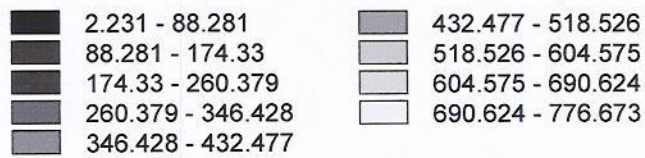


**Fig. 6.14** Correlation between simulated and measured cumulative freezing and thawing indexes. CFTI is abbreviation for Cumulative Freezing and Thawing Indexes on the ground surface in a year.



**Total amount of Potential Solar Radiation(kWhm<sup>-2</sup>)**



**Ground Temperature at 1.0m depth(°C)**

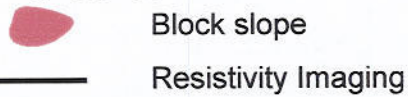


**Fig. 6.15** Estimated total amount of potential solar radiation between 1-May and 30-October.

developed for the European mountains (Funk and Hoelzle, 1992; Hoelzle, 1992; Hoelzle and Haerberli, 1995; Hoelzle, 1996). These models can predict the occurrence of permafrost at the site where PR is extremely reduced even in low altitudes (Funk and Hoelzle, 1992; Kneisel *et al.*, 2000). PR distribution does not predict the occurrences of permafrost at the summit areas of the Daisetsu Mountains. This inconsistency is probably due to the difference in the resolution for spatial simulation. Modelling in the European mountains has relatively coarse resolutions, *i.e.* 100 to 250 m grids (Funk and Hoelzle, 1992), 25 to 100 m (Hoelzle and Haerberli, 1995) and 50 m (Imhof, 2000). PR estimation by these resolutions might predict the occurrence of permafrost beneath the northern slopes of Mt. Hakuundake and the northeastern slopes of Mt. Koizumidake. In order to predict permafrost occurrence on the flat summit areas a higher resolution for the DC resistivity imaging and SGT measurements is needed. PR estimation alone is insufficient.

#### **6-5-2. Correlation between CFTI and Permafrost occurrence**

The CFTI distribution shows the good correlation with permafrost occurrences on the summit areas, satisfying the resolution surveyed by DC resistivity imaging and SGT measurements as shown in chapter 5. Fig. 6.16 shows the areas with negative CFTI values, thus reflecting the areas where permafrost can develop. At the sites of HOK#1, permafrost was found throughout the line by SGT measurements and DC resistivity imaging (fig 5.4). At the sites HOK#2, HOK#3, KZ#3 and KZ#5, permafrost was found beneath the areas with negative CFTI (figs. 5.6, 5.8, 5.14 and 5.18). At the site KZ#4, no permafrost was found where positive CFTI had been calculated (fig. 5.16).

The occurrence of permafrost beneath the block slopes and steep slopes can be explained also by this CFTI distribution. The areas with negative CFTI are distributed on the block slopes, *i.e.* sites HK#1 and HK#2 (figs. 5.19, 5.20 and 6.16). This CFTI distribution also predicts the occurrences of permafrost beneath the outer side of Mt. Hakuundake crater and the northeastern slope of Mt. Koizumidake.

The accuracy of the CFTI distribution is strongly controlled by the resolution of DEM. Using DEM with less resolution, snow cover distribution might be simulated incorrectly and thus estimated CFTI distribution might not be accurate. CFTI simulated using precise DEM represents a good proxy for predicting permafrost distribution by

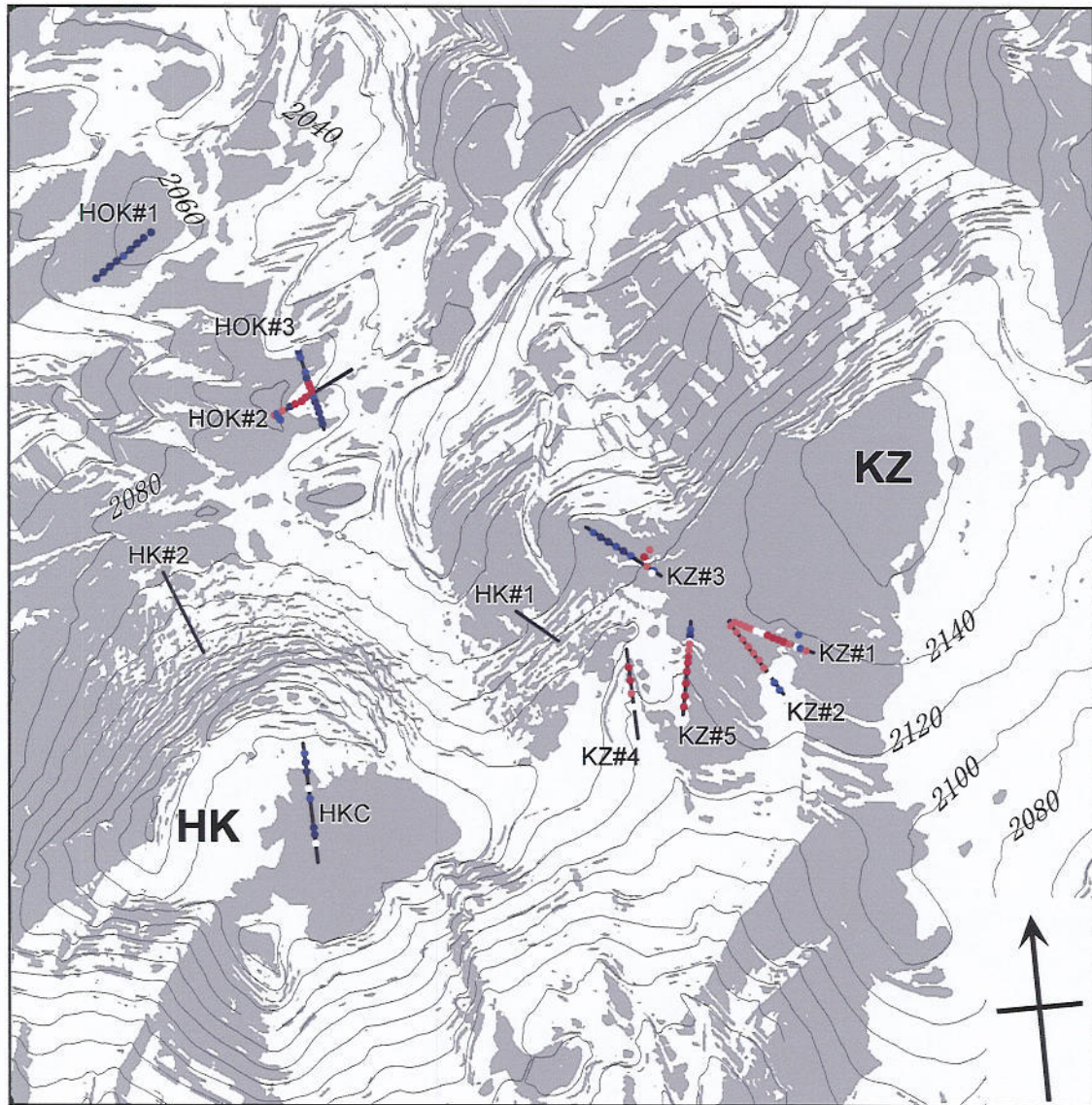


**Fig. 6.16** The areas with negative values of cumulative freezing and thawing indexes (CFTI). Ground temperatures at the depth of 1.0 m are also shown. Contour interval is 20 m.

high resolution on the flat summit areas where snow is re-distributed by strong wind.

## **6-6. Spatial changes of mountain permafrost in the Daisetsu Mountains**

### **6-6-1. Significance of permafrost in the summit areas of the Daisetsu Mountains**

As a consequence of global warming, mean annual air temperatures are predicted to increase (*e.g.* Hulme *et al.*, 1999), leading to changes in the distribution and duration of snow cover. As mountain permafrost can only develop in areas that experience a specific temperature range (generally only a few degrees below zero), global warming could potentially result in the degradation of mountain permafrost.

In the European mountains and Himalaya, the summit areas are covered with glaciers, which restrict the growth of permafrost. Permafrost has mostly been identified on the mountain slopes, using geomorphic features formed by creeping of ice-rich permafrost, *e.g.* rock glaciers (Haeberli, 1985; Barsch, 1992; 1996; Barsch and Jacob, 1993; Jacob, 1992; Ishikawa *et al.*, 2001). Mountain permafrost in the Daisetsu Mountains is mostly distributed beneath the wind-blown ground on the summit areas where air temperature directly affects the ground thermal regimes. Changes in air temperature and precipitation would be anticipated to cause drastic changes in the distribution of permafrost.

Spatial modelling of mountain permafrost by a proxy of CFTI allows me to predict changes of permafrost distribution. Climatic predictions provided by Global Circulation Model (GCM) are used for this prediction.

### **6-6-2. Global Circulation Model**

The Global Circulation Model (GCM), HadCM2 was adopted for climate scenarios. It was developed at the Hadley Center for Climate Prediction and Research in Britain. This GCM model has high-resolution, coupled ocean-atmosphere GCMs and has a spatial resolution of 2.5 ° latitude and 3.75 ° longitude and representation produces a grid box resolution of 96×73 grid cells. This produces a surface spatial resolution of about 417×278 km, reduced to 295×278 km at 45 degrees North and South. This is the highest ocean-atmosphere GCM currently operational for transient climatic changes

experiments.

There have been over 20 climate change integrations performed with HADCM2. These include the control run (HadCM2CON), four ensembles of four members with different forcing scenarios. Among all variables, only air temperature in the HHGSAX ensemble, which includes the effects of both greenhouse gases and sulfate aerosols (Hardley Center, 1997), was used in the response model of high altitude permafrost with respect to climatic change. Data are available at daily, monthly, mean monthly time steps or pre-constructed 30-year means for 2010-2039, 2040-2069 and 2070-2099. Air temperature forecast results of 30-year means are shown in table 6.1 and used for simulation.

### **6-6-3. Predicted changes of permafrost distribution**

The data obtained at Mt. Koizumidake during August 1998 and July 1999 was used to represent current air temperature. The increasing air temperatures listed in table 6.1 were added to all daily means of this baseline. The effect of changing snow cover duration was not taken into account.

The results of simulation for the three time periods are shown in fig. 6.17. If the simulation result is regarded as the baseline, then spatial distribution changes in permafrost can be obtained. Since the current permafrost distribution is well calibrated based on field surveys (fig. 6.16), this extrapolation for future prediction should be reasonable.

Fig. 6.17 also shows the spatial ratio of permafrost over the area. It is predicted that the extent of the permafrost area will not decrease significantly until the 2020s (43.47 %), but will significantly decreasing until the 2080s (17.6 %). Permafrost is predicted to disappear more rapidly on the northern slope of Mt. Koizumidake than in the other areas. Permafrost underneath the block slope of Mt. Hakuundake will also disappear before the 2080s.

**Table 6.1** Predicted changes of monthly mean air temperature. The scenarios are presented for three future periods – 30-years mean centered on the 2020s, the 2050s, the 2080s – and are expressed with respect to the mean 1961-1990 climate. These predictions were made using HadCM2gsax, which combined 1 % CO<sub>2</sub> concentration with the negative forcing from sulphate aerosols.

	HHGSAX20 2010 - 2039	HHGSAX50 2040 - 2069	HHGSAX80 2070 – 2099
January	0.97	1.84	2.93
February	0.89	1.69	2.63
March	0.93	1.83	2.77
April	0.92	1.86	2.74
May	0.89	1.74	2.62
June	0.86	1.56	2.58
July	0.71	1.47	2.39
August	0.56	1.50	2.37
September	0.43	1.27	2.3
October	0.73	1.56	2.54
November	1.34	1.97	3.02
December	1.33	1.97	3.00
Mean	0.88	1.69	2.66

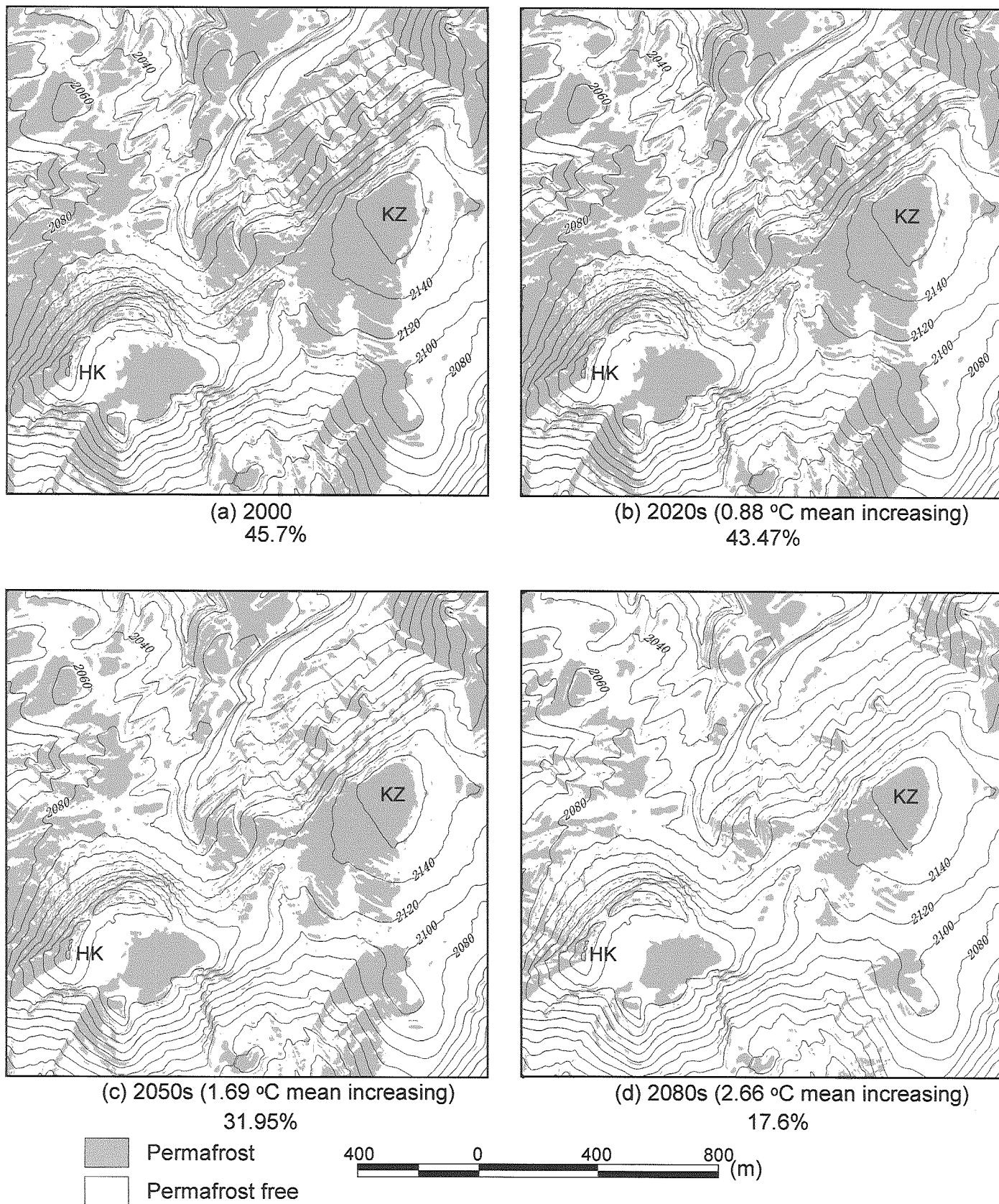


**Fig. 6.17** Simulated changes of permafrost distribution. Percentages of areas with permafrost are also shown. HK: Mt. Hakuundake, KZ: Mt. Koizumidake

## Chapter 7 Conclusions

The extent and thickness of permafrost in the Daisetsu Mountains were evaluated by means of geophysical methods, ground temperature monitoring and measurements. Spatial modelling of permafrost was also attempted on the basis of GIS techniques using precise DEM as base map. The following conclusions have been drawn from this data.

1) The occurrence of permafrost beneath snow cover was identified by means of BTS mapping, BTS monitoring and DC resistivity sounding. Cold heat penetrations through the snow cover and the ventilation effect within the surficial blocky layer are the predominant factors for growth and preservation of permafrost beneath snow cover.

2) Empirical BTS criteria by Haeberli (1973) should be applicable for mapping permafrost in the Daisetsu Mountains. Permafrost occurs beneath snow cover on the sites with three thermal processes; cooling in autumn and heat prevention due to snow retention until summer, direct cold heat penetration, and cold air concentration within the blocky materials. These thermal processes are revealed by BTS monitoring.

3) The lower limit of permafrost was estimated to be at 1650 m ASL, which is equivalent to MAAT at about  $-2.0$ . This estimation is based on the extrapolation of the thickness of permafrost delineated by DC resistivity sounding at different elevations.

4) Micro-scale permafrost distribution was revealed by a combination of DC resistivity imaging, with shallow ground temperature measurements and ground surface temperature monitoring through a year. Vegetation patches, which represent the snow accumulation and duration over an annual cycle represent good indicator for the occurrence of permafrost. The occurrence and thickness of permafrost is strongly controlled by snow cover, which prevent cold heat penetration from ground in the winter.

5) Spatial mountain permafrost modelling was attempted on the basis of precise DEM ( $2 \times 2$  m unit grid cell) and GIS analysis. Conventional models, which are based on the total amount of potential solar radiation, cannot explain the small scale distribution of permafrost as revealed by DC resistivity imaging and shallow ground temperature measurements. Instead, a model was developed based on the estimation of cumulative freezing and thawing indices (CFTI), which took into account the spatial and temporal thermal insulation effect by snow cover. The areas with negative CFTI show the

presence of permafrost. The modelled permafrost distribution coincided well with the field evidence.

6) Changes in areas with permafrost were simulated based on the GCM prediction currently available. In the 2050s, when MAAT is expected to increase by 1.69 °C, the areas with permafrost will start to reduce significantly. By the 2080s, the extent of permafrost will be reduced to approximately one thirds of current.

## References

- AGGR. (Associate Committee on Geotechnical Research).** 1988. *Glossary of permafrost and related ground ice terms. Permafrost Subcommittee*, National Research Council of Canada, Technical Memorandum **142**, 156pp.
- Anisimov, O.A. and Nelson, F. E.** 1996. Permafrost distribution in the Northern Hemisphere under scenarios of climate change: *Global and Planetary Change*, **14**, 59-72.
- Barsch, D.** 1988. Rock glaciers: In *Advances in Periglacial Geomorphology*, Clark MJ (ed.). Wiley: Chichester; 69-90.
- Barsch, D.** 1992. Permafrost creep and rockglaciers: *Permafrost and Periglacial Processes*, **3**, 175-188.
- Barsch, D. and Jacob, M.** 1993. Active rockglaciers and the lower limit of discontinuous alpine permafrost in the Khumbu Himalaya, Nepal. In *Proceedings, Sixth International Conference on Permafrost*, Beijing, South China University of Technology Press, Wushan Guanzhou, Vol. 1: 27-31.
- Barsch, D. and King, L.** 1989. Origin and geoelectrical resistivity of rockglaciers in semi-arid subtropical mountains (Andes of Mendoza, Argentina): *Zeitschrift für Geomorphologie*, **33**, 151-163.
- Bernhard, L., Sutter F., Haeblerli W, Keller F.** 1998. Processes of snow/permafrost-interactions at a high mountain site, Mürtel/Corvatsch, Eastern Swiss Alps. In *Proceedings of the 7th International Conference on Permafrost, Yellowknife, Canada, Nordicana*, **57**, 35-41.
- Berthling, I., Etzelmüller, B., Eiken, T. and Sollid, L.** 1998. Rock glaciers on Prins Karls Forland, Svalbard. I: internal structure, flow velocity and morphology. *Permafrost and Periglacial Processes*, **9**, 135-145.
- Brown, R. E. J.** 1967. *Permafrost in Canada*. Map 1245a, Geological survey of Canada, National Research Council of Canada, Ottawa.
- Brown, R. E. J. and Péwé, T.L.** 1973. Distribution of permafrost in North America and its relationship to the environment; a review 1963-1973. In: *Permafrost; North American Contribution, Second International Permafrost Conference, Yakutsk, USSR*. Washington DC: National Academy of Science, Publication 2115, pp. 71-100.

- Chang, P. L.** 1976. *Control of Flow Separation*, Hemisphere Pub. Corp., London, 523pp.
- Etzelmüller, B., Ødegård, R.S., Berthling, B. and Sollid, L.** 2001. Terrain parameter and remote sensing data in the analysis of permafrost distribution and periglacial processes: principles and examples from Southern Norway: *Permafrost and Periglacial Processes*, **12**, 79-92.
- Evin, M. and Fabre, D.** 1990. The distribution permafrost in rock glacier of the Southern Alps (France): *Geomorphology*, **3**, 57-71.
- Evin, M., Fabre, D. and Johnson, P. D.** 1997. Electrical resistivity measurements on the rock glacier of Grizzly Creek, St. Elias Mountains, Yukon: *Permafrost and Periglacial Processes*, **8**, 179-189.
- Fisch, W. Sr., Fisch, W. Jr. and Haerberli, W.** 1977. Electrical D.C. resistivity soundings with long profiles on rock glaciers and moraines in the Alps of Switzerland: *Zeitschrift für Gletscherkunde und Glazialgeologie*, **13(1/2)**, 239-260.
- Fujii, Y.** 1980. Distribution of alpine permafrost in the northern hemisphere and its relationship to the environmental condition. *Seppyo*, **42**, 41-52.
- Fujii, Y. and Higuchi, K.** 1972. On the permafrost at the summit of Mt. Fuji, *Seppyo*, **34**, 9-22.
- Fukuda, M. and Kinoshita, S.** 1974. Permafrost at Mt. Taisetsu, Hokkaido and its climatic environment: *The Quaternary Research*, **12**, 192-202 (in Japanese with English summary).
- Fukuda, M. and Sone, T.** 1992. Some characteristics of alpine permafrost, Mt. Daisetsu, central Hokkaido, Northern Japan: *Geografiska Annaler*, **74A**, 159-167.
- Fukui, K. and Iwata, S.** 2000. Result of permafrost investigation in Kuranosuke cirque, Tateyama, the Japanese Alps: *Seppyo*, **62**, 23-28 (in Japanese with English summary).
- Funk, M. and Hoelzle, M.** 1992. A model of potential direct solar radiation for investigating occurrences of mountain permafrost: *Permafrost and Periglacial Processes*, **3**, 139-142.
- Goodrich, L. E.** 1982. The influence of snow cover on the ground thermal regime. *Canadian Geotechnical Journal*, **19**, 421-432.

- Greene, E. M., Liston, G. E., and Pielkers, R. A.** 1999. Simulation of above timberline snowdrift formation using a numerical snow-transport model. *Cold Region Science and Technology* **30** (1-3), 135-144.
- Griffiths, D. H., Turnbull, J. and Olayinka, A. I.** 1990. Two-dimensional resistivity mapping with a computer-controlled array, *First Break*, **8**, 121-129.
- Griffiths, D. H. and Barker, R. D.** 1993. Two-dimensional resistivity imaging and modelling in areas of complex geology. *Journal of Applied Geophysics*, **29**, 211-226.
- Gruber, S. and Hoelzle, M.** 2001. Statistical modelling of mountain permafrost distribution: local calibration and incorporation of remotely sensed data: *Permafrost and Periglacial Processes*, **12**, 69-77.
- Haeberli, W.** 1973. Die Basis-Temperatur der winterlichen Schneedecke als möglicher Indikator für die Verbreitung von Permafrost in den Alpen: *Zeitschrift für Gletscherkunde und Glazialgeologie*, **9**, 221-227.
- Haeberli, W.** 1978. Special aspects of permafrost methodology and zonation in the Alps: In *Proceedings, Third International Conference on Permafrost, Vol. 1*. National Research Council, Ottawa, pp. 379-384.
- Haeberli, W.** 1985. Creep of mountain permafrost: internal structure and flow of Alpine rock glaciers: *Mitteilungen der VAW-ETH Zürich*, **77**.
- Haeberli, W., Cheng, G., Gorbunov, A. P. and Harris, S. A.** 1993. Mountain permafrost and climate change. *Permafrost and Periglacial Processes*, **4**, 165-174.
- Haeberli, W. and Patzelt, G.** 1982. Permafrostkartierung im Gebiet der Hochebenkar blockgletscher, Obergurgl, Ötztaler Alpen: *Zeitschrift für Gletscherkunde und Glazialgeologie*, **18(1/2)**, 127-150.
- Haeberli, W. and Vonder Mühl, D.** 1996. On the characteristics and possible origins of ice in rock glacier permafrost: *Zeitschrift für Geomorphologie*, N.F., Suppl.-Bd, **104**, 43-57.
- Harada, K., Fukuda, M. and Ishizaki, T.** 1991. Measurements of electrical resistivity of frozen soils: *Low Temperature Science, Ser. A*, **50**, 57-68 (in Japanese with English summary).
- Harris, C., Davis, M. C. R. and Etzelmüller, B.** 2001. The assessment of potential geotechnical hazard associated with mountain permafrost in a warming global

- climate, *Permafrost and Periglacial Processes*, **12**, 145-156.
- Harris, S. A.** 1979. Ice caves and permafrost zones in southwest Alberta, *Erdkunde*, **33**, 61-70.
- Harris, S. A.** 1981a. Climatic relationships of permafrost zones in areas of low winter snow-cover: *Arctic*, **34**, 64-70.
- Harris, S. A.** 1981b. Climatic relationships of permafrost zones in areas of low winter snow-cover: *Biuletyn Peryglacjalny*, **28**, 227-240.
- Harris, S. A.** 1983. Cold air drainage west of Fort Nelson, British Columbia. *Arctic*, **35**, 539-541.
- Harris, S. A.** 1988. The alpine periglacial zone. In: M. J. Clark (ed.), *Advances in periglacial geomorphology*. Chichester: J. Wiley and Sons Ltd, pp. 385-391.
- Harris, S. A. and Pederson, D. E.** 1998. Thermal Regimes Beneath Coarse Blocky Materials: *Permafrost and Periglacial Processes*, **9**, 107-120.
- Hauck, C. and Vonder Mühl, D.** 1999. Using DC resistivity tomography to detect and characterize mountain permafrost. In *Proceedings of the 61st European Association of Geoscientists and Engineers (EAGE) Conference, 7-11 June 1999, Helsinki, Finland*. 2-15.
- Higuchi, K. and Fujii, Y.** 1971. Permafrost at the summit of Mount Fuji, Japan. *Nature*, **230**, 521.
- Hoekstra, P. and McNeill, D.** 1973. Electromagnetic probing of permafrost: *North American contribution, Second International Conference on Permafrost*. National Academy of Science, Publication 2115, Washington, D.C., pp.517-526.
- Hoelzle, M.** 1992. Permafrost occurrence from BTS measurements and climatic parameters in the eastern Swiss Alps: *Permafrost and Periglacial Processes*, **3**, 143-147.
- Hoelzle, M.** 1993. DC resistivity Soundings 1992 in North-Western Svalbard. Arbeitsheft, 13, Laboratory of Hydraulics Hydrology and Glaciology, ETH-Zürich, **132**.
- Hoelzle, M.** 1994. *Permafrost und Gletscher im Oberengadin. Grundlagen und Anwendungsbeispiele für automatisierte Schätzverfahren*. Mitteilung der VAW-ETH Zürich, **132**.
- Hoelzle, M.** 1996. Mapping and modelling of mountain permafrost distribution in the

- Alps: *Norsk Geografisk Tidsskrift*, **50**, 11-15.
- Hoelzle, M.** 1999. Miniature temperature dataloggers for mapping and monitoring of permafrost in high mountain areas: First experience from the Swiss Alps: *Permafrost and Periglacial Processes*, **10**, 113-124.
- Hoelzle, M. and Haerberli, W.** 1995. Simulating the effect of mean annual air-temperature changes on permafrost distribution and glacier size: an example from the Upper Engadin, Swiss Alps. *Annals of Glaciology*, **21**, 399-405.
- Hoelzle, M., Haerberli, W. and Keller, F.** 1993. Application of BTS measurements for modelling permafrost distribution in the Swiss Alps. In: *6th International Conference on Permafrost, Beijing, China*. South China University Technology Press, 272 – 277.
- Hoelzle, M., Mittaz, C., Etzelmüller, B. and Haerberli, W.** 2001. Surface energy fluxes and distribution models of permafrost in European Mountains areas: an overview of current developments: *Permafrost and Periglacial Processes*, **12**, 53-68.
- Hulme, M., Mitchell, J., Ingram, W., Lowe, J., Johns, T., New, M. and Viner, D.** 1999. Climate change scenarios for global impacts studies. *Global Environmental Change*, **9**, S3–S19.
- Humlum, O.** 1997. Active layer thermal regime at three rock glacier in Greenland. *Permafrost and Periglacial Processes*, **8**, 383-408.
- Imhof M.** 1996. Modelling and verification of the permafrost distribution in the Bernese Alps (Western Switzerland). *Permafrost and Periglacial Processes*, **7**, 267-280.
- Imhof, M., Pierrehumbert G., Haerberli W, Kieenholz H.** 2000. Permafrost investigation in the Schilthorn massif, Bernese Alps, Switzerland. *Permafrost and Periglacial Processes*, **11**, 189-206.
- Isaksen, K., Holmlund, J., Sollid, L. and Harris, C.** 2001. Three deep alpine-permafrost borehole in Svalbard and Scandinavia, *Permafrost and Periglacial Processes*, **12**, 13-25.
- Ishikawa, M., Watanabe, T., Nakamura, N.** 2001. Genetic variation of the rock glacier and its implication to the discontinuous mountain permafrost zones in the Kanchanjunga Himal, eastern Nepal. *Permafrost and Periglacial Processes*, **12**, 243-253.

- Ishikawa, M. and Hirakawa, K.** 2000. Mountain permafrost distribution based on BTS measurements and DC resistivity soundings in the Daisetsu Mountains, Hokkaido, Japan: *Permafrost and Periglacial Processes*, **11**, 109-123.
- Ishikawa, M. and Sawagaki, T.** *in press*. GIS simulation of the spatial distribution of snow cover and observed ground temperature in the Daisetsu Mountains, Japan, *Norsk Geografisk Tidsskrift*.
- Ito, K. and Sato, K.** 1981. Explanatory notes for actual vegetation map of the Daisetsuzan Mountains. *Synthetic survey of the Daisetsuzan Mountains, Hokkaido*, 23pp (in Japanese with English abstract).
- Jacob M.** 1992. Active rock glaciers and the lower limit of discontinuous alpine permafrost, Khumbu Himalaya, Nepal. *Permafrost and Periglacial Processes*, **3**, 253-256.
- Keller, F.** 1992. Automated mapping of mountain permafrost using the program PERMAKART within the geographical information system ARC/INFO: *Permafrost and Periglacial Processes*, **3**, 133-138.
- Keller, F.** 1994. *Interaktion zwischen Schnee und Permafrost. Eine Grundlagenstudie im Oberengadin*. Mitteilung der VAW-ETH Zürich, **127**.
- Keller, F. and Gubler, H.** 1993. Interaction between snow cover and high mountain permafrost, Mürtel/Corvatsch, Swiss Alps: In *Sixth International Conference on Permafrost, Proceedings*, Vol.1. pp. 332-337.
- King, L.** 1983. High mountain permafrost in Scandinavia: In *Proceedings, the Fourth International Conference on Permafrost*, National Academy Press, Washington, D.C., pp.612-617.
- King, L., Fisch, W., Haerberli, W. and Waechter, H. P.** 1987. Comparison of resistivity and radio-echo soundings on rock glacier permafrost: *Zeitschrift für Gletscherkunde und Glazialgeologie*, **23**, 77-97.
- King, L., Gorbunov, A. P. and Evin, M.** 1992. Prospecting and Mapping of permafrost and associated phenomena: *Permafrost and Periglacial Processes*, **3**, 73-81.
- Kneisel, C., Hauck, C. and Vonder Mühl, D.** 2000. Permafrost below the timberline confirmed and characterized by geoelectrical resistivity measurements, Bever valley Eastern Swiss Alps: *Permafrost and Periglacial Processes*, **11**, 295-304.
- Koaze, T.** 1965. The patterned grounds on the Daisetsu volcanic group, central

- Hokkaido: *Geographical Review of Japan*, **38**, 179-199 (in Japanese with English summary).
- Koefoed, O.** 1979. *Geosounding principles. 1. Resistivity Sounding Measurements*, Elsevier, Amsterdam, Oxford, New York.
- Lachenbruch, A. H. and Marshall, B. V.** 1986. Changing climate: geothermal evidence from permafrost in the Alaskan Arctic, *Science*, **234**, 689-696.
- Li, X., L., Guodong, C. and Xianzhang, C.** 1998. Response of permafrost to global change on the Qinghai-Xizang Plateau –A GIS-aided model: In *Proceedings of the Seventh International Conference on Permafrost, Yellowknife, Canada*. 657-661.
- Liston, G. E., and Stturm M.** 1998. A snow-transport model for complex terrain. *Journal of Glaciology*, **44**, 498-516.
- Loke, M. H. and Barker, R. D.** 1995. Least-squares deconvolution of apparent resistivity, *Geophysics*, **60**, 1682-1690.
- Loke, M. H. and Barker, R. D.** 1996. Rapid least-squares inversion of apparent resistivity pseudosections using quasi-Newton method: *Geophysical Prospecting*, **44**, 131-142.
- Matsuoka, N.** 1998. Rock Glaciers: Glacial or periglacial?: *Journal of Geography*, **107**, 1-24 (in Japanese with English summary).
- Matsuoka, N. and Ikeda, A.** 1998. Some observations regarding mountain permafrost in the Japanese Alps. Annual Report of the Institute of Geoscience, the University of Tsukuba, **24**, 19-25.
- Mittaz, C., Hoelzle, M. and Haerberli, W.** 2000a. First steps towards a mountain permafrost distribution model with energy balance data. *European Geophysical Society, 25th General Assembly*, Vol.2. Geophysical Research Abstracts, Nice, CD-ROM.
- Mittaz, C., Hoelzle, M. and Haerberli, W.** 2000b. First results and interpretation of energy-flux measurements of Alpine permafrost. *Annals of Glaciology*, **31**, 275-280.
- Miyamoto, M.** 1999. Disappearance of a snowpatch in the hollow of the northeastern slope of Mt. Koizumidake, the Daisetsu Mountains, Central Hokkaido. *Quarterly Journal of Geography*, **51**, 134-144 (in Japanese with English abstract).

- Nakayama, T., Sone, T., and Fukuda, M.** 1993. Effect of climatic warming on the active layer. *Proceedings of Permafrost Sixth International Conference*, Vol.1, South China University of Technology Press, 488-493.
- Nelson, F. E. and Outcalt, S. I.** 1987. A computational method for prediction and regionalization of permafrost. *Arctic and Alpine Research*, **19**, 279-288.
- Ohmura, H., Ishida, T., Kobayashi, D. and Yamada, T.** 1967. Studies on blowing snow II, Physics of Snow and Ice, Part 2, Institute of Low Temperature Sciences, *Sapporo*, 1099-1117.
- Okitsu, S., and Ito, K.** 1984. Vegetation dynamics of the Siberian dwarf pine (*Pinus pumila* Regel) in the Taisetsu mountain range, Hokkaido, Japan. *Vegetario* **58**, 105-113.
- Osterkamp, T. E. and Romanovsky V. E.** 1996. Characteristics of changing permafrost temperatures in the Alaskan Arctic, U.S.A. *Arctic and Alpine Research*, **28**, 267-273.
- Osterkamp, T. E. and Romanovsky V. E.** 1999. Evidence for warming and thawing of discontinuous permafrost in Alaska. *Permafrost and Periglacial Processes*, **10**, 17-37.
- Pazderik, O. and Blaha, V.** 1996. Examples of resistivity imaging using ME-100 resistivity field acquisition system. *EAGA 58th Conference and Technical Exhibition - Amsterdam, The Netherlands, 3-7 June 1996*.
- Péwé, T. L.** 1983. Alpine permafrost in the continuous United States: a review. *Arctic and Alpine Research*, **15**, 145-156.
- Péwé, T. L.** 1991. Permafrost. In: G. A. Kiersch (ed.) *The heritage of engineering geology: the first hundred years*. Boulder, Colorado: Geological Society of America Centennial Special Volume 3, pp. 277-298.
- Powell, M. J. D.** 1970. A hybrid method for nonlinear equations. In: *Numerical method for Nonlinear algebraic equations*, P. Rabinowitz, ed., Gordon and Breach, pp, 87-114, 115-161.
- Sone, T.** 1990. The permafrost environment of the Daisetsu Mountains, central Hokkaido, Northern Japan: *Environmental Science, Hokkaido University*, **13**, 1-28.
- Sone, T.** 2000. Thermal regime of permafrost at Takanegahara in the Daisetsu Mountains, Hokkaido, Japan. *Proceedings of the General Meeting of the*

- Association of Japanese Geographers*, **57**, 442-443 (in Japanese).
- Sone, T. and Nakayama, T.** 1992. Air temperature data at Hakuun Hut in the Daisetsu Mountains, central Hokkaido, 1987-1989: *Low Temperature Science*, Ser. A, **51**, *Data report* (in Japanese with English summary).
- Sone, T. and Takahashi, N.** 1986. Winter field observations of the frost-fissure polygons on Hokkai-daira plateau, Daisetsu volcanic massif, Hokkaido: *Geographical Review of Japan*, **59**, 654-663 (in Japanese with English summary).
- Sone, T. and Takahashi, N.** 1988. Climate in Mt. Daisetsu, as viewed from the year round meteorological observation at Hakuun hut in 1985: *Annals of the Tohoku Geographical Association*, **40**, 237-246 (in Japanese with English summary).
- Sone, T., Takahashi, N. and Fukuda, M.** 1988. Alpine permafrost occurrence at Mt. Taisetsu, central Hokkaido, in northern Japan: In *Permafrost Fifth International Conference Proceedings* Vol.1., Tapir Publishers, Trondheim, pp. 253-258.
- Takahashi, N.** 1983. Landslides around Takanegahara in the Daisetsuzan Mountains, Hokkaido, Japan. *Abstracts of the Annual Meeting of the Association of Japanese Geographers*, **24**, 88-89 (in Japanese).
- Takahashi, N.** 1985. The block stream on the Chubetsudake NW slope in Daisetsuzan Mountains: *Annals of the Tohoku Geographical Association*, **37**, 16-28 (in Japanese with English summary).
- Takahashi, N.** 1990. Environmental-Geomorphological study on the Holocene mire development in the Daisetsuzan Mountains, Central Hokkaido, Northern Japan: *Environmental Science, Hokkaido University*, **13**, 93-156.
- Takahashi, N.** 1995. Distribution of the autumn ground temperature and its controlling factors in the alpine zone of the central Daisetsuzan Mountains. *Geographical Review of Japan*, **68A-1**, 27-42(in Japanese with English summary).
- Takahashi, N. and Sone, T.** 1988. Palsas in the Daisetsuzan Mountains, central Hokkaido, Japan: *Geographical Review of Japan*, **61**, 665-684 (in Japanese with English summary).
- Vonder Mühl, D.** 1993. *Geophysikalische Untersuchungen im Permafrost des Oberengadins*. Mitteilung der VAW-ETH Zürich, **122**.
- Vonder Mühl, D. Stucki, T. and Haerberli, W.** 1998. Borehole temperature in alpine permafrost: a ten years series: In *Proceedings of the Seventh International*

*Conference on Permafrost, Yellowknife, Canada. 1089-1095.*

- Vonder Mühl, D., Hauck, C., Gubler, R., McDonald, R. and Russill, N.** 2001. New geophysical methods of investigating the nature and distribution of mountain permafrost with special reference to radiometry techniques. *Permafrost and Periglacial Processes*, **12**, 27-38.
- Wakahama, G., Endo, Y., Yamada, T., Ushiki, H. and Naruse, R.** 1968. Studies of firn on Mt. Daisetsu in summer, III, *Low Temperature Science*, **26**, 215-235 (in Japanese with English summary).
- Wakahama, G., Shimizu, H., Akitaya, E., Narita, H., Tanuma, K., Yamada, T., Naruse, R., Kitahara, T., Sato, N., Ishikawa, N. and Kawamura, T.** 1969. Studies of firn on Mt. Daisetsu in summer, IV, *Low Temperature Science*, **27**, 181-196 (in Japanese with English summary).
- Washburn, A. L.** 1979. *Geocryology*. Arnold London, 406p.
- Williams, P. J. and Smith, M. W.** 1989. *The Frozen Earth: Fundamentals of Geocryology*. Cambridge University Press. 306pp.
- Yamada T., Nishimura H., Suizu S. and Wakahama G.** 1978. Distribution and Process of accumulation and ablation of snow on the west slope of Mt. Asahidake, Hokkaido. *Low Temperature Science Ser. A* **32**, 1-12 (in Japanese with English summary).
- Yamada, T.** 1982. Studies on accumulation-ablation processes and distribution of snow in mountain regions, Hokkaido. *Low Temperature Science*, **31**, 1-33.
- Yoshino, M. M.** (1968): *Climatology*. Chujin-Shoin, Tokyo (in Japanese).